AN ABSTRACT OF THE DISSERTATION OF

Jason William Nikkel for the degree of Doctor of Philosophy in Chemistry presented on December 18, 2020.

Title: Designing Dielectric Materials through Complex Metal Oxides.

Abstract approved: ____

David P. Cann

This dissertation demonstrated that the electrical properties of complex oxide-based perovskite materials could be controlled through the careful modification of both material composition and structure. This was first shown through the modification of lead zirconate titanate ($Pb(Zr_{0.52}Ti_{0.48})O_3$, PZT) solid solutions with bismuth indate ($BiInO_3$, BI) where the relative stability of the parent PZT phases, tetragonal (P4mm) and rhombohedral (R3m,) were shifted with increasing additions of BI. There were also observations of a correlated reduction in the Curie temperature with increasing additions of BI. Control over the electrical properties was also demonstrated through the modification of the $Ba_{0.85}Ca_{0.15}(Zr_{0.10}Ti_{0.90})O_3$ solid solution with $Bi(Zn_{0.50}Ti_{0.50})O_3$ through the disruption of long-range ferroelectric dipole order, resulting in a relaxor ferroelectric phase with a very high permittivity over a very large temperature range.

Studies into BI modified PZT solid solutions showed the formation of stable solid solutions with the incorporation of BI at up to 10 mol% for PZT compositions with a Zr:Ti ratio of 50:50, and with up to 15 mol% BI with a Zr:Ti ratio of 52:48. Dielectric and ferroelectric studies were carried out on xBI – (1-x) PZT (52/48) samples for $0\% \leq x \leq 10\%$. These studies showed a decrease to the Curie temperature from 390°C at 0% BI to

325°C at 10% BI, a transition in the room temperature ferroelectric phase from tetragonal at 0%, to mixed tetragonal and rhombohedral at 2.5%, to rhombohedral at 5% and above, and a variation to the high temperature phase transitions prior to the cubic paraelectric phase resulting in a rhombohedral to tetragonal phase transition in the 10% BI composition. Ferroelectric studies showed all samples to saturate at approximately 40 kV/cm upon which polarization loops of a normal ferroelectric were observed with coercive fields ranging from 10.8 kV/cm to 14.1 kV/cm, remanent polarizations ranging from 7.4 $\mu C/cm^2$ to 12.1 $\mu C/cm^2$, and maximum polarizations ranging from 18.4 $\mu C/cm^2$ to 24 $\mu C/cm^2$ (properties summarized from a maximum applied field of 50 kV/cm.) Piezoelectric studies were carried out on 2.5% BI – PZT (52/48) samples showing an average maximum strain of 0.2% correlating to an inverse piezoelectric coefficient (d_{33}^*) of 280 pC/N at 70 kV/cm.

The modification of the ferroelectric $Ba_{0.85}Ca_{0.15}(Zr_{0.10}Ti_{0.90})O_3$ solid solutions with 1% $Bi(Zn_{0.50}Ti_{0.50})O_3$ resulted in a high permittivity relaxor ferroelectric phase. The induced relaxor phase was observed to be very sensitive to both processing effects and stoichiometry, with small modifications to processing parameters resulting in complex changes to the magnitude of the permittivity and the size distribution of PNRs, as evidenced by shifts in the observed T_{max}. The desirable high permittivity relaxor phase was determined to be dependent on the existence of secondary phases, as single-phase samples were observed to maintain relaxor character in the dielectric properties while exhibiting relatively low permittivity. The existence of secondary phases was determined to be a function of cooling rate, with increased cooling rates showing lesser impurities, and bismuth oxide excess, as opposed to being determined by maximum sintering temperature. This material was found to be promising for multi-layer ceramic capacitor applications, though further research is needed into mitigating space charge contributions to the permittivity.

Designing Dielectric Materials through Complex Metal Oxides

by
Jason William Nikkel

A DISSERTATION

submitted to

Oregon State University

in partial fulfillment of
the requirements for the
degree of

Doctor of Philosophy

Presented December 18, 2020
Commencement June 2021

Doctor of Philosophy dissertation of Jason William Nikkel presented on December 18, 2020

APPROVED:

Major Professor, representing Chemistry

Head of the Department of Chemistry

Dean of the Graduate School

I understand that my dissertation will become part of the permanent collection of Oregon State University libraries. My signature below authorizes release of my dissertation to any reader upon request.

Jason William Nikkel, Author

ACKNOWLEDGEMENTS

I would like to express my sincerest gratitude and appreciation to the figurative, and almost literal, village of professional academic colleagues who have worked with me and assisted me throughout my undergraduate and graduate tenure. I truly would not be able to be in this position without them.

Above all, I would like to thank my wife, María José Ugalde Rojo, for every single ounce of love, patience, support, and understanding she has poured out on me. I could not have asked for a better partner in this life, and I owe you a debt of gratitude one could never repay. Y más, quiero agradecer su mamá y tía, María Guadalupe Ugalde Rojo y Adriana Ugalde Rojo, por recibirme a su familia y sus corazones con abrazos abiertos. Sus presencia e influencia en mi vida ha sido nada más que una bendición, y no puedo describir que tanto agradecido estoy por ello.

I would further like to acknowledge my major Professor David Cann for his continued guidance and assistance throughout my work with him as an undergraduate and now again as I finish my graduate career. To whom I owe the discovery of the realm of materials science and, without, I may have mistakenly decided to stay in pre-medicine nigh a decade ago and was the impotence of my academic journey. I would also like to thank Professor Michelle Dolgos for her time as my primary advisor and her valued insights, guidance, and assistance throughout. I would especially like to thank Professor Jacob Jones for his guidance and assistance during my time in his research group, without his help, guidance, patience, and encouragement, both professional and personal, I would not be able to in the position I am today.

To my fellow graduate students and colleagues, I would like to acknowledge the collaborative members of the Dolgos research group, Cann research group and Jones research group for always making themselves available and helpful in all my endeavors. In particular, Giovanni Esteves, Chris Fancher, Ryan McQuade, Brienne Johnson, Michael Bowen, Sanu Gupta, Kyle Grove, Dylan Fast, Wesley Surta, Eric Patterson, Troy Ansell, Nitish Kumar, Hanhan Zhao, Dong Hou, BB Chung, Tedi-Marie Usher-Ditzian, Thanakorn Iamsasri, Ashley Diane-Mason, Matt Nelson, Sasiporn Prasertpalichat, Natthaphon Raengthon, Jenny Forrester, Jonathon Guerrier, Charles Culbertson, Alyssa Johnson, Brian Zanca, Thomas Rowe, Alicia Majón Sanz, Greg Guymon, and John Magnum. Everyone of you played a role in my development both professionally and personally, and I cannot express my gratitude enough for your enrichment of my life.

I would also like to acknowledge my committee members, David Cann, Michelle Dolgos, Douglas Keszler, Brian Bay, and John Conley, and thank them for their continued flexibility and for being kind, supportive, and genial in all interactions.

Finally, I would like to acknowledge and thank my family for their love and support throughout my entire career and life. My father, Eric, mother, Leanne, brother, Matt, and sister, Mari. Without your continued love, support, and guidance I would not be the person I am today.

CONTRIBUTION OF AUTHORS

Professor David Cann contributed to all work included within through assistance in guidance, experimental design, data analysis, manuscript preparation, and editing. Professor Michelle Dolgos contributed to all work in chapter 3 through project conception, experimental design and guidance, data analysis, and manuscript preparation. Dr. Ryan McQuade contributed to all work within chapter 3 through guidance and assistance in his capacity as a postdoctoral scholar. My fellow graduate student Kyle Grove contributed to the work in chapters 4 and 5 through his work on the same project. Finally, my undergraduate worker Gregory Guymon contributed to all work in chapters 4 and 5 through assistance in synthesis.

TABLE OF CONTENTS

Page

TABLE OF CONTENTS (Continued)

Page

TABLE OF CONTENTS (Continued)

Page

TABLE OF CONTENTS (Continued)

Page

TABLE OF CONTENTS (Continued)

Page

TABLE OF CONTENTS (Continued)

Page

LIST OF FIGURES

LIST OF FIGURES (Continued)

LIST OF FIGURES (Continued)

LIST OF FIGURES (Continued)

LIST OF FIGURES (Continued)

LIST OF FIGURES (Continued)

LIST OF FIGURES (Continued)

LIST OF TABLES

LIST OF TABLES (Continued)

LIST OF APPENDICES

LIST OF APPENDIX FIGURES

LIST OF APPENDIX FIGURES (Continued)

DEDICATION

All work within this document is dedicated to my loving wife, and to my Lord and Savior, Jesus Christ in whom all things are possible.

Chapter 1

1. INTRODUCTION

Advanced, high performance, dielectric materials are central to modern infrastructure and key to developing future technologies. As the backbone of advanced electronic devices, dielectric materials range widely in role when it comes to technology. Their applications range from those who rely solely on the dielectric effect (insulators, multi-layer capacitors, electronic filters, etc.) to more advanced applications such as piezoelectrics (actuators, acoustic resonators, ultra-sound, energy harvesters, etc.) or ferroelectrics (non-volatile memory, ferroelectric capacitors, etc.) Dielectric materials provide the basis for charge displacement through polarization in otherwise insulating, non-electronically active solids, and leads to more elaborate phenomena in these materials such as the piezoelectric effect, which couples mechanical energy and electrical energy, and the ferroelectric effect, which allows for switchable binary memory. The use of these materials pervades the world of electronic devices and many are at the leading edge of the development of higher performing, and more efficient, advanced dielectric materials. This is the driving force behind improving current technology and developing novel futuristic technologies. The scope of this work is to develop dielectric materials for broad temperature range and high permittivity applications through a fundamental understanding of the dielectric effect and crystal chemistry of solid-state solutions of complex metallic oxides.

The aim of this review is to develop a rich fundamental knowledge base pertaining to dielectric materials from industrial, historical, and scientific viewpoints using available literature, and to explore the current literature and state of high permittivity (high κ) materials to develop possible novel materials for multilayer capacitor applications. It is important to note that the scope of this work will be focused on, and limited to, bulk electroceramic systems, as the application of the thin film paradigm only further convolutes the issues at hand.

1.1 The Push for High κ

The ability to store electrical charge was first demonstrated in the mid-18th century and one year later the first primitive capacitor, the Leyden jar, was invented [1]. Even while it was not fully understood, it was quickly improved upon by attaching multiple jars in parallel [2]. Although it is not an earth-shattering anecdote, it has one large implication: even at their inception, capacitors have continually been engineered and designed to store greater and greater charge.

Today, charge storage is an integral part of our society. Just recently in 2019, it was determined that the number of physical electronic devices out populated the worldwide human populace [3]. Each one of these devices rely on hundreds, if not thousands, of multilayer ceramic capacitors (MLCCs) that range from macroscopic to microscopic in size. With the ever-increasing push for miniaturization of electronic devices and to incorporate elaborate space-consuming functionalities into newer models, the space available for their necessary basic components, namely MLCCs, has become a limiting barrier to miniaturization [4]. Therefore, designing MLCCs of smaller size, yet equal capacitance, is a necessary hurdle on the current path to miniaturization of 5G devices and beyond. However, brute engineering of MLCC components can only get one so far, as the capacitance of these devices is mainly dependent on two factors: the number of layers in the MLCC (which within a fixed form factor is limited by thickness of each layer and is limited by the mechanical integrity of the device) and the relative permittivity of the dielectric material of each layer. As the layer thickness of MLCCs had already hit 0.5μm in 2010 [5], the theoretical thickness of these dielectric layers is currently being approached and only leaves one avenue forward to further decrease the size of MLCCs, that is, increasing the relative permittivity of the material. This can be observed through the fundamental formula for the capacitance of an MLCC:

$$C = \frac{N\kappa\varepsilon_0 A}{t}$$

Where N represents the number of layers in the MLCC devices, t is the thickness of each layer, A is the area of electrode overlap of top and bottom electrodes in a layer, ε_0 is the permittivity of free space, and k is the dielectric constant of the material.

Further complicating things is the need for the capacitance of the MLCC to be temperature stable as most mobile devices operate over a wide range of temperatures. As a materials permittivity is generally a highly temperature sensitive property, due in part to the inherent nature of the dielectric effect, as well as the fundamental mechanisms of polarization, the challenge of developing high κ materials for MLCC applications is a multi-faceted one deserving of careful scrutiny and investigation.

1.1.1 A Note of Clarity on Permittivity and the Dielectric Constant

Given the redundant nomenclature around a materials permittivity (*relative permittivity*, ε_r, *permittivity of free space*, ε_0, and *permittivity*, ε, as the actual materials property,) as well as the added convolution that the *relative permittivity* of a material is equivalent to the *dielectric constant*, κ, the language found in literature to discuss *permittivity* (as a concept) can be ambiguous and vary widely. In this work, the nomenclature of *relative permittivity* and *dielectric constant* will be used interchangeably as mathematically:

$$\kappa \equiv \varepsilon_r$$

For purposes of shorthand, also note that, unless explicitly stated as the actual materials property, ε, the use of the term *permittivity* will also be used interchangeably with *relative permittivity*, and therefore will also refer to the *dielectric constant*, κ. This use of shorthand is believed to be the root of the confusion, as the *relative permittivity*, ε_r, of a material is the ratio of the materials property *permittivity*, ε, and the *permittivity of free space*, ε_0, mathematically represented here:

$$\varepsilon_r = \frac{\varepsilon}{\varepsilon_0}$$

1.1.2 Classes of Dielectric Materials

With the scope of this work focusing on dielectric materials for capacitor applications, a brief overview of how these materials are organized is beneficial. The following was summarized from Moulson and Herbert second edition [6] and compiled in **Table 1.1** with the electronic industrial alliance (EIA) coding scheme as reported by Fortunato [7]. There are four individual classes of dielectric ceramics, and they are qualified by relative permittivity range as well as type of dielectric.

Class I dielectrics are low permittivity dielectrics with very low dielectric loss. These materials range from dielectric constants on the order of 10(s) to 1000(s) with dielectric losses on the order of 0.001. While these materials are high quality insulators due to their very low loss and can be used under large voltages, their very low dielectric constants make them undesirable for capacitor technologies and will not be considered in this work.

Class II and III dielectrics are high permittivity materials and are generally based on ferroelectric materials systems. These materials range from dielectric constants on the order of 1000(s) to 10,000(s) while maintaining relatively low dielectric losses on the order of 0.01. They are known for high volumetric efficiencies; however high losses can be induced at higher temperatures and under the application of a.c. fields. As these materials combine a high permittivity with low dielectric loss, they are very desirable for capacitor technologies and will be of main consideration in this work, and the most well-known ferroelectric material belonging to this class is barium titanate.

Class IV dielectrics are also high permittivity materials, but of high dielectric loss. These materials generally contain a highly conductive phase, or large contributions to the dielectric constant through space charge, which can lead to very high permittivities over limited frequencies and voltages. These permittivities are inherently voltage dependent and

Table 1.1: Summary of classes of capacitor materials and coding designation for Class II/III as defined by the Electronic Industry Alliance (EIA). X7R, one of the most well-known capacitor materials can be determined from this coding to vary only 15% in capacitance from -55°C to +125°C. It is acknowledged that this coding is out of date due to the adoption of the International Electrotechnical Commission (IEC) standards adopted in 2010, however EIA coding is still widely used and referenced. Data summarized from Moulson and Herbert and Fortunato [6],[7]

Class	**ε_r range**	**EIA code**	**Temp (°C)**	**EIA #**	**Temp (°C)**	**EIA code**	**Capacitance change %**
I	**15 - 500**	X	-55	2	+45	D	±3.3
		Y	-30	4	+65	E	±4.7
		Z	+10	5	+85	F	±7.5
II/III	**2000 - 20,000**			6	+105	P	±10
				7	+125	R	±15
				8	+150	S	±22
IV	**> 20,000**			9	+200	T	+ 22, -33
						U	+ 22, -56
						V	+ 22, -82

therefore this class of dielectrics is limited to very low voltages for use in electrical circuits. Materials of this class commonly exhibit what is known as the Maxwell-Wagner effect [8],[9], or can be modeled as internal barrier layer capacitors. Due to these factors, these materials are not desirable for use at the frequency and voltage levels necessary for mobile applications.

As previously stated, the scope of this work is focused on high permittivity materials for capacitor applications. As the literature around high permittivity materials can be indiscriminate to Class II/III and Class IV dielectrics, a large portion of this work will be dedicated to deconvoluting this fact and identifying possible Class II/III dielectrics of high permittivity for future research and development.

1.1.3 Historic and Current State of Tech

Capacitor technology has been in the crucible of advancement for centuries. However, leaps and bounds of progress in capacitor and materials technologies have been made over just the past half-century, culminating in the wide variety of capacitor devices

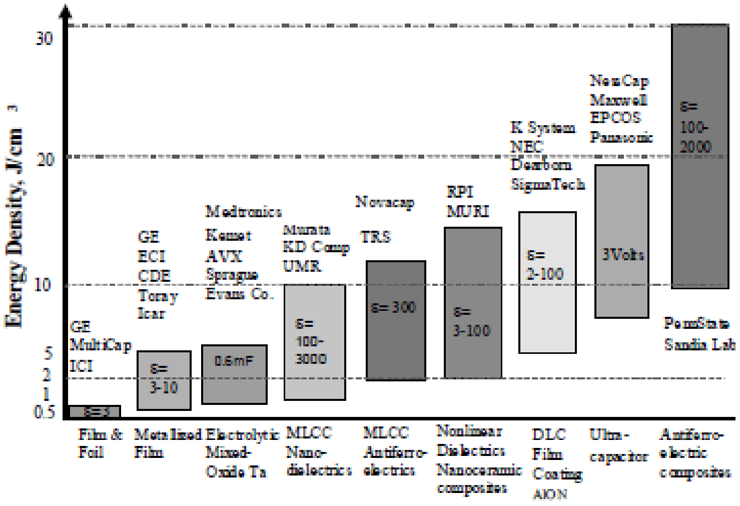

Figure 1.1: First figure from '*Advanced Dielectrics for Capacitors'* Tan et al. [15] showing the energy density of various capacitor devices as conceived throughout history.

in utilization today. From the historical inception of the Leyden Jar in 1745, to mica-based capacitors developed in 1850 (which saw use along-side rolled paper/ceramic capacitors, developed in 1900, throughout both world wars,) to more advanced technologies such as the rolled foil tower capacitor in 1960, and electrolytic capacitors in 1970. On the turn of the 20th, and start of the 21st century, however, capacitor technology exploded with the development of multi-layer ceramic capacitors (MLCCs) in between 1950 and 1970 [11]–[15], the metallized film cap capacitor in 1990, ultra-capacitors 2000, nano-dielectric capacitors in 2002, and finally nonlinear composites 2004 summarized in **Fig. 1.1** [16]. Notably of these technologies are MLCCs which take advantage of class II/III dielectric ceramics (namely barium titanate, or composites thereof.)

1.1.3.1 History of Barium Titanate

Barium titanate, $BaTiO_3$, the most important material in MLCC capacitors and one of the first oxide materials in which ferroelectricity was observed, was discovered during World War II in 1941 and 1944 [17]. Initially discovered through doping studies of TiO_2 with barium oxide, due to dwindling mica supplies as German U-boats threatened the Allies mica sources in South America, it was found to have dielectric constants an order of magnitude higher than any other known material at the time [18]. Immediate realization of the possible benefits of such a material are seen through the plethora of work done after its public availability at the close of the war [19]–[27]. This body of work is responsible for elucidating, not only the foundational knowledge of the materials system still built upon today, but foundational knowledge of the interplay between ferroelectric domains and grain

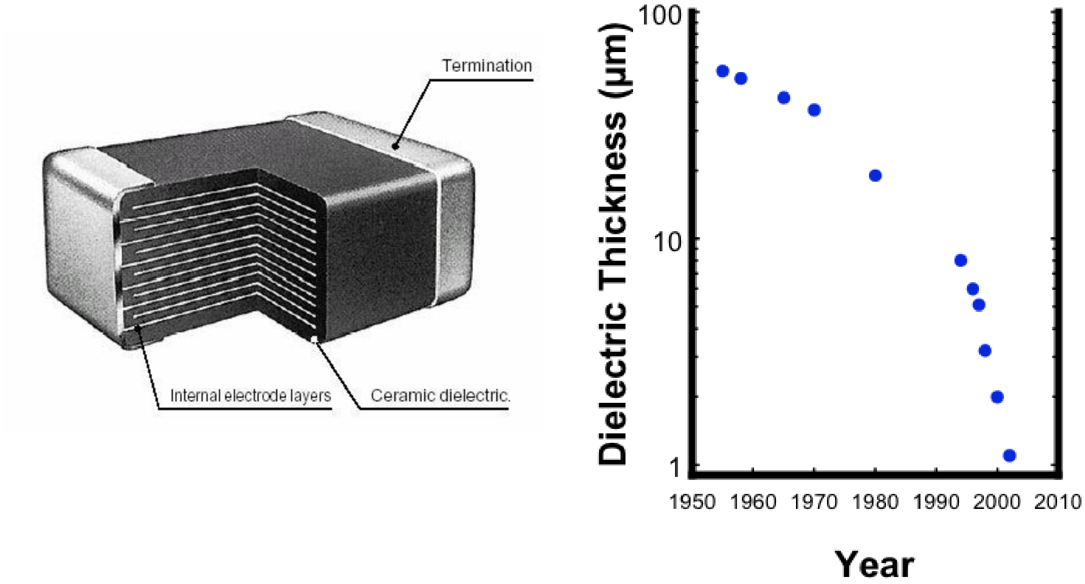

Figure 1.2: (left) general diagram of a multilayer capacitor as depicted in figure 1 Blattau et al. and (right) plot showing achieved dielectric layer thickness versus year from Y. Honda, AEI, p. 48, October (2004)

size, the effects of mechanical stress on domain switching, and early understandings on poling and induced piezoelectric effects. This plethora of knowledge led to a boom in ceramic capacitors, with barium titanate at its core, helping the initial push for miniaturization. As technology continued the path of miniaturization, devices quickly became more nuanced and demands for capacitors of higher volume efficiency were realized in the invention of MLCCs.

Multilayer ceramic capacitors are composite brick capacitors of sandwiched dielectric layers between alternating metal electrodes electrically connected in parallel with encapsulating metal caps on opposite ends. They are generally formed as green-bodies and fired as individual units in reducing atmospheres. The diagram observed in **Fig. 1.2 (left)** [28] shows the general design of an MLCC. Since its conception between the late 1950’s and late 1960’s for use in the Apollo space program, multilayer ceramic capacitor technology has been consistently improved upon for the past two decades, though mainly in engineering of the dielectric layer thickness of the device as discussed above and seen in **Fig. 1.2 (right)**. As the capacitance of a normal (vacuous) parallel plate capacitor is a function of the area of the capacitor plate and the thickness between the plates, it follows that the capacitance of an MLCC is a function of not only the area and thickness of the dielectric layer, but also a function of the number of layers as seen in the equation from section 1.1. The capacitance density of an MLCC then increases simply with decreasing thickness of the dielectric layers and increasing number of layers. However, these variables are limited by device form factors and theoretical limits on layer thickness. Therefore, the development of higher k materials is the only route forward for developing MLCCs of similar or higher capacitance while lowering the form factor, with the included significant challenge of temperature dependence. Currently the main route to solve the challenge of temperature independent high permittivity responses is though composite materials.

1.1.4 Composite Approach

To mitigate problems imposed by the temperature dependence of the dielectric properties, composite microstructures that exploit non-stoichiometric barium titanate are utilized. It is well known that phase transition temperatures in barium titanate can be shifted in temperature space with either doping or defect incorporation through oxygen vacancies. Therefore, composites of various compositions of non-stoichiometric barium titanate can be developed in which the overall permittivity of the composite capacitor would be an integration of the permittivity of all components. This allows for a new family of materials with a temperature-stable high permittivity, one well-known being X7R barium titanate. As the X7R moniker is coded from **Table 1.1**, there are various versions of X7R barium titanate. While some X7R composites are based on oxygen deficient barium titanate, the

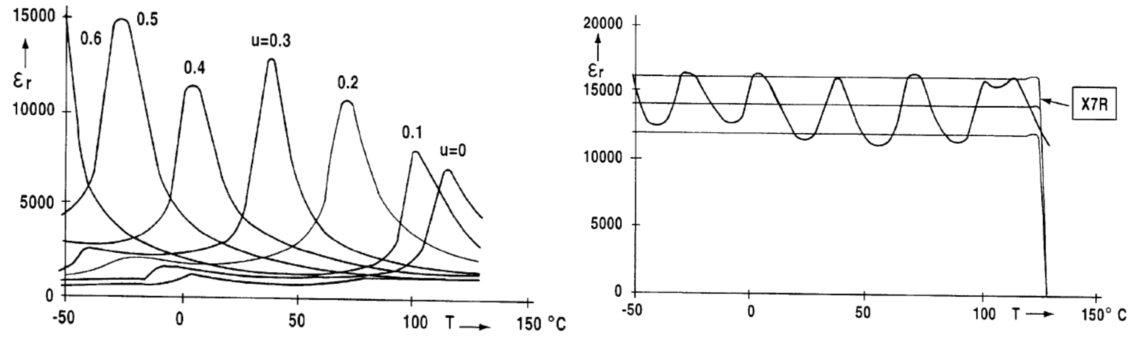

Figure 1.3: Relative permittivity of $(Ba_{(1-u)}Sr_u)TiO_3$, as seen in U.S. Patent 6108191 filed by Bruchhaus et al. in 2000, as a function of Sr composition in individual compositions (left) and a single composite structure (right)

X7R composite seen in **Fig. 1.3** [29] is a composite of strontium doped barium titanate. While a good approach to obtain high permittivity materials with low temperature dependence, composite materials suffers from homogeneity issues, as each individual composition undergoes a phase transition at each peak observed in **Fig. 1.3**. This constant cycling of phase transitions in the composite imposes stress/strain issues that can result in defect agglomeration. These generally build at high energy surfaces or interfaces, especially electrode-dielectric interfaces and can lead to delamination. This work will focus solely on permittivity of non-composite systems with the knowledge that any materials system with high-permittivity compositions that vary in T_{max} through composition, or defect chemistry, are good candidates for further composite engineering studies.

1.1.5 Maxwell – Wagner and the Internal Barrier Layer Model

Another manner to artificially obtain temperature-stable high permittivity materials is through the internal barrier layer model. In this model, conducting grains surrounded in an insulative grain boundary matrix (or conversely, insulating grains surrounded by conductive grain boundary matrix,) allow the material itself to act as a composite array of individual capacitors, with each capacitive element located at the grain boundaries. This

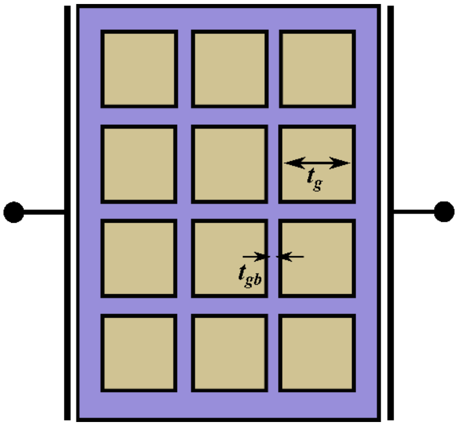

Figure 1.4: Hypothetical brick-wall diagram of conducting grains sized t_g (bricks) and insulating grain boundaries sized t_{gb} (mortar) representative of the internal barrier layer model.

model, visualized in **Fig. 1.4**, gives rise to very high capacitances and, effectively, “extrinsic” permittivities that can be as high as $1\text{x}10^6$ or greater that are not respective of the actual materials property. This model can also be described by the Maxwell-Wagner model of a two-phase dielectric medium [8],[9]. As both models rely on charge buildup on interfacial surfaces, the realized gain to the capacitance of the device will be lost upon application of an electric potential strong enough to excite charge carriers into the conduction band. The voltage needed for such excitation is generally low, and therefore these materials behave more like a resistor under relatively low applied fields ~ 10 kV/cm. As these devices must be able to work under varied applied fields, materials with high permittivities due to these secondary effects are generally undesirable for MLCC applications.

In fact, it was reported by *Lukenheimer et al.* [30] that the majority of ‘colossal’ permittivities observed in oxide-based high permittivity materials can be attributed to these secondary mechanisms. Therefore, greater scrutiny and analysis of the voltage, or field, dependence of these materials is paramount in the search for high permittivity materials.

1.2 Classes of Materials

Regarding electronic materials, they are generally grouped into three classes: conducting, semi-conducting and insulating. While all are important in their own regard and, in concert, can work together to develop society and planet-changing technologies, the scope of this work will focus mainly on insulating materials. Namely, this work will focus on dielectric materials, in addition to ferroelectric and piezoelectric materials, especially with regards to high permittivity and high temperature dielectric materials.

1.3 The Dielectric Effect

The dielectric effect is the displacement of charge under the application of an external electric field. As all matter consists of atoms that displace their electrons under such conditions, all materials exhibit the dielectric effect. However, if a material does not have an incipient energy barrier to conduction, i.e. conductive or non-insulating materials, any charge displaced by the dielectric effect will result in free electron transport through the system, or conduction. This phenomenon is defined by dielectric displacement, $\vec{\boldsymbol{D}}$, a vector parallel to applied field that is governed by the materials property of permittivity, ε. A materials permittivity is its inherent ability to resist the application of an external field through the mechanism of dielectric displacement and is shown here:

$$\vec{\boldsymbol{D}} = \varepsilon\vec{\boldsymbol{E}}$$

Note that for the permittivity for an isotropic material is a scalar quantity, however, for general cases of anisotropy, ε is a second rank tensor with units of farad per meter. Also note, however, that the dielectric displacement within a sample is not the same as its dielectric constant, κ. A materials dielectric constant, κ, is defined as its relative permittivity, ε_r, or the ratio of the materials property, ε, to that of the permittivity of free space, ε_0, as shown here:

$$\kappa = \varepsilon_r = \frac{\varepsilon}{\varepsilon_0}$$

This relation arises from the insertion of a dielectric material into the free space of a parallel plate capacitor which will be discussed in a later section. Notice that κ is a dimensionless constant that directly represents a materials property, ε. Therefore, the relationship between the dielectric displacement vector, $\vec{\boldsymbol{D}}$, within a material and its dielectric constant, κ, representing the materials property, is:

$$\vec{\boldsymbol{D}} = \varepsilon_r \varepsilon_0 \vec{\boldsymbol{E}} = \kappa \varepsilon_0 \vec{\boldsymbol{E}}$$

1.3.1 Origins of Dielectric Displacement and Polarization

With this simple definition of the dielectric effect, it can be easily seen that various components of matter will give rise to this dielectric displacement, as any electronically active component of a material with a fixed or net charge, q, will displace, $\vec{r}$, under an external applied field, $\vec{\boldsymbol{E}}_{\boldsymbol{ex}}$, generating a static or average dipole moment, $\vec{\mu}$. Note that this does not exclude components of neutral charge at equilibrium. This dipole moment will have units of Coulomb-meter and can be directly seen in **Fig. 1.5a** and is summarized here:

$$\vec{\mu}_i(\vec{\boldsymbol{E}}_0) = q \cdot \vec{\mathrm{r}_\imath}$$

Where 'i' represents some charged component of a material, $\vec{r_\imath}$ is the separation distance, d_i measured from the center of the negatively charged moment to that of the positive, dotted with the unit vector, $\overrightarrow{\boldsymbol{E_0}}$, of the applied electric field. Inherent static dipoles will align

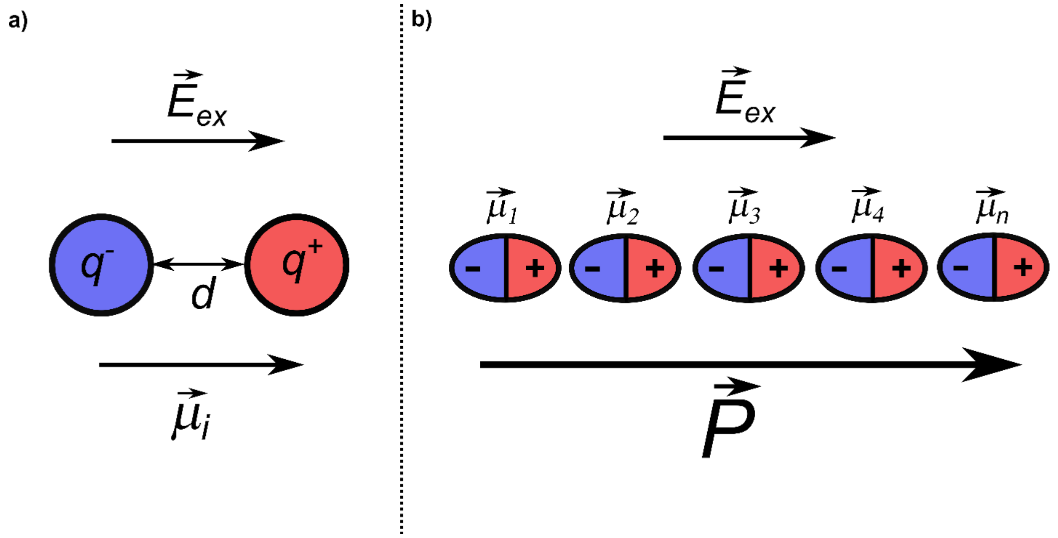

Figure 1.5: a) Diagram of an elementary dipole and effective dipole moment aligned with an external electric field and b) an infinite one-dimensional array of dipoles aligned with an external electric field and their resultant polarization

themselves with the applied field due to torsion forces and charge neutral equilibrium components (i.e. a neutral atom) will displace to form dipoles in alignment with the applied field. These two factors, q and $\vec{r}$, contribute directly to the overall dielectric constant, κ, and therefore permittivity, ε, of the material. As q normally remains fixed in a dipole, the largest potential contributor to a materials permittivity is $\vec{r}$.

Moving further, if this idea of a dipole moment is applied to an ideal infinite array of an indistinguishable chargeable species **Fig. 1.5b**, each unit of this array will experience an equal yet individual dipole moment in response to $\vec{\boldsymbol{E}}$. The summation of all these dipole moments in the array is known as the polarization, $\vec{\boldsymbol{P}}$, of the array and is shown here:

$$\vec{\boldsymbol{P}}(\vec{\boldsymbol{E}}_0) = \sum_{N=1}^{\infty} N_{\vec{\mu}_i}\vec{\mu}_i\,(\vec{\boldsymbol{E}}_0)$$

Where N represents an individual dipole moment. Note that to extrapolate this to a multi-dimensional array, a simple area (2D) or volume (3D) term would be added to the denominator of the summation, and the equation would take on a number density form:

$$\vec{\boldsymbol{P}}(\vec{\boldsymbol{E}}_0) = \sum_{N=1}^{\infty} \rho_{N,\vec{\mu}_i} \vec{\mu}_i \, (\vec{\boldsymbol{E}}_0)$$

Here, $\rho_{N,\vec{\mu}_i}$is the number density of dipole moments per unit volume of the array. Now, substituting in the coulombic representation of the dipole moment we find:

$$\vec{\boldsymbol{P}}(\vec{\boldsymbol{E}}_0) = \sum_{N=1}^{\infty} \rho_{N,\vec{\mu}_i} q * d \cdot \vec{\boldsymbol{E}}_0$$

Remembering,

$$\rho_{N,\vec{\mu}_i} = \frac{N}{V}$$

And assuming our three-dimensional array of dipoles is surrounded by a cylindrical prism of length *d* and base surface area *A* then,

$$\vec{\boldsymbol{P}}(\vec{\boldsymbol{E}}_0) = \sum_{N=1}^{\infty} \frac{N * q * d_i}{A * d} \cdot \vec{\boldsymbol{E}}_0$$

And, as the sum of all individual dipole moments in the array, *N*, and their charge, *q*, is simply the total charge Q_T then:

$$\vec{\boldsymbol{P}}\big(\vec{\boldsymbol{E}}_0\big) = \frac{Q_T}{A} \cdot \vec{\boldsymbol{E}}_0$$

Or,

$$\vec{\boldsymbol{P}} = \frac{Q_T}{A} \cdot \vec{\boldsymbol{E}}$$

Which represents of the total accumulated charge density on the surface, A, of the indefinite cylindrical prism enclosing an infinite three-dimensional array of dipoles, like that depicted in **Fig. 1.5b**. Considering this hypothetical polarized cylindrical prism with a charge density of +σ_T on one surface, and a correlative -σ_T on the opposing surface, the basis for an analogous parallel plate capacitor becomes apparent where,

$$\sigma_T = \frac{Q_T}{A} \;, \qquad \vec{\boldsymbol{P}} = \sigma_T \vec{\boldsymbol{E}}$$

Note that, as the magnitude of $\vec{\boldsymbol{D}}$ is the total charge density, σ_T (or total displaced charge,) the polarization vector and dielectric displacement of this idealized material are equivalent:

$$\vec{\boldsymbol{P}} = \left|\vec{\boldsymbol{D}}\right| \cdot \vec{\boldsymbol{E}} \equiv \vec{\boldsymbol{D}}$$

1.3.2 The Parallel Plate Capacitor

Building from the hypothetical situation posed above, if both charged surfaces of the cylinder were covered with perfectly flat, conductive plates, both plates were connected to a source of electric potential, *U*, and subsequently all matter was removed from within the cylinder, the resultant circuit would be a parallel plate capacitor as depicted in **Figure 1.6a**. As the plates of this capacitor are separated by vacuous free space, the electric field across this capacitor, as well as its overall capacitance, are defined by the permittivity of free space, ε_0, summarized from Fig. 1.6a here:

$$C_0 = \frac{Q_T}{U} = \varepsilon_0 \frac{A}{d}; \; \vec{\boldsymbol{E}} = \frac{\sigma_T}{\varepsilon_0}$$

From this electric field definition, the naught, $\vec{\boldsymbol{D}}_0$, dielectric displacement relationship can also be defined:

$$\vec{\boldsymbol{D}}_0 = \varepsilon_0 \vec{\boldsymbol{E}}$$

As the total charge accumulation on the plates due to the vacuum is equivalent to the total charge displaced from the insertion of a dielectric material with permittivity of free space.

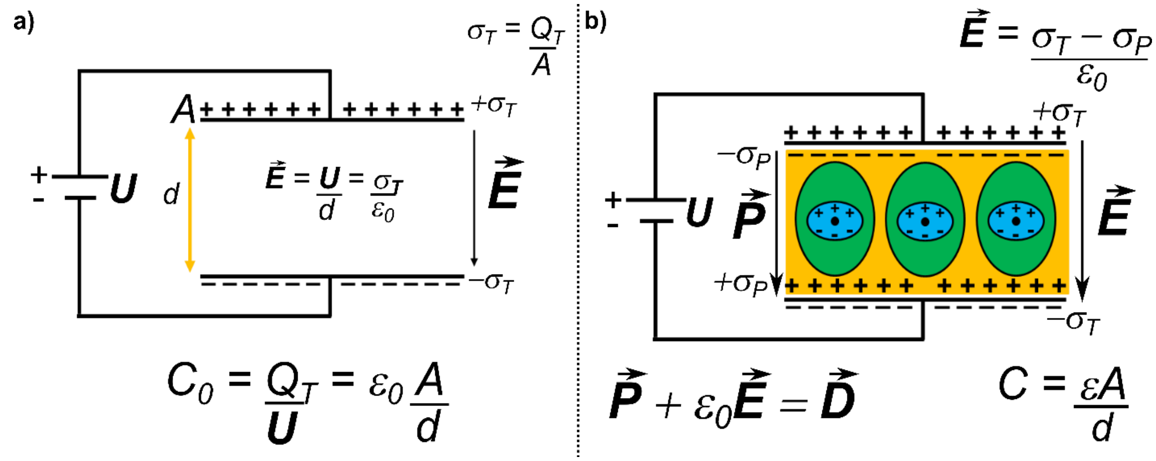

Figure 1.6: a) Schematic of a parallel plate capacitor of two plates with equal area, A, separated by a vacuum with discrete distance, d (or volume A*d), attached to a potential source, U, and b) insertion of a dielectric material into free space of a parallel plate capacitor, subsequent dipole formation within the material (denoted by oblong circles between plates) generating the polarization, $\vec{\boldsymbol{P}}$, leading to complementary charge buildup on surface of the dielectric material, σ_p, a and its effect on the overall electric field across the capacitor

More interestingly, if a dielectric material of discrete permittivity ($\varepsilon > \varepsilon_0$) is inserted between these plates, complementary charge, σ_p, will begin to build up on the surface of the dielectric material as depicted in **Fig. 1.6b**. This complementary charge 'resists' applied electric field by effectively reducing the overall charge generating the applied field:

$$\vec{\boldsymbol{E}} = \frac{\sigma_T - \sigma_P}{\varepsilon_0}$$

The resultant capacitance is therefore increased as the effective potential, ***U***, is decreased proportionately to $\vec{\boldsymbol{E}}$, and the permittivity of the inserted dielectric material contributes to that of free space through its dielectric constant κ:

$$C = \frac{\varepsilon * A}{d} = \frac{\varepsilon_r \varepsilon_0 A}{d} \ or \ \frac{\kappa \varepsilon_0 A}{d}$$

Note that, for experimentally measured capacitance values, a materials dielectric constant can be calculated by solving for *κ*, with a sample of known area, *A*, and thickness, *d*:

$$\kappa = \frac{C'\varepsilon_0 A}{d}$$

Where *C'* represents an experimentally measured capacitance of a parallel plate capacitor. Another consequence of complementary charge buildup can be seen through the induced polarization of the dielectric medium. Remembering that the polarization is the net sum of all dipole moments within the material, we can see that there are multiple contributions to $\vec{\boldsymbol{P}}$:

$$\vec{\boldsymbol{P}} = \vec{\boldsymbol{D}} - \vec{\boldsymbol{D}}_0$$

In other words, the resultant polarization of the dielectric material is difference between the overall charge density displaced and the naught dielectric displacement of the empty capacitor. Given our previous definition of $\vec{\boldsymbol{D}}_0$ and $\vec{\boldsymbol{D}}$, we can see that,

$$\vec{\boldsymbol{P}} = \vec{\boldsymbol{D}} - \varepsilon_0\vec{\boldsymbol{E}} - or - \ \vec{\boldsymbol{D}} = \varepsilon_0\vec{\boldsymbol{E}} + \vec{\boldsymbol{P}}$$

Also,

$$\vec{\boldsymbol{P}} = \varepsilon_r\varepsilon_0\vec{\boldsymbol{E}} - \varepsilon_0\vec{\boldsymbol{E}}$$

Which simplifying gives:

$$\vec{\boldsymbol{P}} = (\varepsilon_r - 1)\ \varepsilon_0\vec{\boldsymbol{E}} \equiv (\kappa - 1)\ \varepsilon_0\vec{\boldsymbol{E}}$$

Now, if the dielectric is a ‘linear’ dielectric (which will be further discussed in a later section), its polarization can also be defined by its electric susceptibility, χ_e:

$$\vec{\boldsymbol{P}} = \chi_e\varepsilon_0\vec{\boldsymbol{E}}$$

Where the electric susceptibility is a dimensionless constant and a second rank tensor. As the applied field and the resultant polarization are assumed to be collinear in a capacitor, the relationship between a materials electric susceptibility and the dielectric constant, κ, is,

$$\chi_e = \kappa - 1\ \therefore \frac{\varepsilon}{\varepsilon_0} = \chi_e + 1$$

1.3.3 Mechanisms of Dielectric Displacement and Polarization

With the viewpoint building from that of a single atom to a real complex polycrystalline material, multiple charge displacement mechanisms in which these dipole moments can be formed arise. These mechanisms give rise to various contributions to the materials permittivity and are defined as atomic displacement, ε_{atomic}, ionic displacement, ε_{ionic}, displacement of incipient dipoles, ε_{dipole}, and inertial displacement of space charge, ε_{sc}. Therefore, the materials overall permittivity can be defined as the sum of these contributions:

$$\varepsilon = \varepsilon_{atom} + \varepsilon_{ion} + \varepsilon_{dipole} + \varepsilon_{sc}$$

In each of these mechanisms, the charged species that gives rise to a dipole moment have a different effective mass and therefore will have various relaxation times, or frequency dependencies, $\omega(t)$. Also, note that the magnitude of contribution to the dielectric constant for each mechanism varies, as each has individual constraints on the extent of its possible displacement distance, $\vec{r}$. For instance, ε_{sc}, is the largest possible contributor as space charge is able to freely move through the bulk conduction band of a material and accumulate on defect interfaces and boundaries (e.g. grain boundaries, line defects, etc.) in the material. This effectively gives rise to relatively large values of $\vec{r}$, equivalent to the average value of the grain size. Dipole contributions, ε_{dipole}, are the next highest contributor as, within complex polycrystalline materials, these fixed dipoles originate from crystallographic inhomogeneity within a grain. That is regions of homogenously aligned unit cells with similar dipole moments dispersed heterogeneously throughout a crystallite. In ceramic metal oxides these dipole moments arise from average charge displacement in ionic bonds. Therefore, it follows that possible values of $\vec{r}$ for

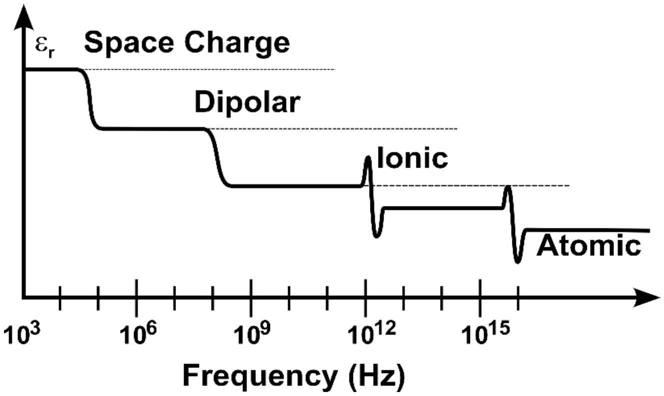

Figure 1.7: Hypothetical frequency dependence for unique components of the dielectric constant with relative contribution to its magnitude.

dipole contributions are smaller than that of the average grain size, yet much larger than that of dipole moments from purely ionic contributions, ε_{ion}, that have $\vec{r}$ values on the order of magnitude equivalent to the ionic bond length. Lastly, the smallest contributor to the overall permittivity would be that of ε_{atom}, which all matter contains, as the possible displacement distances are limited to individual atomic orbitals. This general relationship can be seen in **Fig. 1.7**, and is summarized here:

$$\varepsilon_{atom} < \varepsilon_{ion} < \varepsilon_{dipole} < \varepsilon_{sc}$$

Also note from **Fig. 1.7** that these mechanisms can either be continuous or discontinuous with respect to frequency. This arises from the mode in which the dipole is formed or re-arranged and can give rise to various interesting characteristics of the dielectric constant.

1.3.4 Frequency Dependence

If the dipolar formation, or re-arrangement, resultant from the applied electric field requires diffusion of atoms or ions, or more simply the breaking of symmetry elements within the crystallite, as is the case for ε_{atom} and ε_{ion}, then there will be an activation

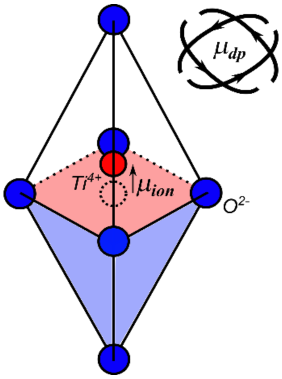

Figure 1.8: Example of a TiO_6 octahedron with Ti^{4+} cation displaced from its equilibrium bond position generating a dipole moment under the application of an external field. The displacement process for generating this structure is an example of ionic polarization, where the octahedron itself becomes a dipole. However, if this non-equilibrium structure is inherent in a material, the reorientation of the octahedron with the applied field is an example of dipolar polarization.

energy, E_a, of equivalence to the bond strength felt by the diffusing, symmetry breaking, species at ground state. As diffusion is a rate determined process, as defined by the Arrhenius equation, that is determined the vibrational frequency, or jump frequency, of the diffusing species as well as the potential energy barrier (E_a), it follows that a discrete frequency will exist where all diffusing species will be able to instantaneously overcome E_a, leading to the observed discontinuity or sinusoidal behavior observed in **Fig. 1.7**. This phenomenon is tied to crystallographic first-order phase transitions in a material, and is therefore temperature dependent, and results in large gains to κ over very limited temperature ranges that do not vary with frequency.

More interesting are the cases that give rise to continuous behavior with respect to frequency, ε_{dipole}, and ε_{sc}. In these mechanisms charge, or fixed dipoles, can move and re-arrange freely until inhibited by an energy barrier. In the case of ε_{sc}, charge carriers within the conduction or valence band can move freely with the applied electric field until inhibited by a discontinuity in the band structure, i.e., a defect surface or grain boundary. As for ε_{dipole}, fixed dipoles, such as the Ti^{4+} ion within the TiO_6 octahedron depicted in

Fig. 1.8, within the crystallite can move and re-orient freely as the process does not involve diffusion and involve only slight distortions away from equilibrium positions. Unlike the polarization mechanisms that require diffusion, these mechanisms are continuous and can lead to frequency dependence in κ, namely dipolar, as dipoles of different size and magnitude will reorient in the applied field at different rates. To elucidate these mechanisms, alternating current is used so that capacitance can be measured at varying frequencies, isolating the contributions to the overall permittivity.

1.3.5 Complex Permittivity

Thus far, the discussion has only focused on hypothetical, ideal, dielectric materials. As dielectric materials are insulators, it is assumed that the ideal dielectric is a perfect insulator with zero energy dissipation or loss. In real materials, this is not the case. The main form of loss in a dielectric material is energy dissipation through resistive heating. With all materials considered in this work being bulk polycrystalline ceramics which contain inherent defects, namely grain boundaries and impurities, this energy dissipation can be largely attributed to conduction losses through defects and cations with unfilled bonding orbitals. While proportionally more conductive than the bulk of the material, these grain boundaries are mainly resistive due to small mean free paths, and therefore conducting species in grain boundaries will result in resistive heating. Note that the mean free path, in this case, is closely tied to the average grain size. Furthermore, as earlier defined, displacing space charge within a dielectric contributes to the overall dielectric displacement through and increase to the relative permittivity. This apparent increase to the dielectric constant is non-real and is considered as the complex permittivity:

$$\varepsilon_r = \varepsilon_r' + i\varepsilon_r''$$

Experimentally, this energy dissipation is measured as the 'loss factor' or *tan* δ, where δ is the phase angle between the capacitive current and the overall current and its relationship with the real and non-real parts of the dielectric constant is:

$$\tan\delta = \frac{\varepsilon_r''}{\varepsilon_r'}$$

1.4 Linearity and Non-Linearity in Dielectrics: Ferroelectricity

One large assumption made until this point is that the hypothetical dielectric material responds to the applied electric field in a linear manner. From the expanded definition of the dielectric displacement, we see that, if plotted against the applied field, our dielectric displacement behaves linearly with a slope, *m*, of:

$$m = \kappa * \varepsilon_0$$

Or in the experimental case of polarization vs. electric field:

$$m = (\kappa - 1) * \varepsilon_0$$

Consequentially, a linear dielectric can be polarized under the application of an electric field and that polarization will be lost with removal of the applied field. These materials are commonly referred to as paraelectric. However, not all dielectrics are paraelectric. There are a variety of non-linear dielectric materials and one of the more common examples is the ferroelectric material which exhibits a 'switching' phenomena first discovered in analogous ferromagnetism. 'Switching' is more aptly described as instantaneous polarization within a material that can be reoriented with an external electric

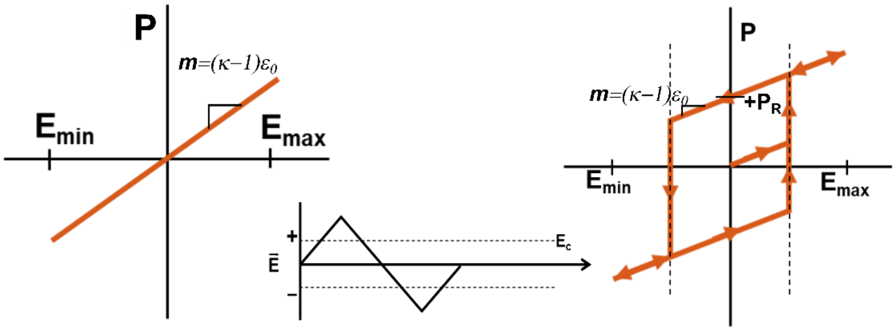

Figure 1.9 idealized polarization response to an applied electric field of triangular waveform for (left) a linear dielectric, or paraelectric material, and (right) a non-linear dielectric, or ferroelectric material.

field, and as the induced polarization from an applied external field generates its own self-sustaining internal electric field. The field at which non-linearity occurs is known as the coercive field, $\boldsymbol{E_c}$, and a non-linear ferroelectric material will behave as a normal linear dielectric at all fields other than $\boldsymbol{E_c}$. Another notable consequence of non-linearity is that, once formed, the polarized units remain within the material upon removal of the applied field. This zero-field polarization is known as remenant polarization, P_R, and can be flipped in sense upon application of $\mathbf{-E_c}$ (thus the term ‘switched’). The process of forming these polarized units is called poling and can be used to artificially increase a materials permittivity, as it adds to the inherent zero-field ε_{dipole}. Note that this gain to the permittivity is anisotropic, as the spontaneous polarization only exists in the direction in which the material was poled, and that ferroelectric phases of materials generally have higher dielectric constants due to incipient dipoles within the material even at ground state.

Finally, once a material is poled, the polarized state of the material will not return to zero unless sufficiently thermally annealed for it to undergo a paraelectric phase transformation. Remenant polarization may reduce over time, however, as the polarized units may relax via defect diffusion to reduce the systems overall internal strain. Idealized plots of polarization versus electric field for hypothetical paraelectric and ferroelectric material are shown in **Fig. 1.9** to help elucidate this phenomenon.

1.4.1 Domains and Ferroelectricity

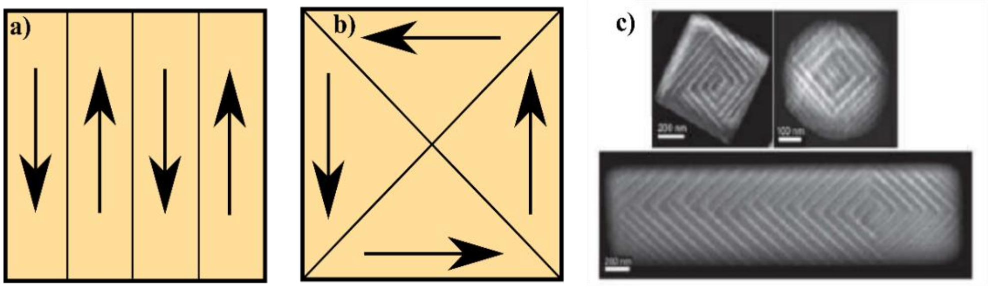

Figure 1.10: Idealized examples of a) 180° domains, b) 90° domains and c) ferroelectric domains in $BaTiO_3$ through electron microscopy as reported by *Scott et al.* [31]

The polarization seen in **Fig. 1.9** above is idealized and, in fact, would only be possible from a perfect single crystal with only one alignment of unit cell. This type of response would never be possible, though, even in a single crystal. Polarized unit cells add to the overall entropy of the system through the electric potential of the self-stabilizing electric field so, if all polarized unit cells in a single crystal are aligned in tandem, this would result in a non-equilibrium structure that could not exist without the stabilization from some external stressor. This non-equilibrium effect is countered by entropic gains arising from dipole moment direction, that is unit cells develop a new source of degrees of freedom when polarized. It follows that, if all unit cells in a crystal share the same dipole moment sense, entropy would be minimized, and the system would be thermodynamically unfavorable. Therefore, to increase the thermodynamic favorability of the system, unit cells will align with like sense in small regions within a crystallite. This correlation of like-polarized unit cells is known as a domain, the correlation length is the domain size, and the finite boundaries that separate these regions are known as domain walls. For a tetragonal ferroelectric crystallite to form at equilibrium there are two common types of domain walls: 180° and 90°. Antiparallel domain boundaries, 180°, are most efficient at establishing equilibrium, while 90° and other angle boundaries are less efficient, examples can be seen in **Fig. 1.10** with incorporated data from *Scott et al*. [31].

At ground state, domains are generally small, dispersed randomly, of large density within a grain, and relatively mobile. Domains will re-orient and grow together under the application of sufficient field, increasing their polarization magnitude, though lowering their density and relative mobility. However, these fields tend to be relatively high (generally > 15 kV/cm), much higher than normal fields used within capacitor devices. The contribution of domains to an un-poled materials overall permittivity is therefore mostly due to domain wall motion, as the polarization magnitude of un-poled domains is small. In fact, domain wall motion gives rise to variations in the polarization of a grain, ΔP, which (for highly mobile domains) can be very high and is the main contributor to the materials permittivity and ε_{dipole}.

1.4.2 The Curie Temperature

While these domains form inherently in ferroelectric materials, materials contain various crystallographic phases of which not all are ferroelectric phases. In fact, ferroelectric materials have either a first or second order phase transition from a ferroelectric phase to a paraelectric phase. As this work focuses on perovskite materials, the most common ferroelectric phases are tetragonal and rhombohedral while the paraelectric phase is most commonly cubic. As the cubic phase is of higher symmetry, it is commonly a high temperature phase, and the temperature at which a material transitions from a ferroelectric (FE) phase to a paraelectric (PE) phase is known as the Curie temperature, T_c [32]. Paraelectric phases are non-polar and therefore cannot be polarized or form domains. Consequentially, cooling through the T_c, spontaneous formation of domains is observed with a large gain to the materials permittivity, and therefore the T_c is generally (though sometimes incorrectly) correlated to a materials maximum dielectric constant, κ_{max}, in ferroelectric materials.

1.4.3 Relaxor Ferroelectrics

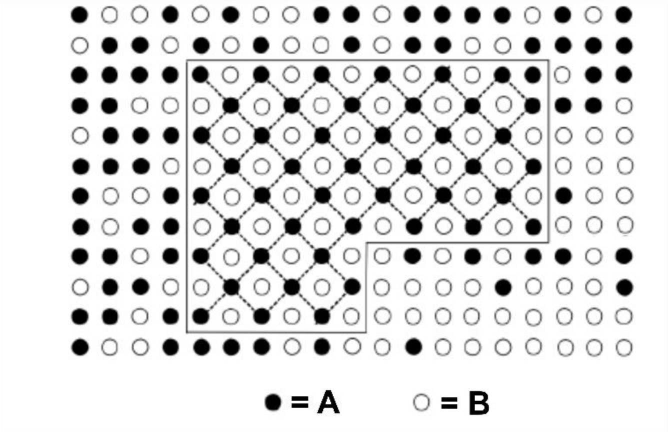

Figure 1.11: Hypothetical array of two distinct species, A and B, distributed in a homogeneous periodic array and inhomogeneous dispersions of only A, only B, or non-ordered mixtures of A and B while maintaining equal atomic ratios of A and B. Figure adapted from the original as developed by *Bokov and Ye* [33]

An important mechanism in solid state phenomena to increase the overall entropy of a FE is chemical inhomogeneity. As the formation of domains lowers the Gibbs free energy of the system through periodic arrangement of crystallographically identical unit cells, chemical inhomogeneity lowers the overall Gibbs free energy through inhomogeneous dispersion of ions on a local, nanometer, scale. This effect can be visualized in **Fig. 1.11** as adapted from Bokov and Ye [33], where a hypothetical array of equal components *A* and *B* can be arranged in various configurations while maintaining the same local atomic ratio: a homogenous periodic array of *A* and *B*, or inhomogeneous dispersion with regions of only species *A*, only species *B*, or non-ordered mixtures of *A* and *B*. In some FE systems, this inhomogeneity is incorporated by small, nanometer-sized, regions of the ordered, polar, FE phase being separated by the inhomogeneous distribution (matrix) of identical stoichiometry. These systems are called relaxor ferroelectrics (RFEs,) and these ordered polarized regions are commonly referred to as nano polar regions (PNRs.) While there are currently various theorized models of how this inhomogeneity gives rise PNRs, they have been regularly observed and their existence has been widely confirmed using inelastic neutron scattering, piezo-response microscopy, refractive index, and single crystal diffraction [34]–[38].

While this inhomogeneity of the cubic matrix is non-ground state, the high density, and relatively small correlation lengths, of PNRs allow for their entropic gain to the system to out-weigh the increase to the systems enthalpy. Furthermore, while the cubic matrix is in-homogenously dispersed, the stoichiometries of these regions are identical, and therefore the overall stoichiometry of the material will be uniform. The bulk structure will then be an average of all PNRs in the material, as well as the in-homogenous bulk crystal matrix in which they exist.

Most commonly, the bulk matrix in these systems is cubic and therefore, these materials are identified as ‘pseudo-cubic,’ for metrically they appear cubic yet exhibit ferroelectric properties which are symmetrically not allowed by a cubic, centrosymmetric, crystal system.

More interestingly, RFEs exhibit diffuse phase transitions and a frequency dependence of the dielectric constant, which can result in a material exhibiting a large value

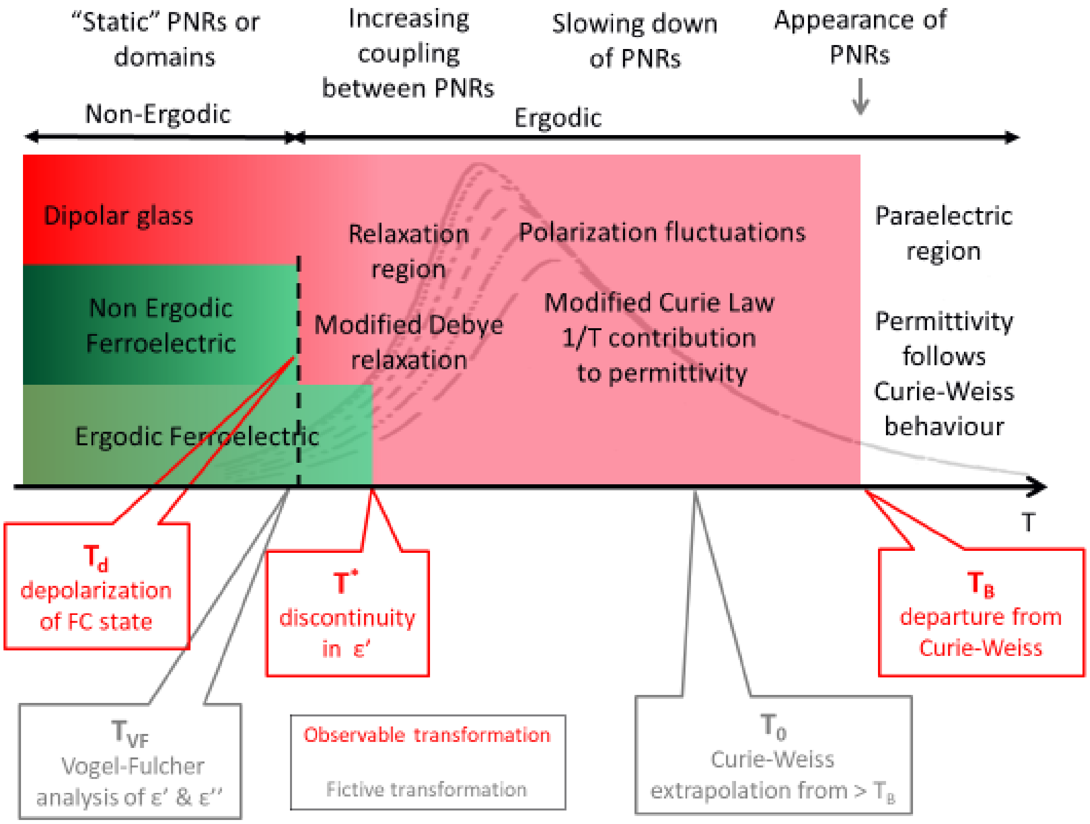

Figure 1.12: Relaxor ferroelectric diagram of the permittivity versus temperature response of a real RFE which exhibits and summarizes the phenomena inherent to relaxor ferroelectrics as developed by Andrew Bell [39]

of κ over a wide temperature range. Identical to FE materials, RFEs exhibit a cubic PE phase at high temperature, though cooling through the PE to RFE phase transition temperature does not give a normal Curie temperature-like transition. Instead, RFEs exhibit a continuous, frequency dependent, peak in the permittivity, and the PE – RFE transition temperature is referred to as the Burns temperature, T_B. This frequency dependence can be described as a dynamic interaction of the applied field with PNRs of varied size, each with its own size dependent relaxation constant, and apparent T_c. The region beneath the Burns temperature is known as the ergodic region, and in this region PNRs form within the cubic crystalline matrix. PNRs are formed with a size distribution equivalent to that of a

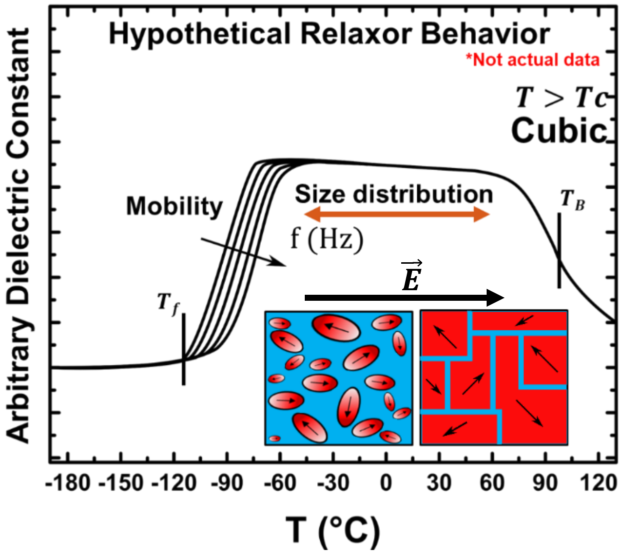

Figure 1.13: Hypothetical relative permittivity versus temperature data for an idealized relaxor material showing the ergodic region where the peak breadth is dependent on the size distribution of PNRs growing at onset of T_B and the frequency dispersion due to PNR mobility. Theorized models of PNR formation are seen as (bottom right) polar nano regions in a inhomogenous crystalline matrix and (bottom left) ordered polar ferroelectric regions (domains) in a cubic-like domain walls. Models are inspired by Bokov and Ye [33]

Maxwell-Boltzmann distribution, are mobile and dynamic, and their average structure approaches that of the cubic matrix, hence the term ergodic from statistical mechanics. These RFE characteristics are summarized and described visually in **Fig. 1.12**.

As temperature decreases, these regions begin to lose mobility until completely immobile at the freezing temperature, T_f. At this temperature, the inhomogeneous cubic matrix will either relax and enter a normal FE phase or persist as a non-ergodic, canonical, RFE. As the size distribution of PNRs follows that of a Maxwell-Boltzmann distribution, PNRs are frequency dependent and gives rise to a broad, frequency dependent, peak in the permittivity as a function of temperature. The breadth of observed peak in the permittivity is correlated to the size distribution of PNRs and the extent of frequency dependence is a function of the PNR mobility. Finally, past T_f, ‘frozen’ PNRs exist in a randomly distributed, glassy state and are immobile unless acted upon by an external electric field.

One large consequence of this ergodic PNR behavior is that the material no longer will exhibit an instantaneous switching event, most characteristic of a FE. This frequency dependence of permittivity response due to size distribution and mobility of PNRs is summarized through use of a hypothetical, idealized, RFE permittivity versus temperature response as seen in **Fig. 1.13 [hypothetical]**

1.5 Piezoelectricity and Strain

Another direct, and significant, consequence of dielectric displacement is the piezoelectric effect. More specifically, dielectric displacement in a non-centrosymmetric material gives rise strain in a material, which is known as the indirect piezoelectric effect. Here, the displaced charge generates strain within the material, or a physical deformation of the material, and can be elucidated from the example of ionic polarization given in **Fig. 1.14**. Conversely, and more commonly referenced, the direct piezoelectric effect is defined as the conversion of mechanical energy to electrical energy through a physical deformation of the material generating an induced current within the material. As the symmetry requirements for piezoelectricity is a non-centrosymmetric structure, all ferroelectrics are

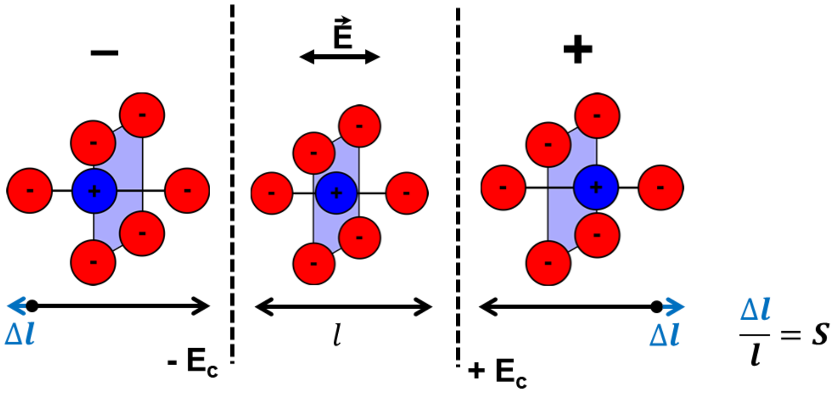

Figure 1.14: Strain generation due to the ionic polarization in an octahedron due to the application of an electric field. The induced strain results in mechanical deformation of a material and is known as the indirect piezoelectric effect.

intrinsically non-centrosymmetric, it follows that all ferroelectric materials are piezoelectric. However, as the qualifier for a polar unit cell is non-centrosymmetry, and not all non-centrosymmetric materials exhibit ferroelectricity, it follows that not all piezoelectrics are ferroelectrics. Piezoelectric materials are characterized by their piezoelectric coefficient, d_{ijk}, a third rank tensor, which is governed, directly, by:

$$\vec{\boldsymbol{D}}_{\boldsymbol{ij}} = d_{ijk}\vec{\boldsymbol{X}}_{\boldsymbol{jk}}$$

Where $\vec{\boldsymbol{D}}_{\boldsymbol{ij}}$ is the displacement field and $\vec{\boldsymbol{X}}_{\boldsymbol{jk}}$ is the applied mechanical stress. Indirectly, they are characterized by the indirect piezoelectric coefficient d_{ijk}^{*} through:

$$\vec{\boldsymbol{S}}_{\boldsymbol{ij}} = d_{ijk}^{*}\vec{\boldsymbol{E}}_{\boldsymbol{jk}}$$

Where $\vec{\boldsymbol{S}}_{\boldsymbol{ij}}$ is the strain field and $\vec{\boldsymbol{E}}_{\boldsymbol{jk}}$ is the applied electric field.

Strain behavior for PE, FE and RFE materials vary, as the switching paradigm in FE materials generates a large instantaneous negative strain, representing lattice rearrangement, in the material. This can be observed in **Fig. 1.15**. As the polarization in PE and RFE materials do not exhibit switching effects, the resultant strain will remain linear and positive, as the strain is resultant of polarized units moving reversibly within a matrix. While this materials property can be very desirable for advanced technologies, it is notably

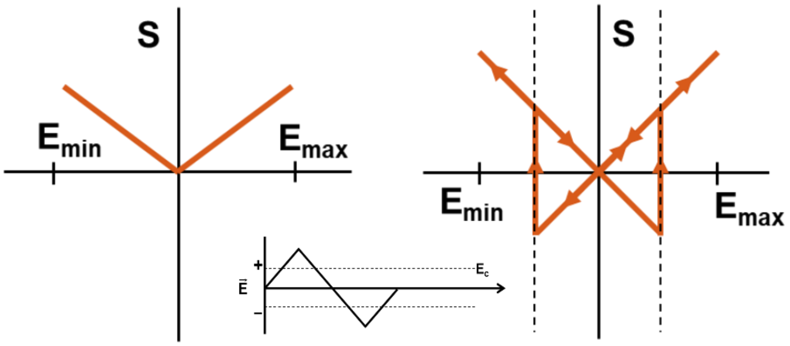

Figure 1.15: Strain behavior of a dielectric material under an applied electric field for a linear dielectric, paraelectric, material and a non-linear dielectric, ferroelectric, material. Note that relaxor ferroelectric materials do not exhibit switching and therefore behave linearly in strain.

undesirable for capacitor applications, as induced strain within a fixed device structure will lead to mechanical instability and device failure.

1.6 Structure – Property Relationships

To better understand the properties discussed above, it is paramount to understand a materials structure. In fact, a materials structure is what allows, and gives rise to, its inherent properties through allowable atomic interactions. A materials structure is determined by how its fundamental building blocks (atoms, ions, etc.) organize to fill space, and their resultant interactions in doing so. In crystalline materials, these building blocks (motifs) arrange themselves periodically in space in a three-dimensional array of mathematically identical points (lattice.) In doing so, they generate a unique structure (unit cell) that is indistinguishable at any translational point within a perfect crystal and whatever symmetry is incipient to the unit cell on a local, nano, scale will be reflected by the material in the macro scale. As real materials are limited finitely, it follows that unit cells cannot repeat indefinitely, and translational symmetry must be broken at some point. These terminations are two-dimensional surface defects known as grain boundaries, given that grains are regions in which unit cells maintain translational symmetry. Grains range widely in size and the density at which they are packed within a polycrystalline material also has a large impact on the materials properties.

1.6.1 The Perovskite Structure

While the world of crystals is filled with a plethora of different crystal structures, (pyrochlore, rutile, wurtzite, sphalerite, etc.) one is paramount in the realm of electroceramics, especially ferroelectric ceramics. That crystal system is the perovskite crystal system. The perovskite mineral was first discovered naturally occurring in calcium titanate ($CaTiO_3$) and is named honorifically after the Russian mineralogist Lev Perovski. This mineral was discovered in Russia by Gustav Rose in 1839 [40], and was first described, much later, by Goldschmidt in 1926 [41]. While not crystallographically solving the structure, Goldschmidts' work resulted in the Goldschmidt tolerance factor (TF), ***t***, which is still commonly used today to accurately approximate the packing in the perovskite structure [42].

$$t = \frac{R_A + R_O}{\sqrt{2}(R_B + R_O)}$$

Where $\boldsymbol{R_X}$ is the ionic radii of specific ionic species in their appropriate coordination environment, and ***t*** defines the phase stability of the structure: perovskites with unity values of ***t*** (***t*** = 1) being ideal simple cubic, those of ***t*** > 1 tending tetragonal and those of ***t*** < 1 tending rhombohedral or orthorhombic. The perovskite structure is generally stable over the range of 0.8 < ***t*** < 1.2.

The publication of the first solved perovskite structure was not published until 1945 on studies of the, then, newly discovered, $BaTiO_3$ system [ref-megaw]. This perovskite structure can be described chemically as ABX_3 where A and B represent cations and X represents a (2-) anion. As this work focuses specifically on metal oxides, X will always be represented by oxygen and thus the chemical formula is ABO_3. For neutrality arguments, A cations are larger and generally of second (II) oxidation state and B cations

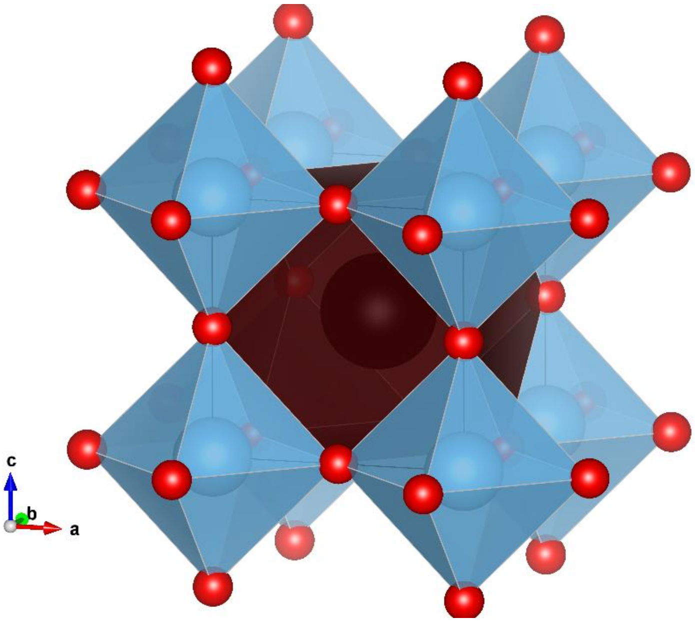

Figure 1.16: Unit cell of $SrTiO_3$ with space group $Pm\bar{3}m$ exemplifying the perovskite structure with a tolerance factor of unity. Sr^{2+} cation is visualized as the largest sphere (center of cuboctahedral,) Ti^{4+} cations are visualized by medium spheres on unit cell corners, and O^{2-} anions are visualized as smallest spheres surrounding Ti^{4+} cations forming octahedrons. The B-site sub lattice of a simple cubic array of corner shared BO_6 octahedra can be seen generating the 12-fold cuboctcahedral A-site.

are smaller and of fourth (IV) oxidation state as the overall anion valence is -6, so the general expanded formula can be written as:

$$A^{2+}B^{4+}O_3$$

However, this generality can be broken as the A and B site can be of any combination of oxidation states generating 6+ overall and allows for aliovalency (is not restricted to isovalent combinations.) This structure is based on cubic-close packing of the anion (O^{2-}) with all resultant, six coordinated, octahedral holes filled by the B cation. This results in a cubic array of corner shared octahedrons, BO_6, such as the TiO_6 example given in **Fig. 1.8** (section 1.3.4.) This is the B-site sublattice, and it generates twelve-coordinated cuboctcahedral voids which are filled by the larger A cations. The ideal perovskite, of ***t*** = 1, has a $Pm\bar{3}m$ space group and is realized by $SrTiO_3$ as seen in **Fig. 1.16**.

1.6.1.1 Solid Solutions and the Perovskite Structure

One very powerful consequence of the perovskite structure is seen through the application of solid solutions. Solid solutions are exactly as they seem, solid-state analogues of liquid-state (solvent-solute) solutions. In the solid-state, solvents are the stoichiometric ions in an ionic solid with discrete structure, sometimes referred to as the ‘parent-structure,’ and solutes are ions of similar valence, ionic size, electronegativity, and preferred coordination. The accepted rules governing the formation of solid-state solutions are summarized by the Hume-Rothery rules [44]. These rules state that the ionic radii of solute and solvent cations must not vary by more than 15%, and that solute and solvent should be of like crystal structure, electronegativity, and valence. Unlike defects, solute species are incorporated by a stoichiometric substitution and therefore incorporate directly onto lattice sites of the solvent species as opposed to interstitial, or vacancy-based, defect sites. Applying solid solutions to the perovskite structure allows for chemical variance such as $(A'A'')(B'B'')O_3$, which can lead to complex phenomena such as the relaxor effect discussed above. In fact, there is no fixed limit to the amount of substitution of a lattice site so long as the solutes agree with the Hume-Rothery rules. Notably this has been realized within the last decade in high entropy materials which contain five or more cations in one lattice site [45]–[48].

While the Hume-Rothery rules are reasonable guidelines, they are not governing laws. In fact, solid solutions of aliovalent cations, cations of different valence, are commonplace and have large implications for perovskite materials. Looking at the B-site of the perovskite, aliovalent substitutions, as well as substitutions of different ionic size, can lead to subsequent distortions in the surrounding O^{2-} bonding array, generating a wide variety of distortions in the BO_6 octahedra. These distortions can give rise various subsequent properties and are the main form of dipole generation in a perovskite unit cell. Note that similar substitutions can be made on the A-site and these substitutions are also accommodated by octahedral distortion. However, A-site substitutions of deviated ionic radius are generally accommodated by octahedral tilting, though they can lead to distortions of the BO_6 bonding array.

1.6.1.2 Jahn-Teller Distortions and Common Phases of Perovskites

There are multiple types of octahedral distortions in a perovskite though they can be generalized into two types: distortion of the octahedra and octahedral tilting. Distortion requires a deviation from equilibrium bond distances and tilting is symmetric rotation of a static octahedra around a fixed point. These octahedral distortions can be well described by the Jahn-Teller effect [49] and, within a perovskite material, are tied closely to the tolerance factor. The Jahn-Teller effect describes two mechanisms leading to distortion, first order and second order. To describe these effects, it is helpful to look at the rotational symmetry of a perfect octahedron, that is it contains three indistinct rotation axes of four-fold symmetry. In first order distortions, the octahedron is elongated or contracted through breaking of orbital degeneracy [49].[50] which induces tetragonality in a perovskite unit cell. In this distortion, four-fold symmetry is maintained along one of the rotational axes, while the other two axes are reduced to two-fold rotational symmetry. Second order Jahn-Teller distortions are characterized by displacement of the B-site cation from its ideal crystallographic site and subsequent lengthening and shortening of B-O bonds in the octahedron. Symmetrically, this breaks all four-fold symmetry axes into lower symmetry axes and can result in various distortions of the octahedra. Given that there are two symmetrically distinct displacement types for the cation in an octahedron (displacement along a B-O bond, or axis of rotational symmetry, and displacements between bonds, or off-axis of rotational symmetry), second order Jahn-Teller distortions can also lead to tetragonality as seen in the example of ionic polarization in section 1.3.4, **Fig. 1.8**. Displacements leading to tetragonality are those along a bonding direction and distortions between bonding directions will lead to bending/rotational distortions.

While these distortions are generally resultant in perovskites of chemical variance in the B-site cation, they can also be induced through variance of the A-site cation. Furthermore, these distortions can help explain stable incorporation of cations with lone pairs (Pb^{2+}, Bi^{2+}) as the, non-symmetrical, excess electron density on the A-site can be mitigated through octahedral deformation or tilting. These distortions are also responsible for deviations in tolerance factors from unity, which are typified by tetragonal ($t > 1$), orthorhombic ($TF < 1$), and rhombohedral ($TF < 1$) phases. These phases are the most

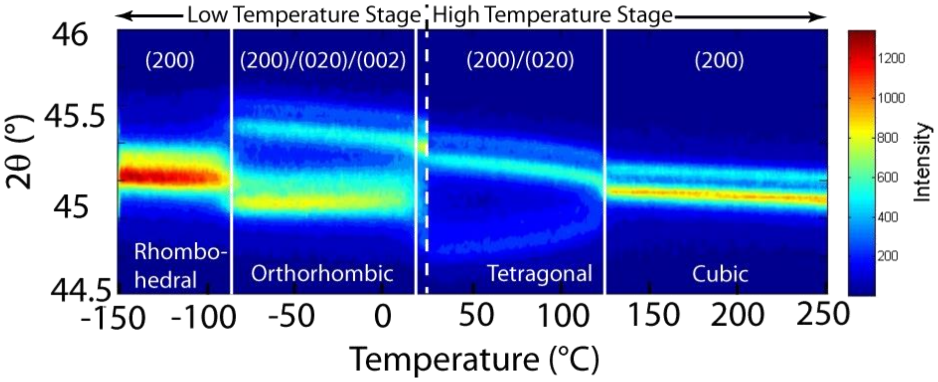

Figure 1.17: *In situ* powder X-ray diffraction data on $BaTiO_3$ showing the evolution of the {200} peak from a single peak at high temperature, cubic (a=b=c), to a split peak at 2:1 intensity, tetragonal (a=b≠c), to three distinct peaks, orthorhombic (a≠b≠c), back to a single peak, rhombohedral (a=b=c), at low temperature. Diffracted X-ray intensity is denoted by color, blue being low (background) intensity increasing to red (high) intensity. Extra intensities seen as peak ‘shadows’ (example of low intensity peak above main in cubic regime) are due to use of a non-filtered X-ray source. Data was collected by primary author using instruments at Analytical Instrumentation Facilities of North Carolina State University.

common phases seen in perovskite materials and are exemplified by lead titanate ($PbTiO_3$, tetragonal), calcium titanate ($CaTiO_3$, orthorhombic), low temperature barium titanate, (low-T $BaTiO_3$, rhombohedral), and strontium titanate ($SrTiO_3$, cubic.)

1.6.2 Phase Transitions and Permittivity

The phase of the perovskite materials above were only considered at a specific temperature. Each of these materials, however, exhibit two or more of the common phases between absolute zero and the materials melting point, with their highest temperature phase generally being cubic. This can be seen as represented by the $BaTiO_3$ system **Fig. 1.17**, which is rhombohedral at T < -90°C, orthorhombic between -90°C < T < 0°C, tetragonal between 0°C < T < 123°C [51], and finally cubic from 130°C to its melting point [52]. Each of these phase transitions are first-order phase transitions, where first-order phase transitions exhibit a discontinuity in the specific heat of the system at the transition temperature. That is the systems specific heat increases instantaneously, known as latent heat, as more thermal energy is put into the system. This is associated with an incorporation of thermal energy into the lattice necessary for it to rearrange and break symmetry. Second-order phase transitions are continuous transitions and do not incorporate latent heat into the system and is typified in this work by RFEs but is also observed in fine-grained $BaTiO_3$. Crystallographic phase transitions, as those described above in barium titanate, are always first-order phase transitions as they require lattice rearrangement. However, some of these first-order phase transitions can approach second-order behavior under stress or if their lattice enthalpies are very similar and only require slight distortions in transition. This can be observed through a broadening of the permittivity peak at the phase transition as opposed to a sharp delta peak.

As phase transitions require movement of charged species, it follows that any phase transition will contribute to dielectric displacement. This contribution to $\vec{\boldsymbol{D}}$ in perovskite phase transitions is seen as a gain to κ and is due to rearrangement of cations. In a PE – FE transition, not only is there a gain to κ from the rearrangement of cations but also from the instantaneous formation of polar domains, though this gain is only accessible in a small temperature window around T_c. Essentially, PE – FE phase transitions include both ionic contributions to permittivity (atomic displacements to distort crystal structure) and instantaneous dipolar contributions (formations of domains.) Above T_c, the ionic contributions diminish as ions stabilize in the new crystallographic phase, while dipolar contributions remain, though are dispersed through small randomly oriented domains. The result is that ferroelectric phases of materials generally exhibit higher permittivities than non-ferroelectric phases, especially around the transition temperature. However, as the very large gains are limited in temperature range, it is difficult to take advantage of this effect for high permittivity materials that operate over large temperature ranges.

It is possible to counteract this effect through engineering of the materials chemistry and incorporating chemical inhomogeneity into the material through solid solution. Such engineering can be of three approaches, shifting phase transitions closer in temperature space via varying stoichiometry, inducing second-order phase transition behavior into the material (relaxor behavior) through chemical disorder, or engineering composites of a single materials system of varied stoichiometry, where the material has stoichiometrically dependent phase transition temperatures (as is done in X7R barium titanate described earlier.)

1.6.2.1 Morphotropic Phase Transitions

One unconventional phenomenon resulting from shifting phase transitions closer in temperature space through compositional variance, and solid-state solution, is the morphotropic phase boundary (MPB). This effect is seen as a compositionally driven phase transition that is independent of temperature and occurs when the Gibbs free energy of one of the compositions phases is equivalent to another. Consequentially, various desirable effects are seen in MPB compositions as they exhibit co-existence of phases at a temperature. This allows for more available polarization directions with dramatic increases in materials properties (e.g. very large polarizations and enhanced electromechanical properties.) This effect is exemplified in lead zirconate titanate with a zirconium/titanium ratio of 52/48, $Pb(Zr_{0.52}Ti_{0.48})O_3$ (PZT 52/48), and this material is one of the most widely used electronic materials for ferroelectric and piezoelectric applications. A large experimental issue with the MPB effect is that these compositions are highly sensitive to stoichiometry and any changes in stoichiometry due to processing effects can cause deviations from the MPB composition. This generally results in materials that exhibit mixed-phase characteristics and, as the phases may not be exactly equivalent in free energy but close, can be hard to distinguish from actual MPB compositions.

Another, currently theorized, aspect of the MPB effect is that MPBs may be due to pressure effects, as an MPB was seen in pure $PbTiO_3$ under high pressure [53]. This work theorizes that it is an induced chemical pressure, due to differences in chemical potentials in the substituents of a solid solution, that gives rise to the MPB seen in PZT (52/48) and that all materials could exhibit such a pressure induced MPB. If correct, this theory could allow developing solid solutions with perovskite end members that would not generally form solutions such as non-ambient (refractory) materials that only exist at high pressure or high temperature.

1.6.3 Microstructure Effects

If we consider a materials unit cell (local) structure as its fundamental, primary, contributions to a material's dielectric properties, we see that various secondary effects arise from a materials microstructure. As a materials local structure is determined from the coherency in the periodic arrangement of unit cells, and gives rise to domains in FE materials, its microstructure is determined by the degree of coherency over larger scales. The regions in which domains share crystallographic symmetry are known as grains and are terminated by grain boundaries. Grains, also known as crystallites, can vary widely in size, ranging from nanometers in diameter to hundreds of centimeters. While the extremes of this range describe nanomaterials (grain size (t_g) < 100 nanometers) and single crystals of varied size (t_g > 1 mm), this work focuses on polycrystalline ceramics where grain sizes typically range on the micrometer scale. In ferroelectric polycrystalline materials, grain size has a very large effect on the overall properties of a material, especially its permittivity.

The effect grain size has on a FE material depends on the interplay between domain wall density and grain size. Given that the width of a domain wall ($t_{d.w.}$) is [6]:

$$t_{d.w.} = \sqrt{t_g}$$

It follows that, with decreasing t_g, the number of domains in the grain will also decrease by a squared root factor of t_g. This suggests that as t_g decreases, the domain density within that grain will increase, and therefore the grain will have inherently more unresolved stress. These increased stress states have been shown to inherently increase the permittivity of a material through the Devonshire phenomenological theory [22], [23]. However, as t_g continues to decrease (specifically $t_g < 1$ μm), the induced stress due to increased domain density becomes sufficient to mechanically suppress the FE phase in a material and therefore suppress polarization modes, essentially pushing the material back into a PE phase through stress induced pressure [54], [55]. This, in turn, will decrease the overall permittivity of the material. As a materials t_g is an effect of various variables in processing, as well as composition, determining parameters for ideal grain sizes to maximize permittivity is generally an issue for secondary process refinement and engineering. However, in any study of permittivity, microstructure should be considered and elucidated to determine any degree of permittivity contribution due to grain size.

1.7 Materials Systems and Applications

In today's world there exists a near infinite demand for development of advanced materials. This is owed to the intricately intertwined relationship between materials and technology. That is materials discovery drives new technologies, by example of the relatively recent discovery of quantum dots [56] and the development of ultra-high resolution 8K quantum dot supplemented light emitting diode (QLED) technologies by Samsung, and technology drives materials discovery, evidenced by the ever persisting, capitalistic, push for cost minimalization and increased output and/or efficiency through materials refinement or advancement. In fact, our civilizations and species have always existed in this manner, as the great periods of time of our existence, almost universally, become defined by the type of material leveraged by humankind at that time [57] (stone age, bronze age, iron age, coal/steel age, polymer age, silicon age, etc.) From everyday building materials, to sophisticated complex electronic devices, to advanced materials for extreme environments, if there exists an application, there exists a materials system, if not multiple, to fit its needs. This work will focus solely on dielectric materials systems for the applications of high temperature memory and actuators in ferroelectric and piezoelectric materials, and high permittivity dielectrics for advanced capacitor applications.

1.7.1 Dielectrics for High-Temperature Memory and Actuator Applications

The advancement of dielectric materials for high temperature applications depends on a variety of figures of merit. Specifically, for memory and actuator applications, these materials are ferroelectric, therefore exhibit a curie temperature, and are also piezoelectric. A main figure of merit for these materials is their T_c, as it defines the upper limit of the temperature range in which they are application viable. Other important figures of merit in these systems are their coercive field, E_c, remnant polarization, P_r, the piezoelectric coefficient, d_{33}, dielectric loss, $\tan\delta$, and dielectric constant, κ. In the world of high temperature materials there are two distinct regimes, lead-based materials, and lead-free materials. To this regard, the focus of this work will be lead-based materials, however the study of lead-free materials for normal and high-temperature materials has led to discovery of various different materials systems that will be discussed for high-permittivity applications, and therefore they shall be discussed briefly as well.

1.7.1.1 Lead-Based Materials

Lead based materials generally exhibit very desirable ferroelectric and piezoelectric properties owing to the inherent qualities of lead cations (Pb^{2+}) in perovskite solid solutions. Lead (II) is not only a very large, polarizable, cation, its electron configuration of $[Xe]6s^2(4f^{14}5d^{10})6p^0$ gives rise to a stable lone pair of electrons. This lone pair effect contributes to its electrostatic polarizability, as well as the polarizability of the overall unit cell. This is realized through an incorporation of excess electron density onto the perovskite A-site which must be accounted for through octahedral distortion. This can easily be observed in the $PbTiO_3$ materials system, where the size of Pb^{2+} and its lone pair effect give rise a very stable tetragonal phase at standard temperature and pressure (STP) which persists to high temperature, exhibiting a T_c at 495°C. While $PbTiO_3$ itself is not a desirable material for ferroelectric and piezoelectric properties due to high dielectric losses and low electromechanical coupling factors [58] its high T_c and ability to readily form solid-solutions make it the starting point for many research endeavors into high T_c ferroelectric materials systems. In fact, no materials system is more ubiquitous in the realm of piezoelectric and ferroelectric materials than lead zirconate titanate (PZT), $Pb(Zr,Ti)O_3$, the binary solid solution of $PbTiO_3$ and $PbZrO_3$ [52], [59], [60]. Lead zirconate titanate owes its ubiquity to its exhibition of an MPB at the zirconium/titanium ratio of 52/48. This MPB composition is responsible for very desirable materials properties (namely exhibiting excellent piezoelectric properties,) as well as a very tunable materials system.

1.7.1.2 Lead-Free Materials

While PZT and lead-based materials currently demonstrate the most advantageous materials properties for ferroelectric and piezoelectric applications, the known high toxicity levels of metallic Pb (and Pb containing compounds) necessitate questions of toxicity in lead-based perovskite materials. Insofar as legislative bodies around the world have limited, or even banned through regulation, the extent of lead content in materials and complex devices. Passing of original legislation to this effect in the European Union and United States around the early 2000's preempted a boom of research into lead-free materials of comparable or equal quality to that of PZT. This led to research trying to mimic the MPB found in PZT in well-known barium titanate systems, as well as incorporation of the lone pair effect from Pb^{2+} through use of similar elements whose ionic state contains a lone pair such as tin (Sn^{2+}) and bismuth (Bi^{3+}). While this research is still ongoing and has yet to produce a single system to rival PZT, it has produced various systems of comparable properties such as the solid solution of sodium bismuth titanate and barium titanate (NBiT-BT) [61], potassium sodium niobate (KNN) [62], [63], and barium calcium zirconate titanate (BCZT) [64]. A comparison of the inverse piezoelectric coefficients of these materials systems and PZT can be seen in **Fig. 1.18** [65]. Another important consequence of these lead-free systems was the discovery of relatively high permittivity materials with phase transitions near, or around, room temperature, namely that seen in the BCZT system.

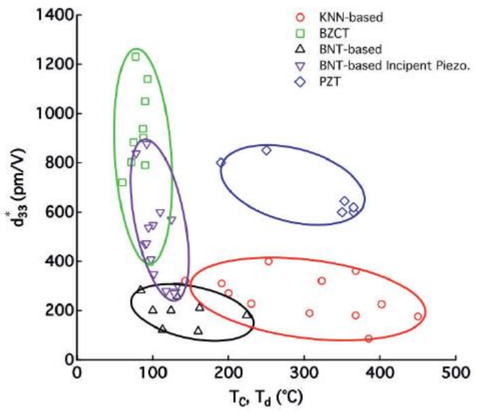

Figure 1.18: Inverse piezoelectric coefficient (d_{33}^{*}) of various lead-free based solid solutions as compared to Pb(Zr_xTi_{1-x})O_3. Figure adopted from Rodel et al. [65]

1.7.2 High Permittivity Dielectrics for Multilayer Ceramic Capacitors

As discussed earlier, the main characteristics that define a dielectric material for capacitor applications are its dielectric constant, κ, dielectric loss, *tan d*, temperature dependence (to be defined qualitatively for this review), and voltage dependence. Other important characteristics are the materials insulation resistance and piezoelectric coefficient (low to avoid delamination within the capacitor,) however these are secondary in concern as the material cannot perform well within a capacitor if the first four properties are not within desirable ranges. The epitome of a high permittivity dielectric material for MLCC applications would be one with a very high dielectric constant > 20,000, very low dielectric loss < 0.01, little to no temperature dependence over the desired temperature range (defined by **Table 1.1** section 1.1.2,) and zero voltage dependence. As capacitors function normally at or around room temperature, this review will focus on materials systems in literature with reported instances of high permittivity near room temperature. For each material system reported, there will be brief discussion on quality of the observed permittivity, the compositional variance of the system, its permittivity, and any trends therein, the proposed mechanisms underpinning its dielectric response, and a brief discussion on candidacy for further research into the system for MLCC applications.

1.7.2.1 $BaTiO_3$ Based High-κ Systems

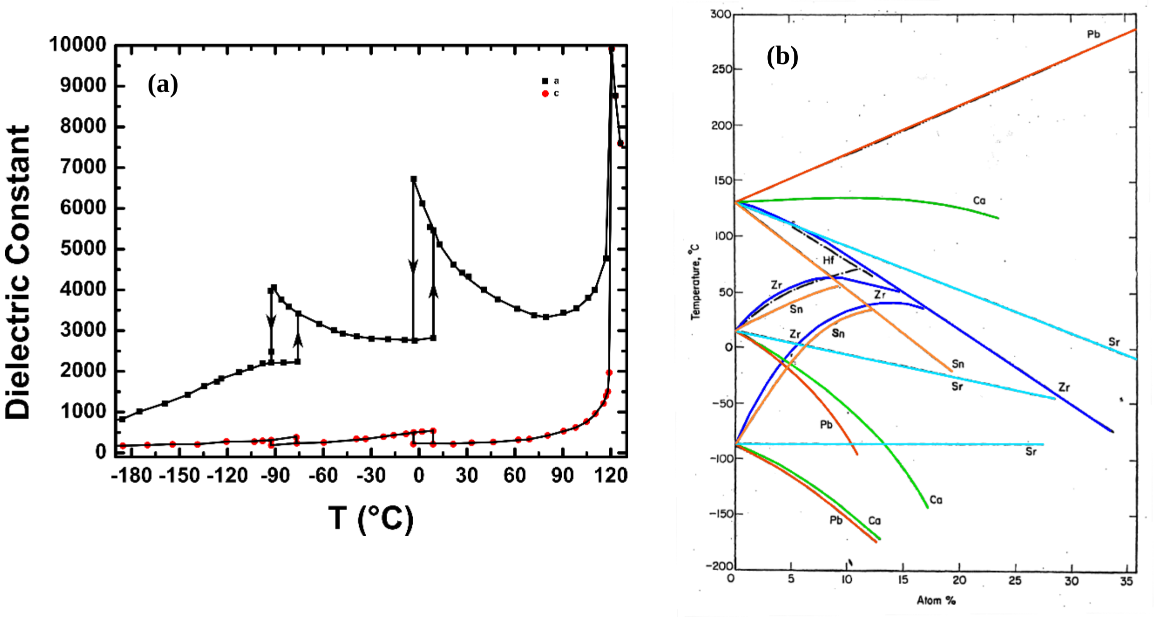

Figure 1.19 (a) dielectric permittivity versus temperature for single crystal $BaTiO_3$ as digitized from Jaffe *Piezoelectrics* [51] and (b) effect of A-site or B-site cation doping on phase transition temperatures in $BaTiO_3$ as adopted from Herbert and Moulson [6]

As previously discussed, barium titanate (BT) is the primary material used in MLCC applications. With it being a well-known ferroelectric system, ahe push for lead-free materials generating various solid solutions based on BT, it becomes a natural starting place for research into high permittivity materials for MLCCs. Barium titanate itself exhibits various ferroelectric phases between its PE-FE phase transition (~130°C) as discussed section 1.6.2 and seen in **Fig. 1.17**, which exhibit, relatively, high permittivities (on a historical scope) as seen in **Fig. 1.19 (a)**. One important aspect of these phase transitions is their ability to be influenced through cation doping of the A-site or B-site in

BT. As seen in **Fig. 1.19 (b)**, different stoichiometric additions of doping cations to BT can increase, or decrease, the temperature at which a phase transition occurs. For example, 5% doping of Zr $^{4+}$ on the B-site will increase the rhombohedral – orthorhombic phase transition by ~50°C, increase the orthorhombic – tetragonal transition by ~50°C and decrease the tetragonal – cubic transition by ~10°C. As the materials permittivity can be maximized through mixed-phase stability regimes, the ability to shift phase transitions through cation doping to a common temperature is a plausible route to maximizing permittivity in BT.

A note on the following subsections and terminology. As to the terminology of doping and solid-state solutions, as these two terms can commonly be used interchangeably, it is important they are well defined. In this work, doping will refer to small additions to a solid solution of a single cation > 3 mol%. Doping can be done stoichiometrically (leading to a solid solution and the inherent confusion) or non-stoichiometrically (leading to incorporation of dopant on defect sites within the material.) Furthermore, in any materials system researched for high permittivity, it is commonplace to dope a system with small amounts of a rare earth metal or lanthanide/actinide to increase overall permittivity through Z_{eff}.

1.7.2.1.1 (Ba,Ca)(Zr,Ti)O_3

Ba,Ca(Zr,Ti)O_3 was discovered in 1954 by McQuarrie *et al.*, [66] for potential capacitor applications. However, the system did not receive much attention until the late 90's and early 2000's when lead-free piezoelectric materials became desirable. It was then that the BCZT system was found to exhibit compositions with piezoelectric coefficients comparable to that of PZT (d_{33} BCZT ~ 620 pC/N) [67]. While a large amount of research into this pseudo-quaternary system for piezoelectric applications has occurred [64], [67]–[71] since then, the work presented in this dissertation focuses solely on the systems observed, compositionally dependent, high permittivity (ε_r ~ 10,000) at or around room temperature. Throughout this body of work, the relatively high permittivity has been continually observed, namely by [64], [65], [70], however (as the goal of this work is to develop materials for MLCC applications,) the large piezoelectric coefficients are not desirable. Despite this inherent issue, the BCZT material system is suggested to be a possible candidate material system for research, with the hypothesis of: if a relaxor ferroelectric phase can be induced through small phase fraction incorporation of chemically dissimilar cations, then the Curie temperature response of the parent BCZT solid solution will become diffusely distributed, maintaining the desirable high permittivity phase over a large temperature window. In addition, the possibility exists that, if the large apparent strains are dependent mainly on domain wall motion, the breaking of domain wall formation due to the induced RFE could inhibit the piezoelectric effect in these materials.

Barium calcium zirconium titanate is a pseudo-quaternary solid solution of $BaTiO_3$ (BT), $CaTiO_3$ (CT), $CaZrO_3$ (CZ), and $BaZrO_3$ (BZ). To simplify, and better represent the physical reality of the solid solution, CZ will not be considered. As any composition in this phase space can be defined by A-site (Ba/Ca) ratio and B-site (Ti/Zr) ratio, the removal of CZ has no mathematical ramifications. This system is also commonly defined in literature as a binary of $Ba(Zr_{1/2}Ti_{1/2})O_3$ (BZT) and $(Ba_{1/2}Ca_{1/2})TiO_3$ (BCT). While the literature varies on style of reporting $(Ba,Ca)(Zr,Ti)O_3$ compositions, the ternary definition of BT-BZ-CT will be used in this review. Studies into this system mostly focus on the $BaTiO_3$

rich side of the ternary, from 65% - 85% BT [67] or fixed percentages of BT, generally 50% with varying CT/BZ phase fractions.

Synthesis of BCZT ceramics generally follows nominal solid-state solution processing, though some studies have shown processing methods can play a critical role on resultant properties. Studies done by Bai et al. [64] show a dependency between the sintering temperature and resultant grain sizes for compositions of 50% BT with varying BZ/CT. That is, lowering the sintering temperature (1450°C – 1475°C) would result in more desirable densities and average grain sizes. Furthermore, processing studies have shown that the use of sintering aides (non-stoichiometric additions) can improve processing for BCZT. Namely, the addition 0.5mol% CuO resulted in improved densities from 94% to 98% for undoped samples sintered at 1450°C versus doped samples sintered at 1325°C [68]. It has also been seen that Ti deficiencies in BCZT can lead to stabilization of the tetragonal phase [72], and that the microstructure is also dependent on oxygen partial pressure during sintering [73] It is notable that these studies were done on samples processed using the sol-gel method.

These studies have shown BCZT to have an intricate phase diagram. The sintering studies done by Bai et al. show a stable tetragonal phase for fixed 50% BT with increasing CT phase fractions (greater that CT/BZ of 50/50) at room temperature, with the 50/50 sample exhibiting a phase mixture of orthorhombic and tetragonal. Compositions of higher BZ phase fraction exhibit a rhombohedral phase. This is consistent with the doping scheme seen in **Fig 1.18**, where increasing phase fractions of Ca into BT disproportionately destabilizes the orthorhombic and rhombohedral phases in respect to the destabilization of the tetragonal phase. Further studies into BCZT with fixed BT or fixed CT done by Chaiyo et al. [67], [70] show that increasing phase fractions of BZ induce a tetragonal to cubic phase transition from low BZ content to high BZ content at a CT/BZ ratio of 0.10/0.15. It should also be noted that, from observed XRD patterns in Chaiyo's work the degree of tetragonality decreases substantially as that ratio is approached. The apparent consequence of these studies is that the BCZT solid solution presents a compositionally tunable triple point where the FE phases at the FE-PE phase transition (orthorhombic, rhombohedral, and tetragonal) are of equivalent free energy and therefore equiprobable to exist and, that, at this triple point, the dielectric properties of the solid solution are maximized.

Table 1.2

Compilation of dielectric properties of BCZT solid solutions at T_c or T_{max} as a function of composition from the work of Chaiyo et al.

% BT	% BZ	% CT	T_c (°C)	ε_r @ T_c	tan δ	ref
82.5	2.5	15	100	~9000	0.02	[70]
77.5	7.5	15	75	~10,000	0.02	[70]
72.5	12.5	15	30	~10,500	0.025	[70]
75	0	25	100	~5,500	0.015	[67]
75	5	20	80	~6,250	0.02	[67]
75	10	15	60	~10,000	0.02	[67]
75	15	10	45	~11,500	0.025	[67]
75	20	5	10*	~9,000	0.03	[67]
75	25	0	-20*	~9,000	0.0175	[67]

* samples that exhibit relaxor ferroelectricity and therefore value reported refers to T_{max}, as opposed to T_c

The dielectric properties of the BCZT system are best summarized by the work of chaiyo [both refs] and are summarized in **Table 1.2**. Note that the T_c reported in **Table 1.2** is not a true Curie temperature for all samples, as relaxor behavior onset with increasing phase fractions of BZ, as noted by an asterisk in the table. Notably, there are various compositions of note for candidacy, with most compositions exhibiting relative permittivities higher than 9000 with correlated low dielectric loss ≤ 0.03 at the maximum temperature, all within the desired temperature range for X(5-7) capacitors (from **Table 1.1**). Also of note is the trend of increasing maximum permittivity with increasing phase fraction of BZ, and lower fractions of CT, where the permittivity maximizes at a Ca/Zr ratio of 1.5/1.

Overall, the BCZT solid solution presents a very desirable candidate system for development of a high permittivity relaxor ferroelectric material for MLCC applications. This is due to its compositionally dependent, high permittivity, FE-PE phase transitions within the desired temperature range for MLCC materials. While it is recognized that challenges due to the high piezoelectricity of the parent BCZT solid solution may exist for any developed material, these concerns are secondary and could be mitigated with further research and device engineering if, indeed, a desirable material is developed.

1.7.2.1.2 Cerium doping in $BaTiO_3$

Various literature reports over the past two decades have shown that cerium doping in barium titanate is a possible candidate to develop high permittivity relaxor ferroelectric materials. However, this system is innately complex as cerium can be incorporated into BT solid solutions on both the perovskite A and B-site given its electronic configuration [Xe] $4f^1$ $4d^1$ $6s^2$, and ionic radii for Ce(II) and Ce(IV) being comparable to Ba(II) and Ti(IV). Generally, the oxidation state for Ce in these solid solutions are fixed stoichiometrically in batching, however any slight off-stoichiometries that can arise during processing can lead to multivalency in Ce and partial doping of both A and B sites in the perovskite. Therefore, careful attention to the processing of these ceramics is very important. And, as it is well known that oxygen partial pressure is needed in the processing of stoichiometric $BaTiO_3$

to prevent reduction of Ti^{4+} to Ti^{3+} [74], it is feasible that some Ce multivalency would be inherent to all Ce-doped BT materials. Studies into this system generally focus on B-site Ce doping with additions of up to 50% Ce on the B-site done by *Chen et al.* [75], and up to 30% done by *Canu et al.* [76] and *Hwang et al.* [77]. Notably, the study done by *Hwang et al.* simultaneously focused on A-site doping of Ce with additions of Ce between 30% and 100%.

Samples reported in these literature reports were synthesized by normal solid solution processing routes. Samples of raw precursors were mixed stoichiometrically, wet milled, pressed isostatically, and thermally treated in air with calcining temperatures around 1350°C and sintering temperatures averaging at 1550°C. Notably, A-site doped samples were sintered at 1350°C in air for 5 hours. Literature is scant on processing studies, however one notable study [78] found that the material permittivity was critically dependent on Ce particle size, with lower particle sizes deteriorating ferroelectric properties, and therefore the observed permittivities. Structural studies show the normal room temperature orthorhombic $BaTiO_3$ progressively averaging into a pseudo-cubic phase with increasing fractions of Ce. In general, the structure typically transformed fully into the pseudo-cubic phase by ~3 mol% Ce [77].

Dielectric properties for these Ce-doped BT samples are compiled and summarized in **Table 1.3**. First observations show very high permittivities at T_{max} ($\varepsilon_{r,Tmax}$ > 10,000) with maximum temperatures in the desired temperature for MLCC applications. Notably, however, there are some observable inconsistencies between studies, with large variations between measured permittivities at specific compositions. Namely, between all three studies referenced, measured permittivities for BT doped with 10 mol% C e on the B-site

Table 1.3

Compilation of dielectric properties of Ce doped $BaTiO_3$ solid solutions at T_{max} as a function of composition for both A-site and B-site substituted Ce

% Ba	% Ti	% Ce	T_{max} (°C)	ε_r @ T_{max}	tan δ @ T_{max}	ref
100	100	0	140	8,000	--	[77]
100	98	2	127	7,500	--	[74]
100	95	5	122	10,000	--	[74]
100	95	5	140	9,000	--	[77]
100	90	10	109	13,000	--	[74]
100	90	10	140	8,750	--	[77]
100	90	10	77	6,500	0.04	[75]
100	88	12	90	10,000	--	[74]
100	85	15	62	10,500	--	[74]
100	82.5	17.5	27	9,500	--	[74]
100	80	20	2	8,000	--	[74]
100	80	20	30	3,900	0.02	[75]
100	70	30	140	8,000	--	[77]
100	70	30	-76	1,200	0.03	[75]
100	67	33	-73	800	0.03	[75]
100	60	40	-90	500	0.03	[75]
100	50	50	-90	300	0.03	[75]
70	100	30	75	8,500	--	[77]
50	100	50	30	15,000	--	[77]
30	100	70	-15	20,000	--	[77]
0	100	100	-20	16,000	--	[77]

ranged from a minimum of ~6,500 to a maximum of ~13,000. However, the trend in decreasing maximum permittivities with increasing content of Ce holds across all studies, with exception of the work of *Hwang et al.* [77] which showed an increase in the permittivity at small fractions of Ce up to 5 mol% Ce, with the decrease in the maximum permittivity beginning at 10 mol%. Other notable discrepancies are a lack of reported dielectric loss in [77],[74] and variation in T_{max} for equivalent compositions across studies. These discrepancies could be attributed to the observed dependency on particulate size in Ce [78] and the use of Ce precursors from various sources. This is highly likely as additions of Ce > 3 mol% led to the onset of RFE characteristics observable in the dielectric response. As the T_{max} in RFE systems is highly dependent on the size distribution of PNRs (as discussed in section 1.4.3), which likely depend on initial particle sizes in the system, it is likely that this would lead to the observed discrepancies in T_{max} across studies.

Contrastingly, A-site doping of Ce shows much higher permittivity values (15,000 to 20,000) which increase with increasing phase fractions of Ce, the highest observable permittivity of 20,000 at 70 mol% Ce, and lower maximum temperatures which decrease with increasing Ce content. However, the maximum permittivity decreases again between 70 and 100 mol% Ce. It, therefore, may be more beneficial to pursue A-site doping of Ce for high permittivity applications, however the report lacks data on the dielectric loss which might suggest the possibility of inherent space charge mechanisms. It should also be noted that, as all samples in these studies were processed in air, it is probable that they all contain some degree of aliovalent Ce.

Overall, this system presents a promising candidate for further study. As the addition of Ce to BT already induces RFE character in compositions with as low as 3 mol% Ce, it lends itself well to the proposed hypothesis for generating desirable high permittivity RFE materials. This system also provides for various routes to develop these materials, focusing either on low mol% B-site doping, high mol% A-site doping, or studies into engineered aliovalent A-site and B-site doping.

1.7.2.2 Co-doping Systems

Co-doping, as applied to perovskites, is the doping of a specific lattice site (namely the B-site) with aliovalent cations. In general, the site occupancy of the nominal stoichiometry material is reduced by a fraction, x, and is replaced by a 1:1 ratio of two various cations with different formal charge, ensuring that the resultant solid solution is charge neutral. For instance, in a A(II)B(IV)O_3 perovskite, the B^{4+} cation is reduced by x% and doped by x/2% $B^{`}$(III) + x/2% $B^{``}$(V). In general, this doping scheme is reported as x% ($B^{`}$ + $B^{``}$), and can vary in valence state so long as the overall charge balance on the B-site is charge neutral, i.e. x% ($B^{`}$(II) + $B^{``}$(VI)) while physically improbable is a possible combination. Some work has focused on applying this scheme to $BaTiO_3$ based solid solutions [79]–[81], however the most notable recent work was that on co-doping in TiO_2 published in *Nature* [82].

1.7.2.2.1 Co-doped TiO_2

Co-doping in TiO_2 using Nb^{5+} and In^{3+} is examined at depth in the work done by *Hu et al.* [82]. This work focuses on four different levels of Nb+In co-doping, 0.05%, 0.5%, 5%, and 10% as well as asserts some preliminary studies on the use of varied 3^{+} cations in the co-doping scheme such as Al^{3+} and Ga^{3+}. These samples were synthesized via normal solid-state methods, except for the lack of a calcination step, where homogenously mixed precursor oxides were annealed at 1400°C/10h with 2°C/min ramp rates. Notably, rutile-type TiO_2 was used in these experiments owing to it exhibiting the largest permittivity of TiO_2 allotropes.

The dielectric properties of these co-doped TiO_2 compositions are summarized in **Figure 1.20** as taken from *Hu et al*. In **Figure 1.20a** it be seen that the permittivity response maintains a very high (termed ‘colossal’) permittivity that increases with % co-doping

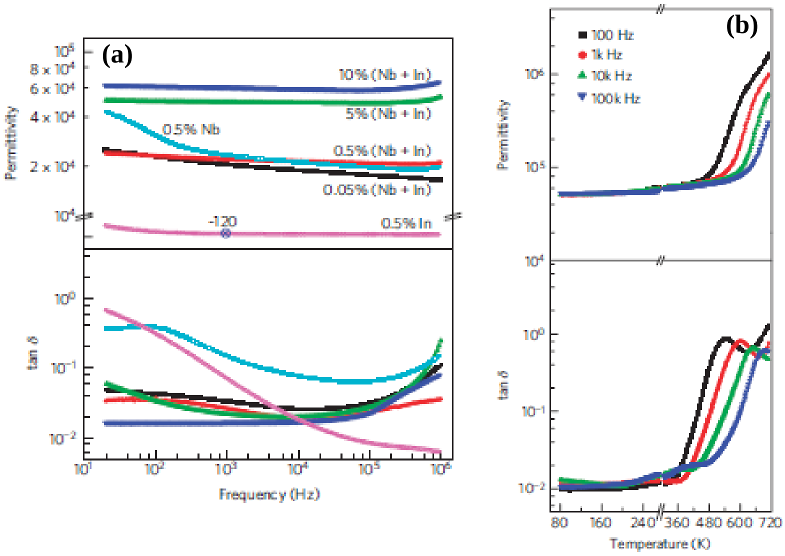

Figure 1.20: Dielectric properties as (a) a function of frequency for co-doped TiO$_2$ with x% (Nb+In) and (b) as a function of temperature for 10% (Nb+In) co-doped TiO$_2$ as reported by Hu et al. in *Nature* [82]

constituents and is mostly independent of frequency at room temperature. In **Figure 1.20b** the permittivity response for 10% (Nb+In) co-doped TiO$_2$ is essentially flat for the desired working temperature range, correlated with low dielectric loss, for most MLCC applications. These permittivity values range from ε_r ~ 20,000 for 0.05% co-doping of Nb + In, to ε_r ~ 60,000 for 10% co-doping of Nb + In at room temperature, with the 10% co-doping composition ranging from ε_r ~ 55,000 at T = -55°C to ε_r ~ 62,000 at T = 85°C.

If the entirety of these permittivity values can be realized for capacitor applications, these materials could be very desirable for use in MLCC devices. However, proposed mechanisms for the described 'colossal' permittivity (K~60,000 in 10% (Nb + In) co-doped TiO$_2$ vs. K~250 in stoichiometric rutile TiO$_2$) of stabilized electron pinned defect structures arising from the co-doping scheme, suggest that the very large gain to the permittivity may be partly, or largely, due to space charge or Maxwell-Wagner type polarization mechanism. If so, the permittivity of these materials would be voltage dependent, and result in large conduction values under application of relatively low fields (~ 1kV/cm). However, the near perfect dielectric response of high permittivity, temperature stable materials for MLCC applications necessitates further study into this system to determine the extent of utilizable permittivity of the observed ‘colossal’ permittivity response.

1.7.2.3 Ba(Fe,Nb)O_3

While most perovskites under consideration for study into advanced dielectric materials are titanium based (or on an A(II)B(IV)O_3 formal charge distributions), A(I)B(V)O_3 type perovskites are also prevalent in this field of study. Namely, many niobium-based perovskites have been researched and shown to exhibit a wide array of properties for both A(I)NbO_3 and A(II)(B`(II/III)Nb)O_3 typic perovskites.

In the aftermath of the discovery of ‘colossal’ permittivities in $CaCu_3Ti_4O_{12}$ at DuPont as reported by *Subramanian et al.* [83] a large volume of research was dedicated to the discovery of ‘giant’ permittivities observed in iron containing perovskites of the type $A(Fe_{1/2}B_{1/2})O_3$. This body of work is summarized in [84]–[91] and generally focuses on, or around, the processing effects of stoichiometric BFN with Fe:Nb ratio of 1:1. Lacking in the body of work is any study into BFN solid solutions of Fe:Nb ratio of 1:2 as a charge balanced perovskite can be formed at this ratio given the multivalency of Fe, $Ba(Fe^{2+}_{1/3}Nb^{5+}_{2/3})O_3$. Also, given the aliovalent nature of Fe (its tendency to exist in solid solution in both Fe(II) and Fe(III) simultaneously), it is possible that this system could exhibit various stable perovskites with mixed Fe valency as the B-site must have a formal charge of +4, and the equation:

$$2X_{Fe(II)} + 3X_{Fe(III)} + 5X_{Nb(V)} = 4$$

defines a truncated plane of real numbers (when considered for absolute values), any point on which could correspond to a stable BFN perovskite with incorporated Fe(II/III) aliovalency. While no studies were found by this work into these hypothetical compositions, they could be promising for future studies into both high permittivity materials as well as multiferroic perovskites. One of the biggest challenges will be controlling the oxidation state of the Fe ion and the resultant stoichiometry of the perovskite phase throughout the temperature ranges experienced during processing.

Of further note, a handful of studies into the BFN 1:1 material explored modifications to the BFN solid solution through doping and varying processing methods. These included the doping of Ti(IV) on the B-site up to 5% Ti [88], La(II) doping on the A-site up to 20% La [84], and mechanochemical synthesis of BFN [90], [91].

Samples of BFN were synthesized via normal solid-state methods with calcining and sintering done in air at temperatures ranging from 950°C – 1250°C, and 1200°C – 1550°C, respectively. Dwell times for both calcining and sintering steps averaged around 4 hours in all studies. Notably, powders and pellets were processed in either Pt crucibles or Pt-foil lined crucibles in all studies, most likely to prevent crucible reaction with the sample. Mechanochemically synthesized samples were processed with an initial wet mill to homogenize, and subsequent high-energy ball milling with times varied between 1-75 h [90] and 25-100h [91]. Mechanically reacted powders in [90] were immediately processed into dense ceramics, did not contain a calcination step, whereas those fabricated in [91] maintained a calcination step at 1250°C/4h prior to sintering at 1350°C/4h. Structures of synthesized BFN ceramics were found to be metrically cubic via XRD with no effect to

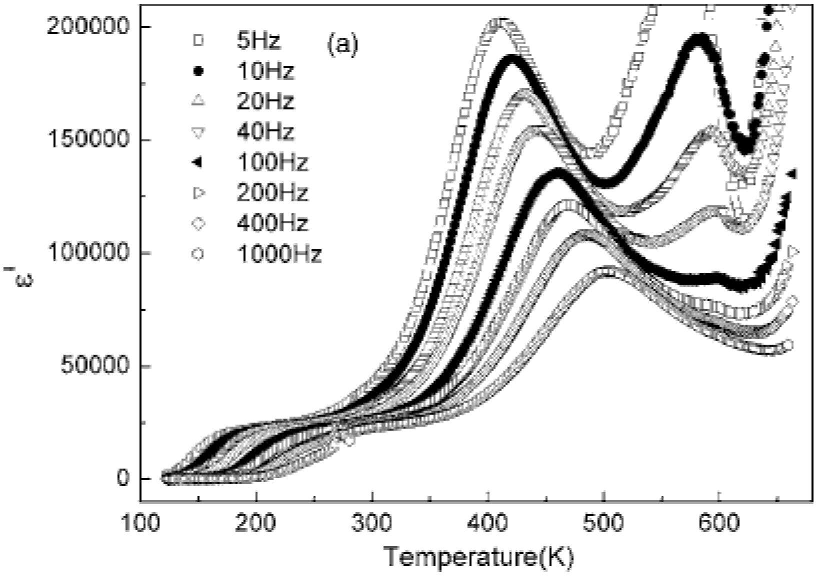

Figure 1.21: Dielectric permittivity as a function of temperature for BFN as reported by Wang et al. in *Applied Physics Letters*

the bulk structure through A-site or B-site doping or mechanochemically synthesis, however conflicting data exists in the La-doped study suggesting the un-modified BFN and subsequent La-modified compositions to be monoclinic through least-squares refinement. However, no description as to the type of refinements utilized requires further research for the structure to be elucidated substantially.

The observed dielectric phenomena for these samples varies widely on a study-to-study basis, however all studies report very high permittivity values from ε_r ~ 12,000 to upwards of 200,000 [85] at ε_{max}. While these very large and desirable permittivity values were generally associated with low dielectric loss values, *tan d* ~ 0.2, various studies did not report any loss values. In almost all studies, the permittivity peak was highly diffuse and frequency dependent as is typified in **Figure 1.21**. Here, multiple peaks in the permittivity are observed with a characteristic frequency dependence persisting throughout the entire temperature range. This is consistent with the observed cubic structure in these materials, as this frequency dependence is most likely not due to a relaxor ferroelectric phase, but due to point defects and/or defect structures within the material. Therefore, it is very likely that the observed 'colossal' permittivities are due to Maxwell-Wagner-like mechanisms arising from polar defects and space charge with various activation/relaxation constants. However, due to desirability of the observed permittivity responses, studies into this material, and the underlying mechanisms giving rise to its permittivity, are warranted to explore the potential for MLCC applications.

1.8 References

[1] J. Ho, T. R. Jow, and S. Boggs, "Historical introduction to capacitor technology," *IEEE Electr. Insul. Mag.*, vol. 26, no. 1, pp. 20–25, Jan. 2010.

[2] B. Park, *A History of Electricity: (The Intellectual Rise in Electricity) from Antiquity to the Days of Benjamin Franklin*. J. Wiley & Sons, 1895.

[3] Z. D. Boren, "There are officially more mobile devices than people in the world | The Independent | The Independent," *Independent*, 2014. [Online]. Available: https://www.independent.co.uk/life-style/gadgets-and-tech/news/there-are-officially-more-mobile-devices-people-world-9780518.html. [Accessed: 08-Dec-2020].

[4] Y. Honda, *AEI*, p. 48, Oct-2004.

[5] C. Hendricks, Y. Min, and V. Magadala, "What is happening to the long term life of MLCCs," in *CARTS*, 2010, pp. 3–11.

[6] A. J. Moulson and J. M. Herbert, *Electroceramics*. Chichester: John Wiley & Sons, Ltd, 2003.

[7] M. Fortunato, "Temperature and Voltage Variation Ceramic Capacitor | Maxim

Integrated," *Maxim Integrated*, 2012. [Online]. Available: https://www.maximintegrated.com/en/design/technical-documents/tutorials/5/5527.html. [Accessed: 08-Dec-2020].

[8] J. C. Maxwell, "A Treatise on Electricity and Magnetism," *Nature*, vol. 7, no. 182, pp. 478–480, Apr. 1873.

[9] K. W. Wagner, "Zur Theorie der unvollkommenen Dielektrika," *Ann. Phys.*, vol. 345, no. 5, pp. 817–855, Jan. 1913.

[10] Q. Tan, P. Irwin, Non-Member, and Y. Cao, "Advanced Dielectrics for Capacitors Non-member."

[11] J. C. Manley, "Encapsulated electrical capacitor," US3496435A, 09-Dec-1968.

[12] R. G. Capek and J. P. Mazintas, "Method of making multilayer ceramic capacitors," US3549415A, 15-Jul-1968.

[13] T. I. Prokopowicz, "High voltage ceramic capacitor," US3496434A, 22-Nov-1968.

[14] F. Kossar, "Method of making multilayer circuit system," US3545079A, 02-May-1968.

[15] A. R. Rodriguez and C. John, "Process for manufacturing multilayer ceramic capacitors," UA3235939, 06-Sep-1962.

[16] X. Zhao, B. M. Sánchez, P. J. Dobson, and P. S. Grant, "The role of nanomaterials in redox-based supercapacitors for next generation energy storage devices," *Nanoscale*, vol. 3, no. 3, p. 839, Mar. 2011.

[17] T. Hans and D. James, "Insulating material," US2429588A, 02-Oct-1941.

[18] C. A. Randall, R. E. Newnham, and L. E. Cross, "History of the First Ferroelectric Oxide, $BaTiO_3$."

[19] O. Saburi, “Properties of Semiconductive Barium Titanates,” *J. Phys. Soc. Japan*, vol. 14, no. 9, pp. 1159–1174, Sep. 1959.

[20] P. W. Forsbergh, “Domain Structures and Phase Transitions in Barium Titanate,” *Phys. Rev.*, vol. 76, no. 8, pp. 1187–1201, Oct. 1949.

[21] J. P. Remeika, “A Method for Growing Barium Titanate Single Crystals,” vol. 76, pp. 940–941, 1953.

[22] A. F. Devonshire, “XCVI. Theory of barium titanate,” *London, Edinburgh, Dublin Philos. Mag. J. Sci.*, vol. 40, no. 309, pp. 1040–1063, Oct. 1949.

[23] A. F. Devonshire, “CIX. Theory of barium titanate— *Part II*,” *London, Edinburgh, Dublin Philos. Mag. J. Sci.*, vol. 42, no. 333, pp. 1065–1079, Oct. 1951.

[24] J. T. Last, “Infrared-Absorption Studies on Barium Titanate and Related Materials,” *Phys. Rev.*, vol. 105, no. 6, pp. 1740–1750, Mar. 1957.

[25] E. C. Subbarao, M. C. McQuarrie, and W. R. Buessem, “Domain Effects in Polycrystalline Barium Titanate,” *J. Appl. Phys.*, vol. 28, no. 10, pp. 1194–1200, Oct. 1957.

[26] R. D. Burbank, H. T. Evans, and IUCr, “The crystal structure of hexagonal barium titanate,” *Acta Crystallogr.*, vol. 1, no. 6, pp. 330–336, Dec. 1948.

[27] A. G. Chynoweth, “Surface Space-Charge Layers in Barium Titanate,” *Phys. Rev.*, vol. 102, no. 3, pp. 705–714, May 1956.

[28] N. Blattau, D. Barker, and C. Hillman, “Lead Free Solder and Flex Cracking Failures in Ceramic Capactiors,” in *CARTS*, 2004.

[29] Bruchhaus, “US PATENT 6109191.”

[30] P. Lunkenheimer, V. Bobnar, A. V Pronin, A. I. Ritus, A. A. Volkov, and A.

Loidl, “Origin of apparent colossal dielectric constants.”

[31] J. F. Scott, A. Schilling, S. E. Rowley, and J. M. Gregg, “Some current problems in perovskite nano-ferroelectrics and multiferroics: kinetically-limited systems of finite lateral size,” *Sci. Technol. Adv. Mater.*, vol. 16, no. 3, p. 036001, Jun. 2015.

[32] P. Curie, “Sur la symétrie dans les phénomènes physiques, symétrie d’un champ électrique et d’un champ magnétique,” *J. Phys. Théorique Appliquée*, vol. 3, no. 1, pp. 393–415, 1894.

[33] A. A. Bokov and Z.-G. Ye, “Recent progress in relaxor ferroelectrics with perovskite structure,” *J. Mater. Sci.*, vol. 41, no. 1, pp. 31–52, Jan. 2006.

[34] G. Burns, F. H. Dacol, G. Burns, and F. H. Dacol, “Glassy polarization behavior in ferroelectric compounds and,” *Solid State Commun.*, vol. 48, no. 10, pp. 853–856, Dec. 1983.

[35] A. Naberezhnov, S. Vakhrushev, B. Dorner, D. Strauch, and H. Moudden, “Inelastic neutron scattering study of the relaxor ferroelectric PbMg Nb O at high temperatures,” *Eur. Phys. J. B*, vol. 11, no. 1, pp. 13–20, Sep. 1999.

[36] V. V. Shvartsman, W. Kleemann, T. Łukasiewicz, and J. Dec, “Nanopolar structure in Sr x Ba 1 − x Nb 2 O 6 single crystals tuned by Sr ∕ Ba ratio and investigated by piezoelectric force microscopy,” *Phys. Rev. B*, vol. 77, no. 5, p. 054105, Feb. 2008.

[37] S. Vakhrushev, A. Nabereznov, S. K. Sinha, Y. P. Feng, and T. Egami, “Synchrotron X-ray scattering study of lead magnoniobate relaxor ferroelectric crystals,” *J. Phys. Chem. Solids*, vol. 57, no. 10, pp. 1517–1523, Oct. 1996.

[38] W. Ge *et al.*, “Direct evidence of correlations between relaxor behavior and polar

nano-regions in relaxor ferroelectrics: A case study of lead-free piezoelectrics Na $_{0.5}$ Bi $_{0.5}$ TiO $_3$ - *x* %BaTiO $_3$," *Appl. Phys. Lett.*, vol. 103, no. 24, p. 241914, Dec. 2013.

[39] A. J. Bell, Private Communication.

[40] G. Rose, "Perowskit," *Ann. Phys.*, vol. 48, p. 558, 1839.

[41] V. M. Goldschmidt, "Die Gesetze der Krystallochemie," *Naturwissenschaften*, vol. 14, no. 21, pp. 477–485, May 1926.

[42] R. E. Eitel, C. A. Randall, T. R. Shrout, P. W. Rehrig, W. Hackenberger, and S.-E. Park, "New High Temperature Morphotropic Phase Boundary Piezoelectrics Based on Bi(Me)O_3 – PbTiO_3 Ceramics," *Jpn. J. Appl. Phys.*, vol. 40, no. 10, pp. 5999–6002, 2001.

[43] H. D. Megaw, "Crystal Structure of Barium Titanate," *Nature*, vol. 155, p. 484, 1945.

[44] J. Daintith, *A Dictionary of Physics*, 6th ed. Oxford University Press, 2009.

[45] D. Bérardan, S. Franger, D. Dragoe, A. K. Meena, and N. Dragoe, "Colossal dielectric constant in high entropy oxides," *Phys. status solidi - Rapid Res. Lett.*, vol. 10, no. 4, pp. 328–333, Apr. 2016.

[46] J. W. Yeh, Y. L. Chen, S. J. Lin, and S. K. Chen, "High-Entropy Alloys – A New Era of Exploitation," *Mater. Sci. Forum*, vol. 560, pp. 1–9, 2007.

[47] M.-H. Tsai and J.-W. Yeh, "High-Entropy Alloys: A Critical Review," *Mater. Res. Lett.*, vol. 2, no. 3, pp. 107–123, Jul. 2014.

[48] C. M. Rost *et al.*, "Entropy-stabilized oxides," *Nat. Commun.*, vol. 6, no. 1, p. 8485, Dec. 2015.

[49] H. A. Jahn and E. Teller, “Stability of polyatomic molecules in degenerate electronic states - I—Orbital degeneracy,” *Proc. R. Soc. London. Ser. A - Math. Phys. Sci.*, vol. 161, no. 905, pp. 220–235, Jul. 1937.

[50] P. S. H. and and K. R. Poeppelmeier*, “Noncentrosymmetric Oxides,” 1998.

[51] K. Sakayori *et al.*, “Curie Temperature of $BaTiO_3$,” *Jpn. J. Appl. Phys.*, vol. 34, pp. 5443–5445, 1995.

[52] B. Jaffe, W. R. Cook, and H. L. Jaffe, *Piezoelectric ceramics*. Academic Press, 1971.

[53] M. Ahart *et al.*, “Origin of morphotropic phase boundaries in ferroelectrics,” *Nature*, vol. 451, no. 7178, pp. 545–548, Jan. 2008.

[54] Y. Huan, X. Wang, J. Fang, and L. Li, “Grain Size Effects on Piezoelectric Properties and Domain Structure of $BaTiO_3$ Ceramics Prepared by Two-Step Sintering,” *J. Am. Ceram. Soc.*, vol. 96, no. 11, pp. 3369–3371, Nov. 2013.

[55] M. H. Frey, Z. Xu, P. Han, and D. A. Payne, “The Role of Interfaces on an Apparent Grain Size Effect on the Dielectric Properties for Ferroelectric Barium Titanate Ceramics,” *Ferroelectrics*, vol. 206–207, pp. 337–353, 1998.

[56] M. A. Reed, “Quantum Dots,” *Sci. Am.*, vol. 268, no. 1, pp. 118–123, 1993.

[57] S. L. Sass, *The Substance of Civilization*. New York: Arcade Publishing, 1998.

[58] G. Shirane, S. Hoshino, and K. Suzuki, “X-Ray Study of the Phase Transition in Lead Titanate,” *Phys. Rev.*, vol. 80, no. 6, pp. 1105–1106, Dec. 1950.

[59] D. Kajewski, P. Zajdel, A. Soszyński, J. Koperski, I. Lazar, and K. Roleder, “Bismuth doped $Pb(Zr_{0.70}Ti_{0.30})O_3$ ceramics and their properties driven by high temperature local polarity,” *Ceram. Int.*, vol. 45, no. 8, pp. 9871–9877, Jun. 2019.

[60] B. Noheda, “Structure and high-piezoelectricity in lead oxide solid solutions,” *Curr. Opin. Solid State Mater. Sci.*, vol. 6, no. 1, pp. 27–34, Feb. 2002.

[61] J.-R. Gomah-Pettry, S. Said, P. Marchet, and J.-P. Mercurio, “Sodium-bismuth titanate based lead-free ferroelectric materials,” *J. Eur. Ceram. Soc.*, vol. 24, no. 6, pp. 1165–1169, Jan. 2004.

[62] L. Egerton and D. M. Dillon, “Piezoelectric and Dielectric Properties of Ceramics in the System Potassium-Sodium Niobate,” *J. Am. Ceram. Soc.*, vol. 42, no. 9, pp. 438–442, Sep. 1959.

[63] X. Wang *et al.*, “Giant Piezoelectricity in Potassium–Sodium Niobate Lead-Free Ceramics,” *J. Am. Chem. Soc.*, vol. 136, no. 7, pp. 2905–2910, Feb. 2014.

[64] Y. Bai *et al.*, “(Ba,Ca)(Zr,Ti)O3 lead-free piezoelectric ceramics—The critical role of processing on properties,” *J. Eur. Ceram. Soc.*, vol. 35, no. 13, pp. 3445–3456, Nov. 2015.

[65] J. Rödel, K. G. Webber, R. Dittmer, W. Jo, M. Kimura, and D. Damjanovic, “Transferring lead-free piezoelectric ceramics into application,” *J. Eur. Ceram. Soc.*, vol. 35, no. 6, pp. 1659–1681, Jun. 2015.

[66] M. McQuarrie and F. W. Behnke, “Structural and Dielectric Studies in the System (Ba, Ca) (Ti, Zr)O_3,” *J. Am. Ceram. Soc.*, vol. 37, no. 11, pp. 539–543, Nov. 1954.

[67] N. Chaiyo, D. P. Cann, and N. Vittayakorn, “Phase transitions, ferroelectric, and piezoelectric properties of lead-free piezoelectric $xBaZrO_3$–$(0.25-x)CaTiO_3$–$0.75BaTiO_3$ ceramics,” *J. Mater. Sci.*, vol. 50, no. 18, pp. 6171–6179, Sep. 2015.

[68] W. Liu and X. Ren, “Large Piezoelectric Effect in Pb-Free Ceramics,” *Phys. Rev. Lett.*, vol. 103, no. 25, p. 257602, Dec. 2009.

[69] X. G. Tang, K.-H. Chew, J. Wang, and H. L. W. Chan, “Dielectric tunability of (Ba0.90Ca0.10)(Ti0.75Zr0.25)O3 ceramics,” *Appl. Phys. Lett.*, vol. 85, no. 6, pp. 991–993, Aug. 2004.

[70] N. Chaiyo, D. P. Cann, and N. Vittayakorn, “Lead-free (Ba,Ca)(Ti,Zr)O_3 ceramics within the polymorphic phase region exhibiting large, fatigue-free piezoelectric strains,” *Mater. Des.*, vol. 133, pp. 109–121, Nov. 2017.

[71] M. Acosta *et al.*, “$BaTiO_3$ -based piezoelectrics: Fundamentals, current status, and perspectives,” *Appl. Phys. Rev.*, vol. 4, no. 4, p. 041305, Dec. 2017.

[72] Z. Yao *et al.*, “Titanium deficiency in tetragonal-structured (Ba,Ca)(Zr,Ti)O_3 piezoelectric ceramics,” *J. Alloys Compd.*, vol. 712, pp. 406–411, Jul. 2017.

[73] W. Cai *et al.*, “Effects of oxygen parial pressure on the electrical properties and phase transitions in (Ba,Ca)(Ti,Zr)O_3 ceramics,” *J. Mater. Sci.*, vol. 55, pp. 9972–9992, 2020.

[74] D. Ghosh *et al.*, “Ferroelectric Materials: Domain Wall Displacement is the Origin of Superior Permittivity and Piezoelectricity in $BaTiO_3$ at Intermediate Grain Sizes (Adv. Funct. Mater. 7/2014),” *Adv. Funct. Mater.*, vol. 24, no. 7, pp. 884–884, Feb. 2014.

[75] A. Chen, Y. Zhi, J. Zhi, P. M. Vilarinho, and J. L. Baptista, “Synthesis and characterization of $Ba(Ti_{1-x}Ce_x)O_3$ ceramics,” *J. Eur. Ceram. Soc.*, vol. 17, no. 10, pp. 1217–1221, Jan. 1997.

[76] G. Canu *et al.*, “Structure-property correlations and origin of relaxor behaviour in $BaCe_xTi_{1-x}O_3$,” *Acta Mater.*, vol. 152, pp. 258–268, Jun. 2018.

[77] J. H. Hwang and Y. H. Han, “Dielectric Properties of $(Ba_{1-x}Ce_x)TiO_3$,” *Jpn. J.*

Appl. Phys., vol. 39, no. Part 1, No. 5A, pp. 2701–2704, May 2000.

[78] G. Confalonieri, V. Buscaglia, G. Canu, M. T. Buscaglia, M. Dapiaggi, and IUCr, "The local and average structure of Ba(Ti,Ce)O_3 perovskite solid solution: effect of cerium concentration and particle size," *J. Synchrotron Radiat.*, vol. 26, no. 4, pp. 1280–1287, Jul. 2019.

[79] X. Wang, J. Yue, and J. Liu, "Enhanced temperature stability and electrical properties of Bi/Mn co-doped (Ba,Ca) (Zr,Ti)O_3 lead-free ceramics," *Ceram. Int.*, vol. 47, no. 2, pp. 2525–2530, Jan. 2021.

[80] X. Liu *et al.*, "Enhancing piezoelectric properties of BCZT ceramics by Sr and Sn co-doping," *J. Alloys Compd.*, vol. 640, pp. 128–133, Aug. 2015.

[81] G. M. Osoro, D. Bregiroux, M. P. Thi, and F. Levassort, "Structural and piezoelectric properties evolution induced by cobalt doping and cobalt/niobium co-doping in $BaTiO_3$," *Mater. Lett.*, vol. 166, pp. 259–262, Mar. 2016.

[82] W. Hu *et al.*, "Electron-pinned defect-dipoles for high-performance colossal permittivity materials," *Nat. Mater.*, vol. 12, no. 9, pp. 821–826, Sep. 2013.

[83] M. A. Subramanian, D. Li, N. Duan, B. A. Reisner, and A. W. Sleight, "High Dielectric Constant in $ACu_3Ti_4O_{12}$ and $ACu_3Ti_3FeO_{12}$ Phases," *J. Solid State Chem.*, vol. 151, no. 2, pp. 323–325, May 2000.

[84] I. P. Raevski, S. A. Prosandeev, A. S. Bogatin, M. A. Malitskaya, and L. Jastrabik, "High dielectric permittivity in $AFe_{1/2}B_{1/2}O_3$ nonferroelectric perovskite ceramics (A=Ba, Sr, Ca; B=Nb, Ta, Sb)," *J. Appl. Phys.*, vol. 93, no. 7, pp. 4130–4136, Apr. 2003.

[85] Z. Wang, X. M. Chen, L. Ni, and X. Q. Liu, "Dielectric abnormities of complex

perovskite Ba($Fe_{1/2}Nb_{1/2}$)O_3 ceramics over broad temperature and frequency range," *Appl. Phys. Lett.*, vol. 90, no. 2, p. 022904, Jan. 2007.

[86] S. Saha and T. P. Sinha, "Low-temperature scaling behavior of $BaFe_{0.5}Nb_{0.5}O_3$," *Phys. Rev. B*, vol. 65, no. 13, p. 134103, Mar. 2002.

[87] C.-Y. Chung, Y.-H. Chang, and G.-J. Chen, "Effects of lanthanum doping on the dielectric properties of Ba($Fe_{0.5}Nb_{0.5}$)O_3 ceramic," *J. Appl. Phys.*, vol. 96, no. 11, pp. 6624–6628, Dec. 2004.

[88] X. Sun *et al.*, "Grain boundary defect compensation in Ti-doped $BaFe_{0.5}Nb_{0.5}O_3$ ceramics," *Appl. Phys. A*, vol. 122, no. 9, p. 864, Sep. 2016.

[89] U. Intatha, S. Eitssayeam, and T. Tunkasiri, "Giant Dielectric Behavior of $BaFe_{0.5}Nb_{0.5}O_3$ Perovskite Ceramic," in *Condensed Matter Theories*, 2008, pp. 429–435.

[90] D. Bochenek, P. Niemiec, M. Adamczyk, and I. Szafraniak-Wiza, "Physical properties of lead-free $BaFe_{1/2}Nb_{1/2}O_3$ ceramics obtained from mechanochemically synthesized powders," *J. Mater. Sci.*, vol. 53, no. 19, pp. 13501–13512, Oct. 2018.

[91] D. Bochenek, P. Niemiec, I. Szafraniak-Wiza, M. Adamczyk, and R. Skulski, "Preparation and dielectric properties of the lead-free $BaFe_{1/2}Nb_{1/2}O_3$ ceramics obtained from mechanically triggered powder," *Eur. Phys. J. B*, vol. 88, no. 10, p. 277, Oct. 2015.

Chapter 2

2. EXPERIMENTAL METHODS

Synthesis and processing methods for oxide based ceramic materials vary widely, though all methods contain a thread of commonality. In all syntheses of oxide-based ceramics, precursor reagents (generally primary metal oxides and carbonates) must be combined in some manner stoichiometrically to form the target compound. These mixed reagents are then treated via an external stressor (chemical, thermal, pressure), resulting in initial nucleation and formation of the target compound. The resultant phase mixture is then collected, formed into a sample, and then finally reacted to completion forming a single phase, dense, ceramic body of the target solid solution. Further complicating matters are the various realms of these materials, bulk polycrystalline ceramics, and thin film ceramics. This work focuses solely on the fabrication of bulk polycrystalline ceramics through the mixed oxides solid-state method.

2.1 Materials Processing: The Mixed Oxides Solid-State Method

The mixed oxides solid-state method consists of stoichiometric massing of precursor fine-grained (sub-micron) powder reagents to form a set mass of the target compound. These massed reagents are then mixed into a slurry with ethanol and homogenized through ‘milling’ with dense ceramic media, normally yttria-stabilized zirconia (YTZ). This milling is a pulverization process which breaks apart any formed agglomerates and maximizes reactant grain surface area for reaction through minimizing particle size. Milled powders are then dried with the milling media removed from the solution, forming an initial ‘batched’ powder. This batched powder is then heated to a set temperature to form initial nucleation of the final product, ‘calcined,’ milled again to maximize reaction surface area after any crystallite growth through the initial calcination, and then formed into dense ‘green bodies’ through application of high pressure in a die press. The green bodies are then heated again at a higher temperature, typically within 10% of the theoretical melting point of the target compound, also known as ‘sintering.’ Here the initially formed nucleates react and grow to completion, producing a dense, single phase sample.

2.1.2 Initial Powder Processing

Initial powder processing is a function of analytical massing and wet milling. In this work, all precursor reagents were massed stoichiometrically and combined with ethanol (EtOH) into a slurry of 80 wt% EtOH. Special considerations were made for precursors not of primary oxides, namely carbonate based and hydroxide-based precursors. As these precursors readily hydrate with ambient humidity, and any mass due to hydration not accounted for in calculations will drive the final composition off the desired stoichiometry, precursors of this type were kept in a constant temperature oven at 120°C. These precursors were also massed while hot to achieve the highest degree of accuracy with the calculated stoichiometry, as the degree of hydration for hydrophilic materials is impossible to be known on a given day with a given humidity level and therefore impossible to account for adequately in any stoichiometry calculations. Finally, once all precursors are massed, ‘batched,’ and combined with 80 wt% EtOH into a slurry, cylindrical YTZ media, of 1 cm diameter and 1 cm height, were added at a ratio of 1.2

media/gram batched powder (rounding to the nearest integer) in preparation for wet milling.

2.1.2.1 A Quick Note on Safety

As a large portion of the work undertaken was in use of a highly toxic and hazardous material, PbO, it was always of utmost importance to use adequate personal protection equipment (PPE) handling this material. As the PbO used was of nano-sized crystallites, PPE included well ventilated (negative pressure) spaces, respirator masks with appropriate filter ratings when handling the raw reagent powder, eye protection and lab coats. All PbO related processing is to be handled with care, and any instrument used in said processing (scoopulas, drying bowls, mortar, and pestle, etc.) was Pb-contaminated and only used in processing of materials where Pb was a component of the system.

2.1.3 Wet Milling and Calcination

In this work, wet milling of slurried batched powders with sufficient YTZ media was performed on a high energy random-orbital vibratory mill for 6-10 hours depending on desired crystallite size. The main purpose of this milling step is to homogenize the precursor powders within the slurry, as well as break up any large particle agglomerates and minimize crystallite size to maximize surface area for reaction. With adequate milling times, required temperatures for reaction can theoretically be minimized and therefore initial nucleation of the desired phase can be achieved at lower temperatures and dwell times. As most ceramic oxides must be reacted at relatively high temperatures (> 1,000°C,) and that some primary oxides will readily volatilize due to low vapor pressures, achieving maximum reactive surface area to minimize calcination temperatures as well as dwell times can be very important. After milling, homogenized slurries are then recovered and separated from the YTZ media and allowed to dry. Dried batched powders are then placed into ceramic crucibles (alumina, Al_2O_3, or magnesia, MgO, depending on possible solubility of reagents with the crucible, i.e., BaO readily forms stable phases with Al_2O_3 at high temperature [1]) for calcination. Samples in covered crucibles are then heated in high temperature furnaces to the set calcination temperature, generally with quick heating and cooling rates, for a set dwell time. While dwell times are generally on the order of 2-4 hours, and temperatures are ~20% of the theoretical melting point of the target composition, best calcination temperatures and dwell times must be determined experimentally on a case-by-case basis. Upon successful calcination of loose batched powders, it will commonly be seen that powders will densify to varying degrees in the crucible which is characterized by the loose powder receding from the edges of the crucible 'caking.'

Calcined powders are then removed from crucibles and gently pulverized in a mortar and pestle if densified to any degree. At this point, X-ray diffraction is utilized to determine the extent, if any, of formation of the desired phase. If, indeed, diffraction peak intensities of the desired phase are observed in initial X-ray diffraction studies, then the calcined powder is ready for a secondary milling step, to again break up any agglomerates formed (missed by mortar and pestle pulverization) and reduce any grain growth during calcination prior to being formed into samples. Once milled, the slurry is again dried, and the resultant calcined powder is ready for sample processing.

2.1.4 Green Body Formation – Uniaxial Pressing

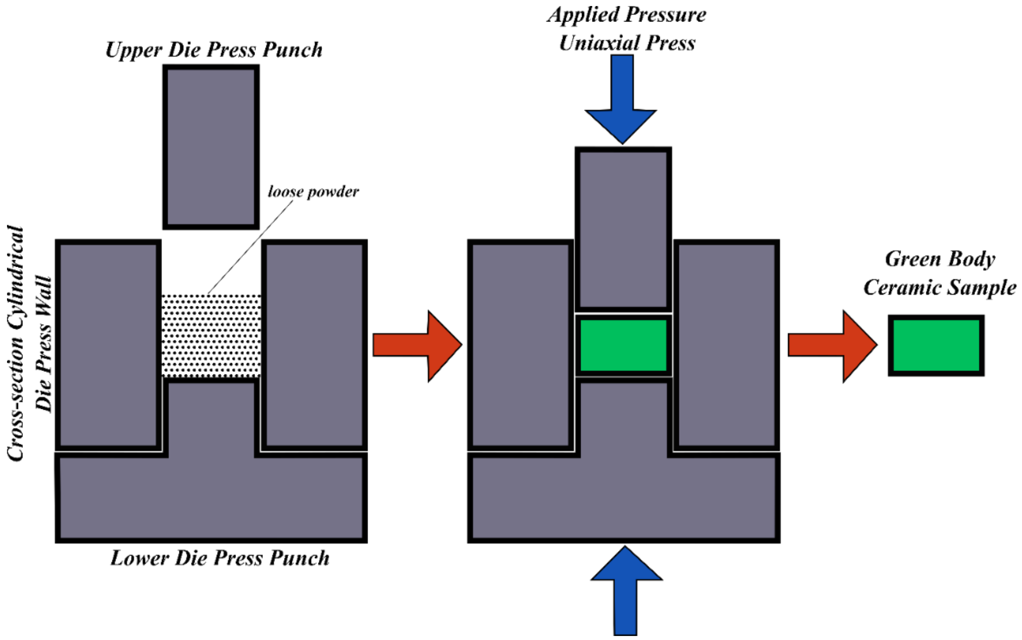

Figure 2.1: Schematic showing formation of ceramic green body from loose powder through uniaxial pressing in a die press

To form the loose calcined powders into dense, single phase, ceramics, it is first formed into ~1 mm thick, 13 mm diameter, cylindrical pucks known as green bodies. First, the powder is massed into approximate amounts necessary to form ~1mm thick pellets. As this mass is a function of the atomic weight of the elemental components, compositions with large fractions of more massive elements (like lead) require larger masses of calcined powder (~0.5 grams for barium titanate based solid solutions and ~1.5 grams for Pb based solid solutions.) Once massed, the powder is then, optionally, processed further through the addition of sintering/pressing aides (to be discussed later) or elemental excess to account for volatile compounds (such as PbO and Bi_2O_3) before being added into a 13mm cylindrical die press as seen in **Fig. 2.1**. Samples are then pressed at 170 MPa for 3 mins in a uniaxial hydraulic press resulting in solid green bodies. These bodies are then set into a ceramic crucible (same considerations for alumina or magnesia use as before hold) for the final sintering step. In the crucible, green bodies are set upon a small layer of calcined powder of same composition known as ‘sacrificial’ (sac) powder. The green body is then covered in sacrificial powder of the same composition, and the crucible is covered with a ceramic lid, readying the sample for the sintering step. As diffusion readily occurs across the surfaces of green bodies, sacrificial powder is used to mitigate this diffusion by minimizing the chemical gradients between the surfaces of the green body and the crucible (bottom) and air (top/sides).

It should also be noted that pressing of green bodies can also be used prior to calcining in effort to maximize diffusion of reaction by minimizing void space in the loose powder. In this case, calcined green bodies densify significantly and must be pulverized prior to milling. This technique is generally employed if it is observed that loose powder does not calcine homogenously (observation of inhomogeneous coloring and densification of the loose powder.) However, as these techniques do not work well with mixed precursor reagents (use of oxides and carbonates) as done in this work, no issue of inhomogeneous calcining was encountered, and this extra step is a possible point for impurity incorporation into the sample, it was not necessary and therefore not utilized.

2.1.4.1 Use of Pressing/Sintering Aides – Liquid Phase Binders

As crystallite grains are rigid bodies of relatively high hardness, they have large wetting angles when interacting with other crystallites and, generally, will not be able to pack efficiently under high pressure due to incongruous shaping. This can result in packing faults during pressing, large pores or void spaces inside the green body, or non-stable green bodies that crumble or fall apart after removal from the die press. Note that, while general, this is not always true and must be determined experimentally on a case-by-case basis. To combat these problems with green body formation, there are various methods to apply. One technique is to ensure that the powder is of finest crystallite size possible (and of homogenous size distribution), as the smaller the crystallite, the larger the surface area and amount of high energy surfaces. This requires various milling steps with intermixed sieving to remove agglomerates and crystallites that are too large. Sieving also ensures semi-homogenous crystallite size distributions which also helps reduce these effects and requires low pressure < 100 MPa pressing for very short periods of time (order of 10s of seconds) to achieve stable green body formation.

These techniques, while effective, are tedious, time consuming, and are not always sufficient to solve the problem. Therefore, a more common approach is the use of a polymer-based liquid phase binder. These binders are additives mixed into the calcined powder pre-pressing, where the polymer binder is dissolved in a polar solvent (ethanol, acetone, xylene) at small weight percentages (wt. %) then mixed with the calcined powder in mortar and pestle. Upon mixing, the solvent evaporates leaving behind the polymer binder, and the dried calcined/polymer powder mixture is ready for pressing. Under high pressure, the polymer binder (Polyvinyl Butryal, PVB, dissolved in EtOH as used in this work) undergoes a phase transition from solid to liquid, hence the terminology of 'liquid-phase binders.' The binder creates a ceramic-liquid composite, where the binder wets all crystallite surfaces, effectively reducing the wetting angle between crystallites and allowing for efficient packing fractions. After pressing, the polymer binder returns to a solid state existing between crystallite boundaries within the green body. This polymer can easily be removed through thermal annealing, as most organic based compounds will vaporize above 250°C. To ensure all organic compounds are burned off, a 450°C/2-4 hours thermal step is added to sintering profiles when polymer binders are used. In this work 1-4 wt.% PVB (determined experimentally) was used for all fabricated samples.

Another common addition to samples, pre-green body formation, are termed 'sintering aides.' These additions have no function during actual green body formation but help to form dense, single-phase samples, during the actual sintering process. They have functions from lowering the overall melting point of the system, allowing for lower sintering temperatures, to accounting for non-stoichiometries which arise from component volatilization at high temperature.

2.1.4.2 Considerations for Componential Volatilization

Some primary metal oxides have a very low vapor point (relative to the high sintering temperatures needed for ceramics) and will readily volatilize at high temperatures. In this work the two main species of interest are PbO and Bi_2O_3. As any form of volatilization will result in non-stoichiometry and unsuccessful processing of samples (inhomogeneities in sintered sample, off-stoichiometry defect incorporation, delamination, cracks, etc.,) managing volatile components during sintering can be very important.

There are multiple avenues utilized to deal with volatilization. One avenue is to first react volatile elements through secondary pathways of reaction. If a metastable compound exists between the volatile component and another component in the system, those two reagents can first be reacted into the meta-stable phase, that is stable prior to volatilization temperature, then react meta-stable phase normally to form desired product. This however is limited, as not all components in a solid solution will have meta-stable phases for secondary reaction pathways, and (even if they do) it is not guaranteed that the meta-stable phase forms at a low enough temperature to avoid volatilization.

Another avenue to mitigate vaporization of volatile reagents is to address the mechanism of volatilization itself. As it is a function of partial pressure and chemical gradients, large amounts of sacrificial powder can be used to reduce possible chemical gradients (between sample surfaces and air/crucible.) The sacrificial powder can also preferentially volatilize, prior to the sample, and create an equilibrium partial pressure environment in the crucible, inhibiting further volatilization.

Finally, a very commonly used avenue is the incorporation of excess constituents of the volatile reagent into sample pre-green body formation, or into sacrificial powder to account for stoichiometry lost due to volatilization. This amount of excess is generally experimentally determined but varies from 1 mol% to 10 mol%. In this work, 3 mol% excess of PbO was sufficient to achieve dense, phase pure samples of $Pb(Zr,Ti)O_3$. Also note that these volatile elements are an inherent health and safety hazard, and necessary safety precautions in the processing and fabrication of materials with these elements should always be observed. In this work, all high temperature furnaces used for lead-based processing were done in a fume hood with adequate chemical scrubbers to ensure no leeching of toxic chemicals into ambient atmosphere.

2.1.4.2.1 Seasoning – Furnace and Crucible effects

Another factor to account for in dealing with volatile components is the crucible. As crucibles are porous ceramics of differing chemical makeup to the samples being made, they are another source of chemical gradients within the sintering system, as well as source of physisorption or chemisorption for the evaporating species. In fact, it can be visually observed that ceramic crucibles will absorb evaporated oxides during sintering through changes in coloring of the crucible walls. While not known to any scientific certainty, due to inherent difficulties of observing these chemical gradients at such high temperatures, it is widely acknowledged that using 'seasoned' crucibles, crucibles in which the volatile substance have been used in prior and show evidence of deposition, to inhibit the excess chemical gradient, as well as be a source of excess vapor pressure, is necessary in producing dense, single phase samples which contain volatile precursors.

This phenomena was encountered experimentally in this work in the sintering process of $Pb(Zr_{0.52}Ti_{0.48})O_3$, pertaining to the research discussed in Chapter 3. Initial processing of these samples had a very high failure rate ~75% of samples fabricated had some inherent physical flaw (low density, macroscopic faults, delamination, gradient densities, etc.) even with excess PbO incorporated into the sample. In effort to explore the source of this issue, four samples of varied PbO excess incorporated into the green body were arranged in a new, unused, alumina crucible with sacrificial powder. To ensure that the sintering environment was sufficiently saturated with PbO and drive any possible chemical gradients away from leeching PbO from the samples, piles of raw PbO were deposited between samples in the crucible as depicted in the diagram in **Fig. 2.2**. Post-sintering, it was observed that all piles of raw PbO had volatilized with no trace of powder left on the crucible where they were deposited. However, it was observed that the walls of the new crucible underwent a color change and appeared the color of raw PbO powder, suggesting that the piles of raw PbO powder volatilized and physiosorbed into the walls of the virgin crucible. The sintered samples were of high quality and density with no

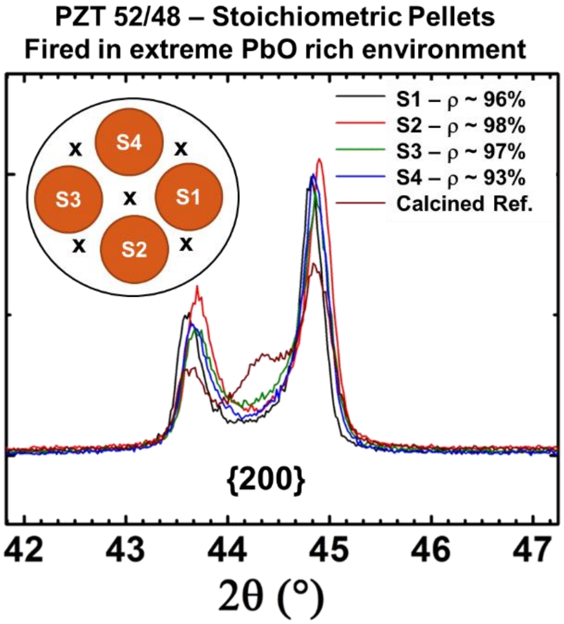

Figure 2.2: X-ray diffraction of the {200} family of planes in $Pb(Zr_{0.52}Ti_{0.48})O_3$ samples fired in a highly PbO rich environment. The 'x's' on the inserted diagram represent piles of raw PbO deposited prior to sintering which no longer were present post sintering. The identifier 'S1-S4' represent Sample 1 – Sample 4 in which varying degrees of PbO excess were incorporated into the green body sample, S1 containing 3 mol % Pb excess, S2 containing 5 mol% Pb excess, S3 containing 10 mol% Pb excess and S4 being the nominal stoichiometric control.

observable flaws or inhomogeneities and exhibited density differences reflecting the extent of PbO excess incorporated into the sample (lower density S4 containing no excess, highest densities, S2/S3, of highest excess in **Fig 2.2**). This suggests that, to account for componential volatilization in a system, both the use of stoichiometric excess and seasoned crucibles are necessary to produce dense samples.

2.1.5 Sample Preparation and Sintering

Once all considerations for necessary additions to calcined powders to achieve dense single-phase samples has been made, and the samples have successfully been pressed into stable green bodies, samples are ready to be prepared for the final sintering process. Green body samples are arrayed in crucibles, set on top of a bed of calcined sacrificial powder of the same composition to the sample and covered in the same sacrificial powder, ensuring that edges of the sample are adequately covered as well. Prepared crucibles are then covered and inserted into a furnace for sintering.

The temperature at which samples are sintered is a function of the melting point of the target materials system. In general, highest densities are achieved as the melting point is approached, however any melting that occurs will ruin the sample completely. As most materials systems being made are either novel or relatively unknown, melting points must be approximated by the rule of mixtures – which states that the resultant properties of a solid solution between compound A and B will be a weighted average of the two components individual properties. While these approximations are generally accurate, they fail to account for secondary effects which can artificially lower the melting point. This, and the fact that high temperature furnaces typically have not-well defined thermal gradients within a furnace (deviating from the reported temperature) and temperature can fluctuate unexpectedly, leads to the general acceptance that sintering temperatures should be chosen typically ~10% below the theoretical melting point. This tends to lead to adequate sintering temperatures for theoretical solid solutions, and experimental methods can be used to improve best sintering practices.

Dwell time at sintering temperature, and heating/cooling rates, also tend to be experimentally determined sintering parameters. As these parameters govern the amount of time the sample is at high temperature, they govern all diffusion driven kinetic processes during sintering and sufficient dwell time for full reaction, grain growth, and densification must occur. However, too long of dwell time, or too low of a cooling rate, can lead to too much grain growth or stabilization of defects in oxides. In this work, a dwell time of 4 hours, with heating/cooling rates of 2°C/min, was chosen for sintering unless parameters are already well defined in literature.

Once single-phase samples are obtained, their as-sintered density is measured via the Archimedes principle and compared to theoretical densities as determined from single phase XRD patterns and target solid solution composition. Desired percent densities for dense samples are >90% theoretical density, as beneath this density percentage the amount of void-space, of permittivity between ε_0 and ε_{air}, in the sample is large enough to noticeably convolute the materials properties. These dense, single-phase, samples are then polished using progressively finer grit silica-based polishing paper until mirror polish to remove the as-sintered defect surfaces and obtain near-parallel surfaces, ensuring parallel-plate capacitor configuration during characterization.

2.1.6 Electrode Application

Finally, once parallel surfaces of mirror polish are obtained and the physical dimensions of the sample are recorded, electrodes are applied to the surfaces of the sample for characterization. Two types of electrodes were utilized in this work for ambient measurements and non-ambient measurements. For ambient measurements, gold electrodes were applied using a plasma-based target sputtering setup. To ensure that no electrode material was deposited on the edges of the sample, acetone-based varnish was applied to the edges prior to sputtering, and removed post-sputtering using an acetone bath. For non-ambient measurements, high or low temperature, silver electrodes were painted on sample surfaces and thermally annealed at a temperature 100°C above the max temperature to be used in characterization (generally 750°C) for 30 mins. In this work, most samples underwent non-ambient characterization techniques so silver painted electrodes were generally used.

2.2 Density Measurements – Archimedes Method

Post-processing, various techniques are utilized to explore and characterize the samples crystallographic structure, microstructure, and electronic properties. As bulk ceramic samples are arrays of tightly stacked, rigid crystallites, they do not always tend to pack in the most efficient manner. Any packing faults that occur during sample processing, and are not relieved during the sintering process, result in the incorporation of void-space, or pores, in the sample. As these pores will have very low permittivities, the overall permittivity of the sample will be of a composite permittivity of the material itself and the permittivity of the void spaces. Therefore, the Archimedes principle is utilized to determine the density of the sample relative to that of deionized water at room temperature. The calculated density of the sample is then compared to the theoretical density of the sample to determine its percent theoretical density. This theoretical density is determined either from literature sources of the sample, or X-ray diffraction studies used to determine the materials crystallographic structure in combination with the expected stoichiometric composition of the target solid solution. Theoretical densities of less than 90% are not sufficiently dense for purposes of materials characterization as the ratio of void-space to sample mass is too high and the permittivity of the pores becomes a substantial fraction of the samples measured properties.

2.3 Structure Characterization – X-ray Diffraction

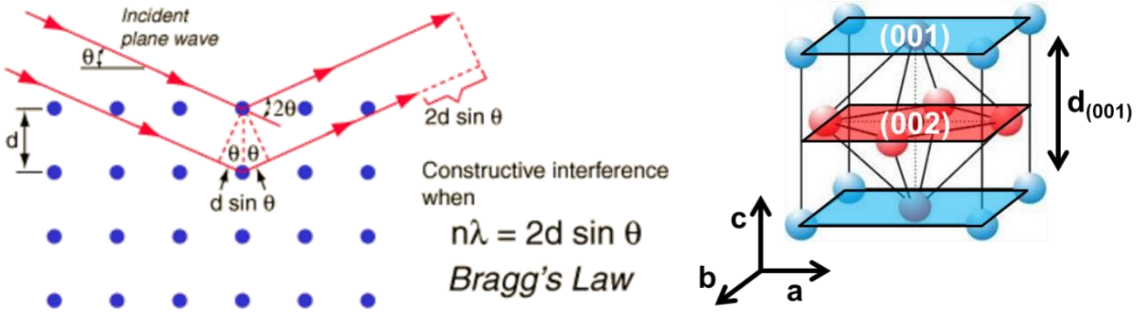

Figure 2.3: X-ray diffraction off planes of atoms in a lattice due to constructive interference at angles of coherence, image taken from Hyperphysics by *R. Nave*, (left) with a representative perovskite unit cell giving physical reference to the lattice planes (right)

After the discovery of X-rays by Roentgen in 1895 [2], it took less than two decades for novel techniques using X-rays to elucidate the structure of materials to be developed. By 1913, father and son researchers William Henry and Lawrence Bragg developed the law by which the well-known diffraction paradigm (defined by the famous double-slit experiment in 1801 by Thomas Young [3]) could be applied with X-rays to probe planes of atoms in a well-defined lattice, as the wavelength regime of X-rays are of the right order of magnitude to interact with the planar separation distances in the average unit cell, and X-rays can inelastically scatter off of core shell electrons in an atom. This law is known as Bragg's Law and is seen here [4]:

$$n\lambda = 2 \cdot d \cdot \sin(\theta)$$

Where n is an integer term describing the plane order, λ is the discrete wavelength of diffracting X-rays, d is the distance separating the crystallographic planes, and θ is the angle of incidence between the incident X-rays and the surface of the crystal. This relationship can be visualized and derived from **Fig. 2.3**.

Applying this law to the paradigm of a crystal, a motif of atoms on a translationally repeatable matrix of lattice points seen in **Fig. 2.3**, diffraction will occur at specific angles of θ, or experimentally 2θ for incident and diffracted (measured) beams, where planes of lattice points are in coincidence leading to constructive interference of diffracted beams. These instances of constructive diffraction are measured by the intensity of the diffracted beam and, for a perfect single crystal, would show up as instantaneous delta peaks. The collection of these delta peaks through 2θ space generates a diffraction pattern which reflects the symmetry of the unit cell as well as its physical dimensions. For non-idealized crystals, and polycrystals, the diffraction peaks grow in breadth (reflecting a Maxwell-Boltzmann distribution), reflecting the relative size of the crystallites, or their average size distribution, and any inherent stress between crystallites. Also, as crystals vary in symmetry and lattice types (spatially defined by the lattice parameters a, b, and c), interplay between the equality relationship of a, b, and c will give rise to degeneracy and peak-splitting when degeneracy is broken. For example, in the cubic case of a=b=c, an instance of diffraction off of the (100) plane will be equal to that of the (010) plane and (001) plane (visualized in **Fig 2.2**), however in the tetragonal case of a=b≠c, an instance of diffraction off of the (100) plane will be equal to that of the (010) plane but not equal to that of the (001) plane. This breaks the degeneracy of the cubic case so the {100} peak will be split into two distinct peaks in 2θ space, one representing the (100) as well as the (010) and one representing the (001). Furthermore, in a perfect randomly oriented polycrystal, diffraction conditions for all these planes are equiprobable, so the ratio of the degeneracies is maintained in the relative peak intensities arising from the break in degeneracy (i.e. 2:1 ratio in the tetragonal case.)

2.3.1 Qualitative Approaches

In general, for experimental ceramics research, XRD patterns are used, and interpreted, on a qualitative (visual) basis to determine the phase-purity of a sample as well as a first approximation of the samples ambient crystallographic phase. While XRD patterns are very complex and a convolution of various materials and experimental parameters, if a majority phase is present in the sample it can be a relatively straight forward process to identify impurity phases and basic symmetry elements. Impurity phases present in the material will diffract readily in a diffraction experiment (if present to any substantial extent) and therefore readily show up on a diffraction pattern at low relative intensities. Determination of these impurity phases can be difficult, however, as normally only the most intense peak of the impurity phases diffraction pattern will be present. Furthermore, as all materials in this work are of the perovskite structure, determining a first approximation of their crystallographic phase is possible as splitting patterns exhibit very characteristic qualifying attributes. For example, a tetragonal perovskite will show multiple peak intensities (all peaks that are not of relation to {111} family of planes) that are split at a 2:1 intensity ratio due to the elongation of the c-axis, and a rhombohedral (a=b=c) perovskite will have non-split peaks except the evolution of a shoulder on the tetragonal (111) due to the variation of the unit cell angle alpha from 90°. While these qualitative techniques are sufficient for informing the experimental process in developing novel ceramics, they do not provide solid evidence to make substantial claims about a materials structure. Further quantitative analysis through modelling of data from precisely controlled XRD experiments is necessary for such assertions.

2.3.2 Iterative Modelling Techniques – Pawley Fitting

Various orders of iterative modelling techniques exist for the quantitative study of XRD data. As there are many variables that can affect said data (both material and experimental) it is commonplace to employ at least two techniques: Pawley fitting analysis and Reitveld [5]. Pawley fitting is a least squares iterative modelling approach which leaves the intensity of the diffracted X-rays un-refined [6]. This allows for more provisional modelling, sufficient mostly to determine accurate peak positions in a diffraction pattern, which govern the materials space group (*hkl* positions) and lattice parameters. Once these parameters have been accurately determined through Pawley fitting, they can be used as a starting point the more complex modelling of Rietveld, which also refines intensity. As this work is more focused on elucidating the properties of novel materials rather than their structure, modelling techniques were scarcely utilized. However, Pawley fitting would be used if any degree of uncertainty existed in the materials crystallographic phase from qualitative analysis for purpose of determining theoretical density values and phase diagrams.

2.4 Microstructure Characterization – Scanning Electron Microscopy

To further characterize a samples physical properties, scanning electron microscopy (SEM) can be used to clarify a samples microstructure. Utilizing beams of accelerated electrons and various optic lenses for magnification, an SEM allows for probing the topography a surface in a sample as well as the surfaces composition through interactions of the electron beam and surface atoms of the sample. As most samples considered in this work are electronically insulating, they will not readily interact with an impinged electron beam, and therefore must be coated with nanometer thin coatings of conductive materials. If prepared correctly, this technique allows for direct observation of grain boundaries in a sample (and therefore average grain size) as well as the extent of the sample's porosity, with newer SEMs, dating as far back as 1991, able to achieve resolutions of up to 1 nanometer [7]. To clearly resolve grain boundaries in bulk polycrystalline materials, the sample must be thermally annealed to grow and resolve the grain boundaries. General practice for this process (commonly referred to as 'thermal etching') is to anneal the freshly polished, or fractured, surface of a ceramic sample at ~10% of the sintering temperature for approximately 1 hour, i.e. a sample sintered at 1400°C would be thermally etched at 1260°C for an hour as a starting point, however this is a 'rule of thumb' and best practices for thermal etching must be determined experimentally. In SEM it is also possible to resolve impurity phases (generally small anomalous crystallites aggregated at grain boundaries,) however it must be noted that these images constitute very small fractional areas of the actual physical sample, and SEM images can vary to a significant extent depending on the spatial probing area. To this regard, results from SEM images should be reported, and considered, accordingly, to forestall conclusions which may adequately represent what is seen in an individual scan, but not represent the entire sample.

2.5 Electronic Characterization

Complimentary to defining the physical characteristics of a sample, and central to this work, is probing and elucidating the samples electronic properties. As most of the materials considered in this work are insulative, non-conductive materials, there are two main categories of utilizable techniques for characterization: low voltage spectroscopy and high voltage. Low voltage spectroscopy is utilized to experimentally determine the capacitance of a sample over a broad range of frequencies, from which the materials relative permittivity is calculated, and high voltage measurements are used to determine the bulk polarization response of the material. In both techniques, the samples thickness and electroded area are necessary components, as the sample is probed as a parallel plate capacitor.

2.5.1 Low Voltage Characterization – Dielectric Spectroscopy

Dielectric spectroscopy is utilized to determine the permittivity of a material, as well as the major mechanisms giving rise to that permittivity. As observed in **Fig. 1.7**, the major mechanisms giving rise to polarization, and therefore permittivity, are frequency dependent, so measuring the capacitance of the material as a function of frequency of the applied current will allow the elucidation of said mechanisms. These measurements are done at low field (or low voltage) as the application of high voltage can bias the results as to give capacitance values not representative of the materials inherent permittivity (polarization due to domain growth and reorientation, non-real capacitance due to charge

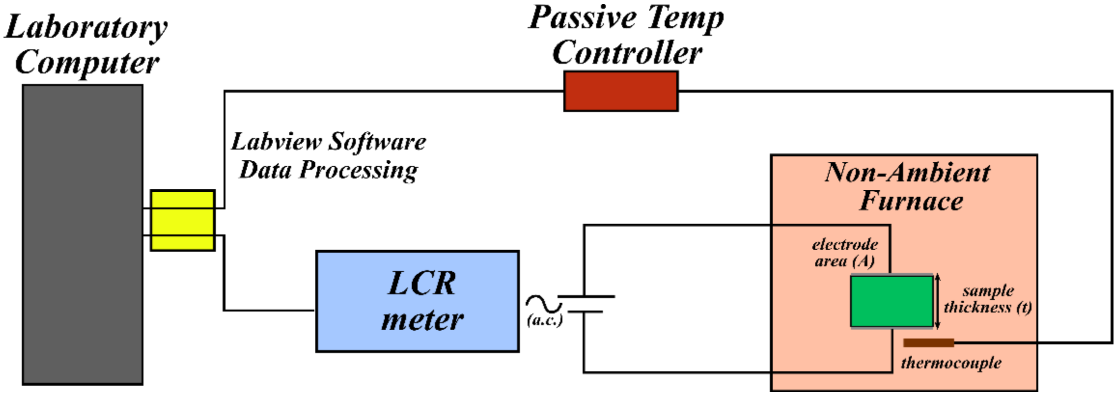

Figure 2.4: General schematic of experimental setup for dielectric spectroscopy. Low temperature experiments utilize a delta box with liquid nitrogen (-150°C to 300°C capabilities) and high temperature setups utilize a high temperature tube furnace (r.t. to >650°C capabilities)

mobility or conduction.) Generally, these measurements are made with the use of an inductance, capacitance, and resistance (LCR) meter or an impedance analyzer, and, due to the passive nature of the experimental setup, they can be easily made *in situ* with regards to temperature as seen in **Fig. 2.4** (image developed from [9], [10]). The experimentally measured values in this setup are the overall capacitance of the sample, C', and dielectric loss of the sample, $\tan \delta$. Also, as LCR meters can vary the applied voltage, rudimentary studies into the voltage dependence of the dielectric permittivity can directly be measured. These measurements are done at low oscillating voltages, < 1V, and can be used to quickly confirm the extent of space charge contribution to the materials permittivity. In materials with high amounts of space charge, the loss will rapidly and greatly increase with small increases of voltage due to an induced current.

2.5.1.1 High Temperature Permittivity – ProboStat Setup

For high temperature dielectric permittivity experiments, the LCR meter is connected to a tubular probe known as a ProboStat [8]. This large ceramic probe consists of a hollow inner ceramic pillar with platinum wiring running through it to make bottom contact with the sample. Sitting on top this pillar, the sample is held into place with a triangular ceramic puck and thin ceramic arms which are locked using springs to ensure the sample does not move. Finally, a thermocouple is inserted near the sample at the tip of the pillar setup and the entire apparatus is covered by a large hollow cylindrical ceramic sleeve. The entire apparatus, seen in **Fig. 2.5 (a)** (image developed from [9], [10]) can then be inserted into a tube furnace, ensuring that the sample is centered within the tube furnace. Utilizing this ProboStat setup allows for passive dielectric measurements up to

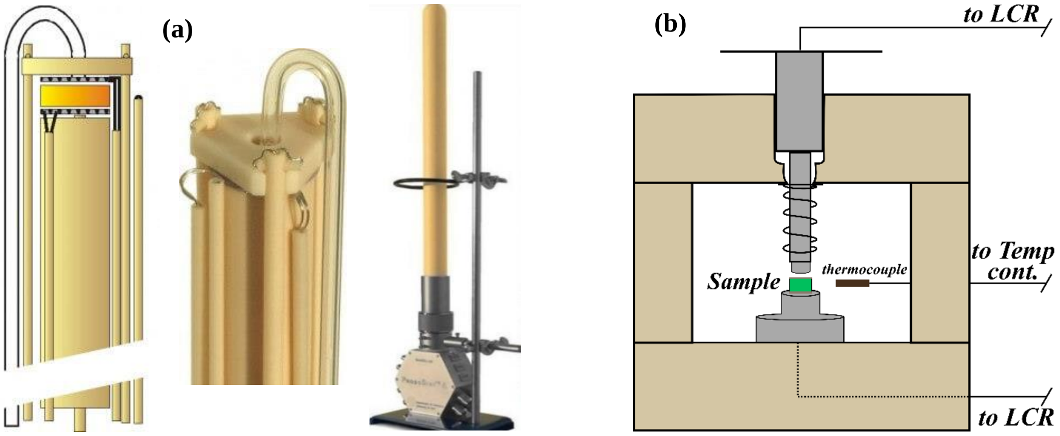

Figure 2.5: (a) Schematic of sample cell for non-ambient ProboStat, far-left, physical representation of schematic, left-middle, and fully enclosed sample cell of ProboStat for insertion into tube furnace (image developed from [9], [10]), and (b) schematic of sample cell for insertion into Delta box low temperature furnace (ceramic plate covers for front and back to seal cell not pictured)

temperatures greater than 650°C, as well as incorporation of non-ambient environmental gradients across the sample although this functionality was not utilized in this work. General temperature profile for high temperature scans are 2-3°C/min heating rate to 650°C with a 30 min hold and 2-3°C/min cooling. Temperature resolution is relatively high as the LCR meter passively sweeps frequencies from 100Hz to 1MHz within 1 min time.

2.5.1.2 Low Temperature Permittivity – Delta Box Setup

Experimental setup for low temperature permittivity measurements are much more straight forward. A simple sample stage for insertion into a Delta Box low temperature, seen in **Fig. 2.5 (b)**, furnace (Delta Design, San Francisco, CA) was developed, and machined, with a loose spring-loaded top contact and thermocouple mount near the sample. It must be ensured that the sample is physically enclosed within the delta box, as the furnace regularly injects high pressure liquid nitrogen into the furnace area on cooling. If not properly enclosed, temperature readings at the thermocouple will vary widely and convolute the data. Due to the nature of the heating and cooling programs on the Delta box, only data of the cooling run is of sufficient temperature resolution, and a typical thermal profile consists of heating to 200°C at 20°C/min, an equilibration dwell of 10 mins, and then cooling to -150°C at 3°C/min with an equilibration dwell of 10 mins. To conserve liquid nitrogen, heating rates after min temperature are 20°C/min as well.

2.6 High Voltage Characterization: Polarization and Strain

To characterize the ferroelectric and indirect piezoelectric properties of these materials, a high voltage Radiant Technologies RT66A experimental setup with high voltage amplifier was utilized. These measurements were done at low frequency (1 Hz) and high fields, up to 100 kV/cm. All high voltage measurements were done in a well-insulated sample cell with copper plug contacts and submerged in silicone oil to limit dielectric breakdown. To allow for strain measurements, the top copper contact was in floating contact with the sample, and the back was polished to a planar mirror finish to allow for optical reflectance. Strain measurements were done at 0.1 Hz with an optical interferometric sensor developed by MTI instruments (2100 Fotonic Sensor) measuring deflection of a reflected light beam due to movement of the floating copper contact. All strain and polarization measurements were done with a three-scan running average.

2.7 References

[1] R. Zhang and P. Taskinen, “A phase equilibria study and thermodynamic assessment of the BaO–Al2O3 system,” *Calphad*, vol. 51, pp. 42–50, Dec. 2015.

[2] W. C. Röntgen, “On a new kind of rays,” *Science (80-.).*, vol. 3, no. 59, pp. 227–231, 1896.

[3] T. Young, "II. The Bakerian Lecture. On the theory of light and colours," *Philos. Trans. R. Soc. London*, vol. 92, pp. 12–48, Dec. 1802.

[4] W. H. Bragg and W. L. Bragg, "The Reflection of X-rays by Crystals," *Proc. R. Soc. London. Ser. A, Contain. Pap. a Math. Phys. Character*, vol. 88, no. 605, pp. 428–438, Jul. 1913.

[5] H. M. Rietveld, "The Rietveld method," *Phys. Scr.*, vol. 89, no. 9, p. 098002, Sep. 2014.

[6] A. A. Coelho, "Whole-profile structure solution from powder diffraction data using simulated annealing," *J. Appl. Crystallogr.*, vol. 33, no. 3, pp. 899–908, Jun. 2000.

[7] D. C. Joy, "The theory and practice of high-resolution scanning electron microscopy," *Ultramicroscopy*, vol. 37, no. 1–4, pp. 216–233, Aug. 1991.

[8] "ProboStat^{TM} Manual."

[9] "A-Tech Systems." [Online]. Available: https://www.atech-systems.com/probostat.html.

[10] "ProboStat Versatile High Temperature Test Fixture - Maranata-Madrid SL - NIF B-85746204." [Online]. Available: https://www.alphaomega-electronics.com/en/norecs/2256-probostat-accesorio-de-prueba-versatil-de-alta-temperatura.html.

Chapter 3

Dielectric Properties of x $BiInO_3$ – (1-x) $Pb(Zr_{0.52}Ti_{0.48})O_3$ Solid Solutions

Jason Nikkel, Ryan McQuade, David Cann and Michelle Dolgos

Published in IEEE – Transactions on Ultrasonics, Ferroelectrics, and Transducers

November 3rd, 2020 – TUFFC – 10533 – 2020; DOI: 10.1109/tuffc.2020.3036366

3.1 ABSTRACT

This study focused on the synthesis and electrical property measurements of the lead zirconate titanate (PZT)-bismuth indate (BI) perovskite solid solution system. As the PZT binary system is a very well-developed and integrated materials system, identifying new ternary systems based off of PZT would allow for a new dimension of control into the exploration and improvement of its electrical properties which could enable enhancements in the performance of current technology and devices. Here, the solid solution of $BiInO_3$ – $PbZrO_3$ – $PbTiO_3$ (x BI – (1-x) PZT 52/48) was explored. Through calcination studies, stable solid solutions were obtained and compositions up to a maximum of 15 mol% BI were synthesized. With increasing BI content, the symmetry transitioned from a tetragonal P4mm phase towards a rhombohedral R3m phase. The Curie temperature of these samples decreased with increasing mol% BI from ~390°C in pure PZT 52/48 to 322°C in 10% BI. Ferroelectric and piezoelectric studies of the 2.5% BI sample showed a coercive field of 14.4 kV/cm, a $P_{max} = 38\ \mu C/cm^2$, $P_r = 29\ \mu C/cm^2$, and a $d_{33}^* = 280$ pC/N under a maximum applied field of 70 kV/cm at 1 Hz.

3.2 Introduction

Lead zirconate titanate (PZT) has long been the industry standard materials system for ferroelectric and piezoelectric applications, as it can easily be compositionally tuned to obtain a wide variety of properties. It can be enhanced by exploiting its morphotropic phase boundary (MPB) at the Zr/Ti ratio = 52/48 [1], which enables its use in various devices such as microelectromechanical machines (MEMS), ferroelectric random access memory, and integrated piezoelectric sensors/actuators (pressure, gas and/or accelerometer

[2]). This MPB is often described as a compositionally dependent phase boundary where the free energies of two crystalline phases (tetragonal P4mm and rhombohedral R3m in the case of PZT as seen in **Fig. 3.1**) are exactly equal [3]. Perovskite solid solutions also can display mixed phase behavior where crystallographic free energies are similar enough to coexist due to variations in lattice enthalpy that arise from defects [4]. These two phenomena are generally observed and characterized by tracking the phase equilibria in the system. Therefore, identifying new dimensions for exploration into the PZT system through changing the phase equilibria across varying compositions could allow for new ways to control and modify materials properties.

In current practice, modifying PZT to achieve desired properties is most commonly achieved by single cation doping of the A or B site in the PZT perovskite [5]. This results in ‘hard’ PZT when doped with an acceptor cation, such as K^+ (A-site) or Fe^{3+} (B-site), and ‘soft’ PZT when doped with a donor cation, such as La^{3+} (A-site) or Nb^{5+} (B-site). Hard and soft PZT display different properties, and therefore are each useful in specific applications. For example, soft PZT is characterized by low coercive fields and high dielectric constants which lends itself well to FRAM and passive sensor applications, while hard PZT is characterized by more stable domain structures with higher electromechanical coupling coefficients and mechanical quality factors and are therefore used in actuator and MEMS applications [6]. While these methods are generally effective, they can be limited by the number of possible dopant cations and low solubility into PZT. Another avenue to modify PZT is through addition of a tertiary phase to the solid solution. This allows for higher solubility limits, modification of both the A and B sites simultaneously, and provides another dimension in controlling the phase equilibria of the system.

Additionally, as the processing and incorporation of PZT into silicon-based technologies has long been established, the infrastructure for developing PZT based devices is well integrated into current manufacturing technologies. Consequentially, it would be greatly beneficial to develop new solid solutions based on PZT that require minimal changes to overall processing methods. The addition of a tertiary phase to the PZT solid solution would allow for new avenues in engineering the properties of PZT-based piezoelectric materials. As previous research has shown, successful modifications and solid solutions of PT with Bi-based perovskite additions. For example, despite limited solubility, an increase in Curie temperature was observed in PT with the addition of $BiInO_3$ and $BiYbO_3$ [7]–[9]. The addition of Bi-based perovskites to PZT could be a very promising direction of research, and it is believed that focusing on the MPB region of PZT (52/48) with incremental additions of the tertiary Bi-based phase will produce the highest possibility for defining the solubility limit of the novel ternary while observing the effect of the newly incorporated perovskite on the phase equilibria of the parent PZT composition.

Little research has been performed on Bi-based solid solutions with PZT, where the prior literature investigates $Bi(Mg,Ti)O_3$ (BMT) modified PZT [10], $BiFeO_3$ (BF) – PZT [11], $BiMnO_3$ (BM) – PZT [12], and $Bi(Zn_{0.5}Ti_{0.5})O_3$ (BZT) – PZT [13]. These systems focused on analyzing the ferroelectric to paraelectric phase transition with the addition of the Bi-based perovskite modifying phase, and, from these studies, several general observations are of note. Primarily, there were observations of a tendency towards relaxor like behavior with increasing amount of the Bi containing phase, an increase in the thermal stability of the tetragonal phase for compositions with low phase fractions of PZ, and there were notable difficulties with solubility of the Bi containing phase with movement away from the MPB composition in the parent PZT system. Comparing these results to those observed in PT-BiMeO$_3$-based perovskite binary systems, the overall focus of this work was determined to investigate the effects of the addition to BiInO$_3$ into PZT to highlight the phase equilibria and electrical properties of PZT-BI based solid solutions.

3.2.1 Bismuth Indium Oxide

From the work of Belik et al., BiInO$_3$ forms under high temperature and high pressure in the polar space group Pna2$_1$, though, upon quenching to room temperature it takes on the more common GdFeO$_3$-type orthorhombic non-polar phase [14]. From this structure, no phase transition is observed at ambient pressure before the decomposition temperature; therefore, it is expected that it has a T_c above 600°C [14]. Given the limited stability of BI in the perovskite phase, synthesis of polycrystalline BI under ambient

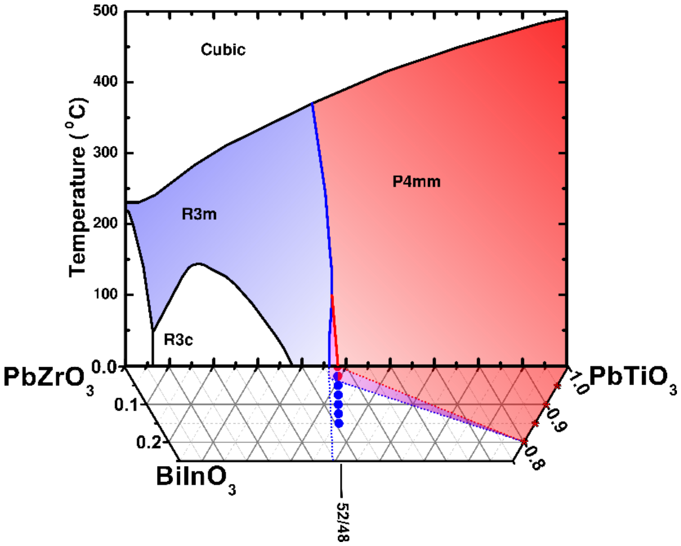

Figure 3.1: Extended phase diagram of the binary PbZrO$_3$ – PbTiO$_3$ recreated from Noheda et al. [16] into the ternary system BiInO$_3$ – PbZrO$_3$ – PbTiO$_3$. Phases of PbTiO$_3$ – BiInO$_3$ (red asterisks) determined by Duan et al. [8] and experimental data (red and blue circles) from room temperature x-ray diffraction of crushed sintered pellets. Ternary phase lines are purely hypothetical and are included to help guide the eye

conditions is not possible. However, recent studies into the origin of morphotropic behavior in materials may give evidence for its possible stabilization and solubility at standard temperature and pressure as part of a solid solution. It has been shown that pure $PbTiO_3$ exhibits morphotropic like behavior under high pressure, ~10 GPa, leading to the theory that MPB behavior is not solely a compositionally dependent phenomena and can be induced via various forms of pressure – i.e. chemical pressure due to large variation in chemical potential or induced crystal strain via competing free energies of crystalline phases [15]. While this has yet to be confirmed, it is possible that this effect could stabilize the high temperature-high pressure BI phase in MPB compositions of PZT.

3.3 Experimental

Samples in this work were synthesized via standard solid-state solution ceramics processing following the empirical formula $x\ BiInO_3 - (1-x)\ Pb(Zr_{0.52}Ti_{0.48})O_3$ for $x = 0 - 0.1$ in 0.025 increments. Solid state precursors of PbO (Alfa Aesar, 99.9%), Bi_2O_3 (STREM Chemicals, 99.999%), In_2O_3 (Alfa Aesar, 99.9%), ZrO_2 (STREM Chemicals, 99+%), TiO_2 (CERAC, 99.9%), were massed according to calculated stoichiometric ratios, mixed in an ethanol slurry, and combined with cylindrical yttria-stabilized ZrO_2 (YTZ) milling media at a ratio of 1.2 media per gram batched powder. The reagents were then milled for 10 hours on a Random-Orbital Vibratory mill (SWECO) to reduce particle size and homogenize the mixture. These milled solutions were then dried and calcined in covered alumina crucibles at 850°C for 2 hours in an open furnace (Carbolite) with a ramp rate of 5°C/min. Post-calcination, powders were pulverized to minimize agglomerates, and mixed again into a slurry with ethanol and YTZ media to further decrease particle size. To ensure that the desired phase was present, calcined samples underwent phase identification X-ray Diffraction measurements (Bragg Brentano, 0.02° step, DS: 1.125°, 2°/min) using a Rigaku Miniflex Cu K-alpha Diffractometer. After phase purity was confirmed, ~1.5 g of the milled, calcined powder was massed and mixed with 2 wt.% of Polyvinyl Butryal (PVB) solution and 2 mol% PbO excess to account for the volatility of PbO. The resultant powder was then uniaxially pressed at a pressure of 170 MPa in a 13 mm diameter cylindrical die (Carver Press). Green bodies were buried in sacrificial powder of the same composition, then sintered in covered alumina crucibles at 1100°C for 2 hours with a ramp rate of 3°C/min (a preliminary heating step of 450°C for 2 hours was incorporated to burnout organic PVB binder.)

It should be noted that, for all thermal treatments, powders and pellets were annealed in alumina crucibles that were aged and saturated with volatilized PbO, as opposed new, out of the box, crucibles. The use of virgin crucibles led to visible inhomogeneities in the sample, substantial cracking, density problems, and observable deposition of volatilized PbO on the walls of the crucible. The density of the sintered pellets was measured using Archimedes method and ensured to be >90 % theoretical density as determined by lattice parameters from Pawley fits. Various other compositions of this ternary were synthesized as calcined powders to explore the phase space but are not reported in this work as sintering conditions tended to vary extensively. XRD data supporting phase purity of these compositions can be found in Appendix A, and it was determined that the solubility limit for BI in PZT (52/48) was ~15% of BI content and ~10 mol% BI in PZT 50/50.

Phase purity of the samples was determined on crushed, sintered pellets using XRD (BB, DS:0.0625°, 0.02° step, 0.05°/min), with a Rigaku Miniflex Cu K-alpha benchtop diffractometer. For property measurements, the samples were polished to 0.5 mm thickness with a mirror finish. Silver electrodes were applied to the samples using a thermal silver paste (Heraeus) at room temperature, and then annealed at 700°C for 30 minutes. Prepared samples then underwent frequency (100 Hz to 1 MHz) and temperature (r.t. to 500°C) dependent dielectric permittivity characterization using a high temperature cell (NorECs AS ProbostatTM, Oslo, Norway) with capacitance measured using a Low Field Impedance Analyzer (HP 4192A) Room temperature polarization was measured at 1 Hz using a three scan running average (Radiant Technologies RT66A), and room temperature strain was measured concurrently at 0.1 Hz using an interferometric sensor (MTI Instruments 2100 Fotonic Sensor).

3.4 Results and Discussion

3.4.1 Density Measurements

The densities of samples reported in this work were confirmed to be ≥ 90 % theoretical density using the Archimedes method, with a minimum density of 90 %, maximum of 98 %, and average of 93.8 % varying by composition. Densities were also accompanied by shrinkage in the diameter of the samples of ≥ 10 %, with an average shrinkage of 11.4%, suggesting successful sintering of the samples. Theoretical densities were calculated using the volume of the parent structure, $Pb(Zr_{0.52}Ti_{0.48})O_3$, and a space group of P4mm, approximated by the splitting of the {100} reflection seen in the sample 0 % BI reported in **Fig. 3.2**. A stoichiometrically weighted average of the atomic masses for each constituent in the desired composition was then used to estimate a theoretical density at that composition.

3.4.2 Structural Studies of x BI (1-x) PZT 52/48

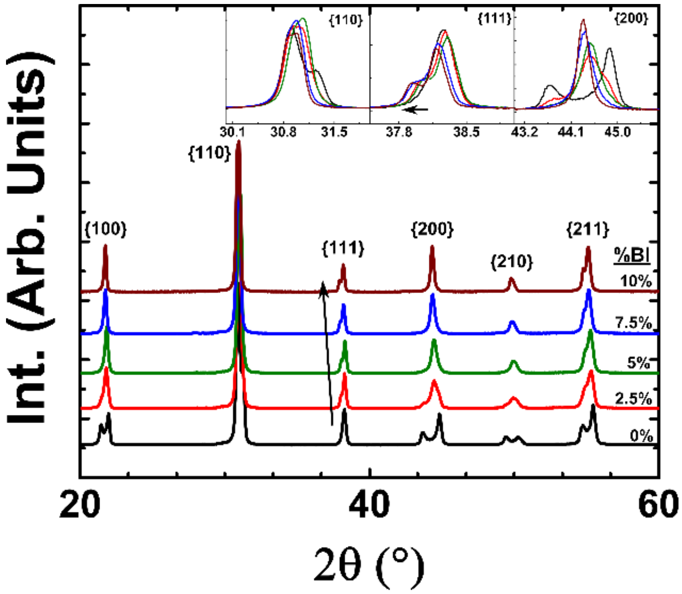

Figure 3.2: XRD data of pulverized dense ceramics with zoomed inserts showing evolution of rhombohedral phase character with increasing BI content. Tetragonal splitting can still be observed in the 2.5% BI sample. Asymmetry in peaks suggest some extent of phase mixing is present at room temperature for all samples except the 10% BI. Full structure intensity refinements, outside the scope of this work, would be necessary to confirm to any degree of quantitative certainty.

From first observations of **Fig. 3.2** a few key results were apparent. XRD results showed no impurity peaks with the lattice parameters changing as a function of composition, indicating a stable, phase pure, solid solution was formed. Also observed throughout these compositions are two distinct crystallographic phases, with apparent phase mixing of them in the 2.5% $BiInO_3$ composition. Qualitatively, these phases were identified from the characteristic splitting patterns as tetragonal and rhombohedral, given the strong splitting of the {200} at a 2:1 intensity ratio, and the evolution of the shoulder in the {111} (guide arrows in **Fig. 3.2**.) These phases are assumed to be the same as those of the parent MPB PZT composition. Note that the MPB PZT 52/48 composition is reported in literature as either of monoclinic symmetry [16], or of a phase mixture of tetragonal and rhombohedral. The 0 mol% BI (MPB PZT 52/48) sample from this work shows a phase mixture of tetragonal and rhombohedral, though with stronger tetragonal splitting, a c/a ratio of 1.022, than is typically present in the literature. This discrepancy from the literature was likely due to the use of excess PbO as a sintering aid, as XRD data of pre-sintered powders shows splitting patterns of mixed phase tetragonal and rhombohedral (included in Appendix A). It has been commonly seen that the use of excess PbO in PZT ceramics increases tetragonality through the preferential initial nucleation of $PbTiO_3$ [17]. As the use of excess PbO was a necessity for producing dense sintered ceramics due to the high volatility of PbO, more elaborate processing methods such as hot pressing, which is beyond the scope of this work, would be needed to inhibit the induced tetragonality.

Comparing the splitting patterns observed in **Fig. 3.2** to analogous bismuth modified PZT systems[10]–[13] a few general trends can be seen. Most apparently, while the onset of reduction in tetragonality in this BI modified system occurs more readily (i.e. BI-PZT(52/48) has fully transformed into the rhombohedral phase at 5 mol% addition of BI, whereas BZT-PZT(52/48) still shows tetragonal XRD character up to 20 mol% BZT [13],) there is a definite trend of a reduction in tetragonality with increasing amount of the $BiInO_3$ addition. With exception to the BF-PZT system, this typically corresponded to a decrease in the systems observed T_c. This is consistent with expected trends from phenomenological theory which predicts a temperature dependent decrease in spontaneous polarization while approaching T_c [18]. Further suggesting that the addition of a bismuth

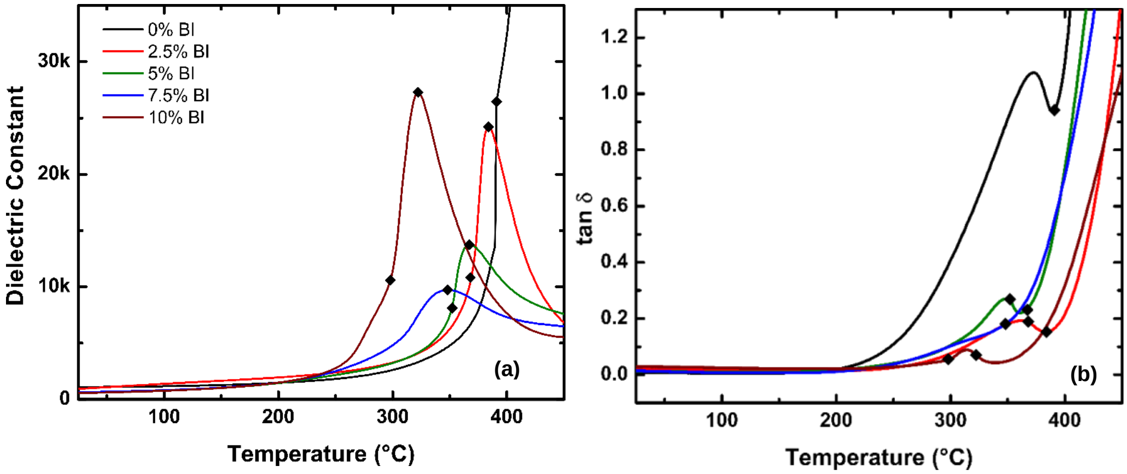

Figure 3.3: a) (left) Dielectric permittivity as a function of temperature and composition and b) (right) dissipation factor (tan δ) as a function of temperature and composition at 10 kHz showing a decrease in T_{max} as a function of increasing mol% BI, a trend from tetragonal character transition to rhombohedral character transition is observed. Diamond symbols refer to inflection points used to define data points in the phase diagram seen in **Fig. 3.5**.

compound to the PZT solid solution, overall, increases the stability of the PZ dominated rhombohedral phase. However, a similar study in the BF-PZT system reported an increase in T_c with increasing phase fraction of BF. This study was done at very low phase fractions of PZ, possibly suggesting that there exists a critical Zr/Ti ratio in bismuth modified PZT systems where the rhombohedral phase is suppressed. This would further correspond to a possible increase in T_c, as seen in the analogous B(M)-PT binaries [7], and would be of interest for further exploration into high T_c compositions of these bismuth modified PZT systems. Therefore, future studies within this system aimed for high T_c applications, a focus on the extrapolated mixed phase region at low PZ content seen in **Fig. 3.1** is highly suggested.

3.4.2 Dielectric Spectroscopy of x BI (1-x) PZT 52/48

Dielectric studies of these materials, seen in **Fig. 3.3 (a/b)**, and summarized in **Table 3.1**, clearly show that this system exhibits similar phenomena as BZT-PZT. A clear

Table 3.1
Summary of Properties for x $BiInO_3$ - (1-x) $Pb(Zr_{0.52}Ti_{0.48})O_3$
Dielectric @ 10 kHz; Ferroelectric @ 50 kV/cm

x $BiInO_3$ (%)	T_c (°C)	ε_r (T_c)	tan δ (T_c)	ε_r (r.t.)	tan δ (r.t.)	P_{max} (μC/cm^2)	P_r (+) (μC/cm^2)	E_c (+) (kV/cm)
0	390	26000	0.940	1070	0.008	24.0	11.6	13.9
2.5	380	24000	0.150	930	0.023	23.6	12.1	10.8
5	370	14000	0.230	620	0.012	21.4	11.5	14.1
7.5	350	9700	0.180	630	0.014	18.4	7.4	11.1
10	325	27000	0.070	550	0.029	22.0	11.9	11.7

decrease in T_{max}, with an accompanying maximum in *tan δ* suggests a constant decrease in T_c with increasing content of BI. This is consistent with, and supports, the theory that the additions of Bi-based perovskites to PZT stabilizes the PZ dominated R3m phase. This is also seen in the change in the character of the ferroelectric to paraelectric transition in the dielectric data, from a sharp peak at 0 mol% BI, very characteristic of a tetragonal to cubic transition, to a broader peak which could be more characteristic of a rhombohedral to cubic phase transition or the onset of a diffuse second-order phase transition. While the possibility of an induced relaxor phase is acknowledged (also evidenced by some frequency dispersion observed in all samples – an example of which is shown in **Fig. 3.4**,) the peak maxima did not shift in temperature at different measurement frequencies (typically less than 5-10°C, the accuracy of our temperature resolution)– suggesting a discrete phase transition. It should be noted that the composition with the highest BI content (10 mol% BI) exhibited two discrete phase transitions that do not fit into the observed trend in the data. While samples with increasing mol% BI show a clear trend in lowering in the absolute value of permittivity at T_{max} and broadening of the peak in the permittivity, the 10 mol% sample begins to exhibit a broad transition of lower permittivity (onset ~250°C in **Fig. 3.3 a**) then instantaneously increases in permittivity (onset ~300°C **Fig. 3.3 a**) into a sharp transition peak. This suggests that the 10 mol% sample (clearly rhombohedral at r.t.

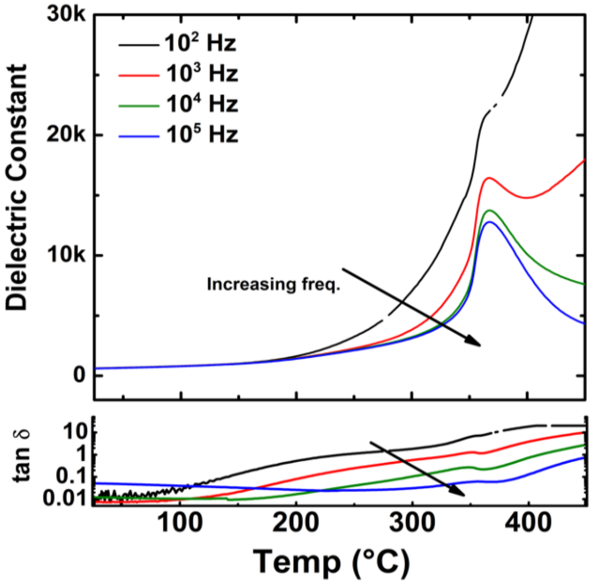

Figure 3.4: Representative frequency dependence of the dielectric response as a function of temperature for 5 mol% BI – PZT (52/48) from 100 Hz to 100 kHz exhibiting an extent of frequency dispersion prior to the transition temperature. A lack of dispersion in T_{max} suggests that the material still exhibits a discrete phase transition, while it may have some relaxor phase present contributing to the observed frequency dispersion

in **Fig. 3.2**) transitions from its rhombohedral phase into a tetragonal phase prior to its ultimate paraelectric phase transition. This is consistent with the phase evolution of the parent PZT system. Looking at the curvature in the phase line separating the PZT R3m phase from the PZT P4mm phase in **Fig. 3.1**, it is apparent that samples of lower PT content (between 42 mol% and 46 mol% PT) would cross this phase line prior to the cubic paraelectric phase transition. It is believed that the extrapolation of this phase line from the binary to the ternary phase diagram is accountable for this phenomenon.

It also should be noted the permittivity data in **Fig. 3.3** only shows measurements at 10 kHz, data over the entire frequency spectra for each composition showed that each sample exhibited some amount of frequency dispersion prior to the FE-PE transition. A representative plot showing this frequency dispersion can be seen in **Fig. 3.4** and full frequency spectra for all samples can be found in Appendix A2. From this figure we can

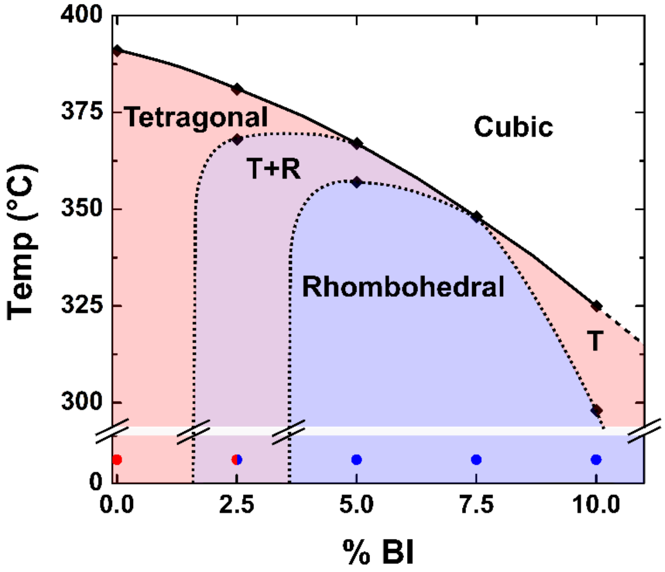

Figure 3.5: General phase diagram of x BI – (1-x) PZT 52/48 with respect to BI content. Circles represent phase ID from r.t. XRD data and diamonds represent and approximated points of interest from the experimental dielectric loss measured at 10^5 Hz. Dotted lines are hypothetical and generated to approximate the phase diagram.

see clear evidence of a frequency dispersion evolving with the addition of BI content, suggesting that the addition of BI to the PZT system induced some relaxor-like behavior, also in agreement with phenomena observed in PZT modified with Bi-based perovskite literature.

In analyzing these samples, apart from the 7.5 mol% BI composition, all compositions exhibit a dielectric phase transition of tetragonal character, suggesting that each exhibits a rhombohedral to tetragonal phase transition as the temperature approaches T_C. Through combining these results with room temperature XRD results in **Fig. 3.2** a general phase diagram with respect to BI content was generated and can be seen in **Fig. 3.5**. The reported transition temperatures were approximated from peaks in the dielectric loss. Colored dots represent the room temperature phase observed by XRD.

3.4.4 Ferroelectric and Piezoelectric Studies

Ferroelectric studies were also carried out on all compositions, unpoled, with a selected representative polarization loop of the 2.5 mol% BI composition shown in **Fig. 3.6**. Full polarization data for all compositions can be found in Appendix A. A subsequent three sample study of the piezoelectric strain in the representative 2.5 mol% BI composition was also completed, with the averaged results reported in **Fig. 3.6**. Full strain data for all three samples can also be found in Appendix A. All samples were able to withstand fields upwards of 100 kV/cm before breakdown. All samples exhibit a coercive field of ~20kV/cm and did not fully saturate until 40-50 kV/cm. The maximum polarization across all compositions ranged from 25 μC/cm^2 to 40 μC/cm^2 at a field of 70kV/cm. Strain maximums across all samples in the 2.5 mol% BI composition averaged around 0.2% at 70 kV/cm. The maximum strain in **Fig. 3.6**. is equivalent to a d_{33}^* of approximately 280 pC/N. These compare well to a similar system, researched for high temperature purposes, $BiScO_3$ modified $PbTiO_3$. The MPB of this system is reported to be at 37 mol% $BiScO_3$ and this

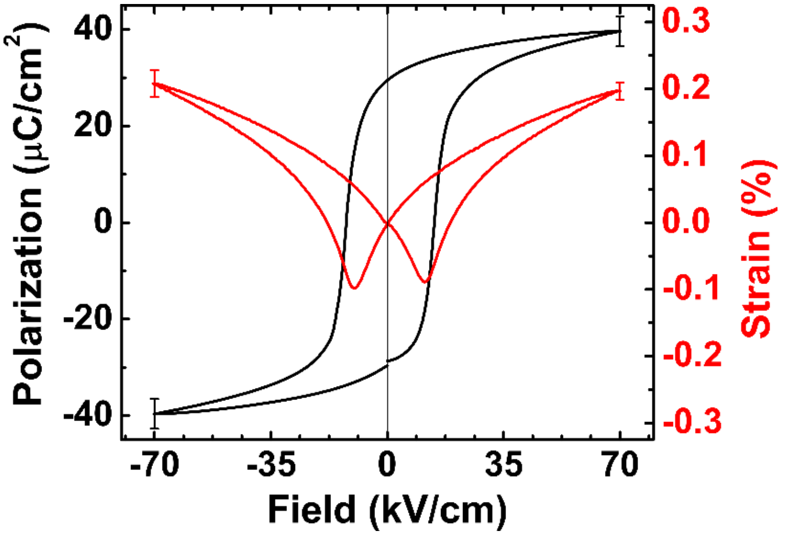

Figure 3.6: Hysteresis loops of 2.5 mol% BI – PZT 52/48 at a max field of 70 kV/cm and a frequency of 1 Hz. Error bars on P_{max} and S_{max} determined from standard deviation of identical runs on five separate samples.

Table 3.2

Comparison of Properties for Bismuth End–Member Modified – Lead Titanate or Lead Zirconate Titanate Compounds; Dielectric @ 10 kV/cm

Composition	d_{33} (pC/N)	d_{33}^* (pC/N)	T_c (°C)	ε (T_c)	tan δ (T_c)	ε (r.t.)	tan δ (r.t.)	Ref.
2.5% $BiInO_3$ - 97.5% $Pb(Zr_{0.52}Ti_{0.48})O_3$	---	~280 @ 70 kV/cm	380	24000	0.150	1080	0.028	*this work*
5% $Bi(Zn_{1/2}Ti_{1/2})O_3$ - 95% $Pb(Zr_{0.52}Ti_{0.48})O_3$	300	---	350	~21000	---	~1100	---	[13]
11% $BiMnO_3$ - 89% $Pb(Zr_{0.70}Ti_{0.30})O_3$	---	---	~347	~3000	---	~1000	---	[10]
64.8% $BiFeO_3$ - 35.2% $Pb(Zr_{0.151}Ti_{0.849})O_3$	64	---	560	~20000	>1	232	0.014	[11]
65% $Bi(Mg_{1/2}Ti_{1/2})O_3$ - 53% $Pb(Zr_{0.378}Ti_{0.622})O_3$	---	~650 @ 60kV/cm	~550	~3000	---	~1200	---	[12]
37% $BiScO_3$ - 63% $PbTiO_3$	208	~200 @ 50kV/cm	430	~21000	>1	~1000	~ 0.022	[20]
15% $BiInO_3$ - 85% $PbTiO_3$	---	---	590	~8700	>1	~250	~0.01	[9]

composition exhibits a maximum polarization of around 40 μC/cm^2, a coercive field of 14 kV/cm, and a maximum strain of 0.1% (corresponding to a d_{33}^* of approximately 200 pC/N with a maximum applied field of 50kV/cm [19]. The dielectric and ferroelectric properties discussed above for the 2.5% BI composition are summarized in **Table 3.2** in comparison to those of similar systems.

3.4 Conclusions

The phase equilibria of the Bi-based perovskite modified PZT ternary perovskite solid solution, x $BiInO_3$ – (1-x) $Pb(Zr_{0.52}Ti_{0.48})O_3$, was explored using x-ray diffraction and dielectric spectroscopy as a function of temperature. Through calcination studies, the solubility limit was determined to be ~15 mol% BI. From XRD data, with increasing phase fraction of BI, the system exhibited a tetragonal to rhombohedral compositionally dependent phase transition with a region of mixed phase stability at 2.5 mol% BI suggesting the possible existence of an MPB in the system. This phase evolution was further informed by dielectric measurements, where all compositions exhibited a sharp dielectric peak characteristic of a tetragonal to cubic phase transition, except for the 7.5 mol% composition. This suggests that a rhombohedral to tetragonal phase transition occurs prior to the cubic phase transition, which agrees with the curvature of the ferroelectric to paraelectric phase line in the parent PZT phase diagram. In agreement with other Bi-based perovskite modified PZT systems, as the BI mol% increased, the T_c was observed to decrease. This was observed along with an increase in the appearance of relaxor-like behavior. Ferroelectric measurements were carried out on 2.5 mol% BI samples with properties comparable to non-modified PZT 52/48 ceramics and the MPB composition of $BiScO_3$ modified $PbTiO_3$ [1], [19].

3.5 References

[1] B. Jaffe, W. R. Cook, and H. L. Jaffe, *Piezoelectric ceramics*. Academic Press, 1971.

[2] N. Izyumskaya, Y.-I. Alivov, S.-J. Cho, H. Morkoç, H. Lee, and Y.-S. Kang, "Processing, Structure, Properties, and Applications of PZT Thin Films," *Crit. Rev. Solid State Mater. Sci.*, vol. 32, no. 3–4, pp. 111–202, Dec. 2007.

[3] D. Damjanovic, "A morphotropic phase boundary system based on polarization rotation and polarization extension," *Appl. Phys. Lett.*, vol. 97, no. 6, p. 062906, Aug. 2010.

[4] W. Jo *et al.*, "Evolving morphotropic phase boundary in lead-free

(Bi1/2Na1/2)TiO3–BaTiO3 piezoceramics,” *J. Appl. Phys.*, vol. 109, no. 1, p. 014110, Jan. 2011.

[5] D. Damjanovic, “Ferroelectric, dielectric and piezoelectric properties of ferroelectric thin films and ceramics,” *Reports Prog. Phys.*, vol. 61, no. 9, pp. 1267–1324, 1998.

[6] M. Marsilius, K. G. Webber, E. Aulbach, and T. Granzow, “Comparison of the Temperature-Dependent Ferroelastic Behavior of Hard and Soft Lead Zirconate Titanate Ceramics,” *J. Am. Ceram. Soc.*, vol. 93, no. 9, pp. 2850–2856, Jun. 2010.

[7] R. E. Eitel, C. A. Randall, T. R. Shrout, P. W. Rehrig, W. Hackenberger, and S.-E. Park, “New High Temperature Morphotropic Phase Boundary Piezoelectrics Based on Bi (Me) O 3 – PbTiO 3 Ceramics,” *Jpn. J. Appl. Phys.*, vol. 40, no. 10, pp. 5999–6002, 2001.

[8] R. Duan, R. F. Speyer, E. Alberta, and T. R. Shrout, “High Curie temperature perovskite BiInO3–PbTiO3 ceramics,” *J. Mater. Res.*, vol. 19, no. 07, pp. 2185–2193, Jul. 2004.

[9] S. Zhang, R. Xia, C. A. Randall, T. R. Shrout, R. Duan, and R. F. Speyer, “Dielectric and Piezoelectric Properties of Niobium-modified BiInO3–PbTiO3 Perovskite Ceramics with High Curie Temperatures,” *J. Mater. Res.*, vol. 20, no. 08, pp. 2067–2071, Aug. 2005.

[10] J. Fu and R. Zuo, “Giant electrostrains accompanying the evolution of a relaxor behavior in Bi(Mg,Ti)O 3-PbZrO 3-PbTiO 3 ferroelectric ceramics,” 2013.

[11] W. Hu, X. Tan, and K. Rajan, “BiFeO3–PbZrO3–PbTiO3 ternary system for high Curie temperature piezoceramics,” *J. Eur. Ceram. Soc.*, vol. 31, no. 5, pp. 801–

807, May 2011.

[12] A. Molak *et al.*, “Electric features of PZT 70/30–BiMnO3 solid solution ceramics,” *J. Eur. Ceram. Soc.*, vol. 35, no. 9, pp. 2513–2522, Sep. 2015.

[13] S. C. Lee *et al.*, “Bi(Zn 0.5 Ti 0.5)O 3 substitution effects in Pb(Zr,Ti)O 3 piezoelectric ceramics around morphotropic phase boundary region,” *Ferroelectrics*, vol. 401, no. 1, pp. 181–185, Oct. 2010.

[14] A. a Belik, S. Y. Stefanovich, and B. I. Lazoryak, “BiInO 3 : A Polar Oxide with GdFeO 3 -Type Perovskite Structure,” *Chem. Mater*, vol. 18, no. 8, pp. 1964–1968, 2006.

[15] M. Ahart *et al.*, “Origin of morphotropic phase boundaries in ferroelectrics,” *Nature*, vol. 451, no. 7178, pp. 545–548, Jan. 2008.

[16] B. Noheda, J. Gonzalo, L. Cross, R. Guo, and S.-E. Park, “Tetragonal-to-monoclinic phase transition in a ferroelectric perovskite: The structure,” *Phys. Rev. B - Condens. Matter Mater. Phys.*, vol. 61, no. 13, pp. 8687–8695, Apr. 2000.

[17] M. Morozov, “Softening and Hardening Transitions in Ferroelectric Pb(Zr,Ti)O 3 Ceramics,” 2005.

[18] L. E. Cross, “Relaxor ferroelectrics,” *Ferroelectrics*, vol. 76, no. 1, pp. 241–267, Dec. 1987.

[19] A. Sehirlioglu, A. Sayir, and F. Dynys, “High temperature properties of BiScO3–PbTiO3 piezoelectric ceramics,” *J. Appl. Phys.*, vol. 106, no. 1, p. 014102, Jul. 2009.

Chapter 4

Report on a Potential High Permittivity, Temperature-Stable Material Based on Perovskite Ba,Ca(Zr,Ti)O_3 Relaxor Ferroelectric Ceramics

Jason Nikkel, Gregory Guymon, and David Cann

Manuscript Developed for Publishing in Applied Physics Letters –
Submission Pending

4.1 ABSTRACT

This work presents the experimental findings on the fabrication of a high permittivity relaxor ferroelectric solid solution based off the well-studied lead-free $(Ba,Ca)(Zr,Ti)O_3$ system. The composition 99% $Ba_{0.85}Ca_{0.15}(Zr_{0.10}Ti_{0.90})O_3$ – 1% $Bi(Zn_{1/2}Ti_{1/2})O_3$ was fabricated into ceramic embodiments via the mixed-oxides route to a theoretical density of ~96% by Archimedes density measurements. Structural analysis via XRD revealed the presence of a small volume fraction of inherent impurities, believed to be induced from Bi volatility during processing. Low temperature permittivity measurements show the sample to exhibit a relaxor-like frequency dispersion with an unexpected very high permittivity response with temperature stability. The temperature of maximum permittivity (T_{max}) is reported to be T_{max} = -19°C with a maximum permittivity of $\varepsilon_r = 36{,}600$ at 1 kHz corresponding to a dielectric loss of $tan\ \delta = 0.28$ with a temperature coefficient $\tau_\kappa = -2498$ ppm/κ between -55°C and 85°C. While the novel composition shows evidence of a space charge contribution to the permittivity (most notably in the relatively high loss values, the frequency dispersion continuing past the peak in the permittivity, and increasing $tan\ \delta$ under low applied fields,) the effects attributable to space charge is believed to be limited and are linked to the small amount of observed impurity phases in the XRD data. These results suggest that the $Ba_{0.85}Ca_{0.15}(Zr_{0.10}Ti_{0.90})O_3$ – $Bi(Zn_{1/2}Ti_{1/2})O_3$ system has great promise for the development of new high permittivity dielectric materials.

4.2 $Ba,Ca(Zr,Ti)O_3$ Solid Solutions

The relatively high permittivity ($\varepsilon_r \sim 15{,}000$), perovskite-based relaxor ferroelectric system $Ba,Ca(Zr,Ti)O_3$ was discovered in 1954 by McQuarrie *et al*. [1]. This system was first discovered for potential capacitor applications but did not receive much attention until the late 90’s and early 2000’s during the push for lead-free piezoelectric materials when it was shown to exhibit piezoelectric coefficients comparable to that of lead zirconate titanate (d_{33} BCZT ~ 620 pC/N) [2]. Since then, a large amount of research into this quaternary system for piezoelectric applications has occurred [2], [3], [4]–[11], [12]–[15], Throughout this body of work, the relatively high permittivity has been continually observed namely by [2], [9]–[11]. This body of work has also shown this system to have a compositionally dependent first-order Curie-transition ranging from ~ -25°C to +85°C, a very advantageous temperature range for capacitor applications whose working temperature ranges vary and range from -55°C to 150°C.

4.3 Temperature Dependence Considerations

The origination of this high permittivity is, in majority, due to the spontaneous onset of polarization accompanied by a paraelectric – ferroelectric first order transition [14]. Unfortunately, this enhancement to the permittivity is only accessible over a small temperature window at and around the Curie temperature (T_c). As the integral application of a capacitor requires the device to have a temperature stable capacitance value, high κ materials that rely on a paraelectric – ferroelectric transitions are disadvantaged. Historically, this hurdle has been approached with composite compositional phase mixtures in doped - $BaTiO_3$ systems [16], however this approach has multiple inherent issues that limit the extent of its use, inhomogeneity etc. Therefore, developing a methodology to modify high κ compositions of ferroelectric perovskites to expand the workable range of the dielectric response away from the Curie point would be very desirable.

4.3.1 Relaxor Ferroelectric Doping Scheme

In this work, such a methodology is hypothesized and experimentally explored through the application of the relaxor ferroelectric (RFE) paradigm. In relaxor ferroelectrics, chemical inhomogeneity is incorporated into the solid solution through substitution of dissimilar cations in the perovskite unit cell as discussed in Chapter 1. This chemical inhomogeneity is incorporated at a local (nanometer) scale through chemical disorder in the formation of polar nanoregions (PNRs) which are theorized to exist as either polar nano-regions in an inhomogeneous cubic matrix or ordered polar ferroelectric regions (domains) separated by cubic-like domain walls. While the mechanisms underpinning this paradigm are still up for debate, the formation of PNRs has been commonly observed and their existence has been confirmed via inelastic neutron scattering techniques. The effect of the RFE paradigm on a normal ferroelectric is drastic, as the polar unit in an RFE is the PNR, due to the presence of disorder there is no driving force for the formation of ferroelectric domains. Therefore, the permittivity response in an RFE is due primarily to the growth and mobility of PNRs as opposed to domain wall motion. Even more importantly, RFEs do not exhibit first order phase transitions from the high temperature paraelectric (PE) phase to the RFE phase. Instead, this transition is of second order, and its onset is defined by the Burns temperature, T_B. Below the Burns temperature a single Curie temperature is no longer observed. Instead, the materials permittivity response reflects a distribution of Curie temperatures which can be correlated to the size distribution of PNRs. This distribution is a Gaussian distribution and can be described as such:

$$\frac{\varepsilon'(max)}{\varepsilon'(f,T)} = \exp\left(\frac{\left(T - T_{max}(f)\right)^2}{2\delta^2}\right)$$

Where the factor δ is directly controlled through the solid solution of dissimilar cations. It is the assertion of this work that the formation of a solid solution between BCZT and small fractions of a perovskite endmember with significant chemical variance on both the *A* and *B* sites will induce a RFE phase, flattening out the permittivity response in temperature space through the above relationship. To achieve this, a desirable composition of BCZT from the literature was chosen, $Ba_{0.85}Ca_{0.15}(Zr_{0.1}Ti_{0.9})O_3$ (T_c = ~75°C, $\varepsilon_{r,Tc}$ = ~10,000) [10], [11] and modified with 1 mol % $Bi(Zn_{0.5}Ti_{0.5})O_3$ incorporating Bi and Zn on the *A* and *B* sites respectively whose chemical variances are summarized in **Table 4.1** as developed by *Shannon et al.* [17] and databased by the Atomistic Simulation Group [18].

Table 4.1

Summary of chemical variance between parent BCZT solid solution and $Bi(Zn_{1/2}Ti_{1/2})O_3$ end-member additions

	Bi*	% diff Ba	% diff Ca	Zn	% diff Zr	% diff Ti
r_{ion} (Å) [12CN‖6CN]	1.45	9.9	8.2	0.74	2.8	22.3
Electronegativity	1.8	80	80	1.6	23.1	14.3
Valency	3	50	50	2	100	100

*All ionic radii are as reported from Shannon radii [17] for correct coordination environment, Bi(III) 12-fold coordinate radii determined from linear extrapolation of 5,6, and 8 fold Shannon radii

4.4 Experimental Methods

Polycrystalline samples of the 99% $Ba_{0.85}Ca_{0.15}(Zr_{0.1}Ti_{0.9})O_3$ – 1% $Bi(Zn_{0.5}Ti_{0.5})O_3$ were synthesized via normal mixed oxides solid solution processing. Reagent powders of $BaCO_3$, $CaCO_3$, ZrO_2, TiO_2, Bi_2O_3, and ZnO were massed stoichiometrically and combined in a wet EtOH slurry through high energy vibratory milling. Note that $BaCO_3$ and $CaCO_3$, both highly hygroscopic, were maintained in a constant 120°C oven, and massed hot, to prevent massing errors due to hydration. Batched powders were calcined in air at 1100°C/4h with 5°C/min heating and cooling rates. After a secondary milling, two

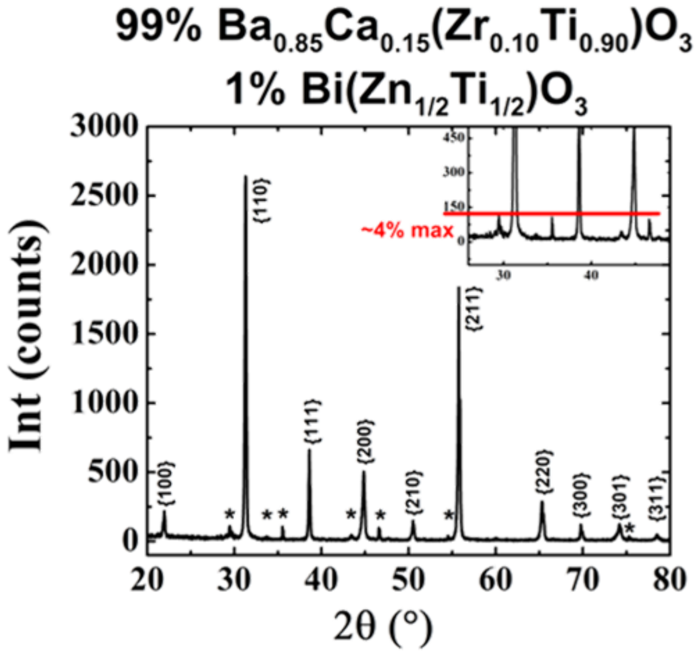

Figure 4.1: As-sintered, indexed, XRD of 99% $Ba_{0.85}Ca_{0.15}(Zr_{0.10}Ti_{0.90})O_3$ – 1% $Bi(Zn_{1/2}Ti_{1/2})O_3$ dense ceramic, peaks attributed to secondary phases are marked with an asterisk, zoomed insert is included to better observe main impurity peaks.

samples were fabricated through mixture of calcined powder with approximately 4 wt% polyvinyl-butyral binder, pressed in a 13mm die uniaxially under 170 MPa for 3 mins, covered in sacrificial powder of the same composition, and sintered in a cylindrical MgO crucible, in air, at 1400°C/4h with 3°C/min heating and cooling rates, with a 450°C/2h step for binder burnout. One sample exhibited characteristics of melting and was therefore ineffectual for property measurements. However, the other sample had no such imperfections and was found to be approximately 96% of the theoretical density using the Archimedes method, based off parent structure. X-ray diffraction (XRD) was utilized to determine phase purity of the samples. For dielectric characterization, electrodes were applied using silver thermal paint, and annealed at 750°C/30 mins. Low temperature dielectric spectroscopy was measured using an LCR meter in conjunction with a non-ambient liquid nitrogen cooled furnace. Low-field voltage dependence of the permittivity response was determined at room temperature in an impedance analyzer with a 1V oscillating voltage.

4.5 Considerations of Phase Purity

X-ray Diffraction analysis of the dense sample is reported in **Figure 4.1**. Upon first inspection a clear pseudo-cubic perovskite phase was observed and, in comparing the 2θ positions of the observed perovskite peaks to those observed in the reference paper [10], it was determined to be representative of the desired solid solution. Clear impurity peaks were observed as denoted by asterisk in **Figure 4.1**. Subsequent phase matching was inconclusive in their identification due to the number of observed impurity peaks throughout the pattern, and a densely packed group of impurity peaks around 29.8°. Phase matching was sufficient to determine several potential candidates. These were determined as $Ca_2Ba_2O_5$, ZrO_2, $TiZn_2O_4$, $(Zr,Ti)O_2$, and $Ba_2Bi_4Ti_5O_{18}$. Most plausible of these candidates are ZrO_2, $TiZn_2O_4$, $(Zr,Ti)O_2$ as Bi_2O_3 is well known to readily volatilize at very high temperatures due to its relatively low melting point (T_{melt} Bi_2O_3 = 817°C [19]). Any volatilization of Bi_2O_3 would lead to A-site stoichiometric deficiencies which then could drive the composition back to stoichiometric BCZT on the A-site, creating a driving force for the formation of compounds consisting of the excess B-site cations in the system. The A-site deficiencies could also be stabilized by oxygen vacancies, which could also lead to excess B-site cations in the system. It is suggested that, due to the very low level of doping, this system is very sensitive to both stoichiometries as well as processing conditions.

4.6 Low Temperature Permittivity Study

The electroded sample was then evaluated using low temperature dielectric spectroscopy as reported in **Figure 4.2**. A high permittivity was observed which was significantly larger than the results obtained for non-modified BCTZ in the literature (36,640 compared to 10,000 as reported at 1 kHz [11]). Furthermore, instead of exhibiting a typical first-order phase transition peak in the permittivity as observed in the literature, the sample exhibited a more diffuse phase transition, characteristic of relaxor ferroelectrics. This could account for the large disparity in the observed T_{max} for the sample, -19°C, as compared to the T_C observed in the non-modified BCZT composition of ~75°C. This suggests that the proposed doping scheme did indeed induce a relaxor ferroelectric phase in this system through the addition of BZT. Normally, in materials with transition from a normal ferroelectric material to a relaxor phase generally result in a loss to the permittivity, however in BCTZ-BZT it resulted in an increase in permittivity. It is therefore likely that a fraction of the observed permittivity response can be attributed to a space charge mechanism. In fact, looking closer at the high temperature regime in **Figure 4.2** there are clear signs of space charge as the permittivity drops with increasing frequency. This is supported by the relatively high loss in the sample with values of $\tan \delta$ hovering around 0.3. However, if most of the observed permittivity response was due to space charge mechanisms, much higher loss values would be expected, and therefore further investigation into this system is necessary.

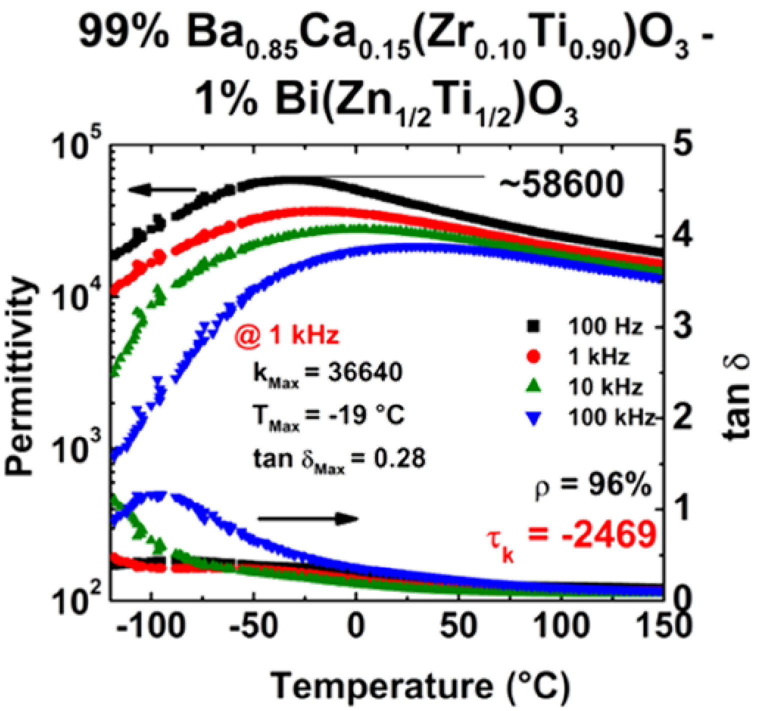

Figure 4.2: Low temperature dielectric spectroscopy of 96% of the theoretical density, 99% $Ba_{0.85}Ca_{0.15}(Zr_{0.10}Ti_{0.90})O_3$ – 1% $Bi(Zn_{1/2}Ti_{1/2})O_3$ ceramic showing frequency dispersion of the permittivity response characteristic of relaxor ferroelectrics at a very high permittivity magnitude ($\varepsilon_{r,Tmax}$ = 36640 @ 1kHz) with relatively high dielectric loss. Signs of space charge mechanisms are observed in frequency dispersion of the permittivity at high temperature (> T_{max}) and the relatively high range of the dielectric loss ($0.15 < tan\ \delta < 1$)

4.7 Voltage Dependence of the Dielectric Response

To further investigate the prevalence of space charge in this sample, the voltage dependence of the dielectric response was measured and is reported in **Figure 4.3**. As space charge mechanisms rely on energy barriers to inhibit electron mobility, the application of a voltage across the capacitor will quickly overcome these energy barriers and, if a materials permittivity is dependent on space charge mechanisms, a drastic increase to the loss will be observed. While experimentally limited by the voltage range on the recording instrument, fields up to ~ 1 kV/cm (corresponding to an applied voltage of 35V) were reached with a sample thickness of 0.511 mm. It can clearly be observed that, for

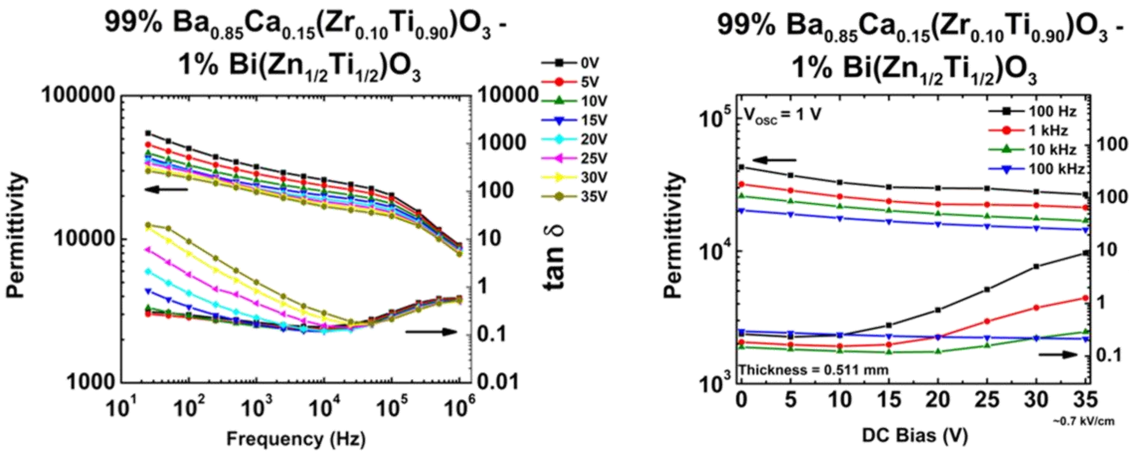

Figure 4.3: Voltage dependence of the dielectric response at room temperature for the high permittivity BCZT-BZT sample as a function of frequency (right) and applied DC bias (left).

frequencies less than 4x10^4 Hz, the application of voltage does incrementally increase *tan* δ in the sample. In fact, at 1 kHz, the value of *tan* δ increases with applied voltage approaching 1 until the application of 35 volts where *tan* $\delta > 1$. As loss values are above *tan* $\delta > 1$ it is reasonable to assume that loss currents dominate the dielectric response. This confirms that there is a definite portion of the permittivity response due to space charge, however the rate of increase in the loss was not as high as expected. As most capacitor applications operate at frequencies around 1 kHz with local fields of 10 kV/cm, this sample is clearly not suited for this application. However, it is believed that this composition is of great interest for future research and that understanding of, and improvements to, its processing conditions could limit the extent of impurity phase (and therefore limit the effects of space charge) while maintaining the desirable very high, temperature stable, permittivity response.

4.8 Conclusions

In summary, a novel relaxor ferroelectric composition was developed based on the Ba,Ca(Zr,Ti)O_3 solid solution. This composition is reported as 99% $Ba_{0.85}Ca_{0.15}(Zr_{0.10}Ti_{0.90})O_3$ – 1% $Bi(Zn_{1/2}Ti_{1/2})O_3$, and fabricated samples of this composition were determined to contain indeterminate secondary phases, suspected to be forms of B-site cation excess due to Bi_2O_3 volatilization. This was supported by the observance of $Ca_2Ba_2O_5$, ZrO_2, $TiZn_2O_4$, and $(Zr,Ti)O_2$ through peak matching with observed impurity peaks in the XRD. The sample was found to have an anomalously high permittivity response (ε_{max} = 36640 @ 1kHz) with a stable temperature dependence (τ_κ = -2498 ppm/κ for -55°C < T < 85°C). Frequency dispersion was observed in the low frequency regime, consistent with an induced relaxor ferroelectric phase through BZT doping. Frequency dispersion was also observed in the dielectric response at high temperature (post T_B) suggesting a contribution of space charge mechanisms to the observed permittivity. This was supported by the observation of respectively high loss values and an increase in the dielectric loss with the application of small fields (~ 1kV/cm). The existence of this space charge contribution was attributed to the existence of phase impurities in the sample, and it was suggested that further refinement of processing conditions, with careful attention paid to stoichiometry of volatile elements, could produce a viable high, temperature stable, permittivity material for capacitor applications.

4.9 References

[1] M. McQUARRIE and F. W. BEHNKE, “Structural and Dielectric Studies in the System (Ba, Ca) (Ti, Zr)O3,” *J. Am. Ceram. Soc.*, vol. 37, no. 11, pp. 539–543, Nov. 1954.

[2] P. Hansen, D. Hennings, and H. Schreinemacher, “Dielectric Properties of Acceptor-Doped (Ba,Ca)(Ti,Zr)O 3 Ceramics,” *J. Electroceramics*, vol. 2, no. 2, pp. 85–94, 1998.

[3] X. Liu *et al.*, “Enhancing piezoelectric properties of BCZT ceramics by Sr and Sn co-doping,” *J. Alloys Compd.*, vol. 640, pp. 128–133, Aug. 2015.

[4] D. Xue, Y. Zhou, H. Bao, J. Gao, C. Zhou, and X. Ren, “Large piezoelectric effect in Pb-free Ba(Ti,Sn)O $_3$ -x(Ba,Ca)TiO $_3$ ceramics,” *Appl. Phys. Lett.*, vol. 99, no. 12, p. 122901, Sep. 2011.

[5] Z. Yao *et al.*, “Titanium deficiency in tetragonal-structured (Ba,Ca)(Zr,Ti)O3 piezoelectric ceramics,” *J. Alloys Compd.*, vol. 712, pp. 406–411, Jul. 2017.

[6] J. Wu, A. Habibul, X. Cheng, X. Wang, and B. Zhang, “Orthorhombic–tetragonal phase coexistence and piezoelectric behavior in (1−x)(Ba,Ca)(Ti,Sn)O3–x(Ba,Ca)(Ti,Zr)O3 lead-free ceramics,” *Mater. Res. Bull.*, vol. 48, no. 10, pp. 4411–4414, Oct. 2013.

[7] S.-W. Zhang, H. Zhang, B.-P. Zhang, and G. Zhao, “Dielectric and piezoelectric properties of (Ba0.95Ca0.05)(Ti0.88Zr0.12)O3 ceramics sintered in a protective atmosphere,” *J. Eur. Ceram. Soc.*, vol. 29, no. 15, pp. 3235–3242, Dec. 2009.

[8] R. Hayati, M. A. Bahrevar, Y. Ganjkhanlou, V. Rojas, and J. Koruza, “Electromechanical properties of Ce-doped (Ba0.85Ca0.15)(Zr0.1Ti0.9)O3 lead-free piezoceramics,” *J. Adv. Ceram.*, vol. 8, no. 2, pp. 186–195, Jun. 2019.

[9] P. Hansen, D. Hennings, and H. Schreinemacher, “High-K Dielectric Ceramics from Donor/Acceptor-Codoped (Ba1−xCax)(Ti1-yZry)O3 (BCTZ),” *J. Am. Ceram. Soc.*, vol. 81, no. 5, pp. 1369–1373, Jan. 2005.

[10] N. Chaiyo, D. P. Cann, and N. Vittayakorn, “Lead-free (Ba,Ca)(Ti,Zr)O3 ceramics within the polymorphic phase region exhibiting large, fatigue-free piezoelectric strains,” *Mater. Des.*, vol. 133, pp. 109–121, Nov. 2017.

[11] N. Chaiyo, D. P. Cann, and N. Vittayakorn, “Phase transitions, ferroelectric, and piezoelectric properties of lead-free piezoelectric xBaZrO3–(0.25−x)CaTiO3–0.75BaTiO3 ceramics,” *J. Mater. Sci.*, vol. 50, no. 18, pp. 6171–6179, Sep. 2015.

[12] X. G. Tang, K.-H. Chew, J. Wang, and H. L. W. Chan, “Dielectric tunability of (Ba0.90Ca0.10)(Ti0.75Zr0.25)O3 ceramics,” *Appl. Phys. Lett.*, vol. 85, no. 6, pp. 991–993, Aug. 2004.

[13] Y. Bai *et al.*, “(Ba,Ca)(Zr,Ti)O3 lead-free piezoelectric ceramics—The critical role of processing on properties,” *J. Eur. Ceram. Soc.*, vol. 35, no. 13, pp. 3445–3456, Nov. 2015.

[14] M. Acosta *et al.*, “BaTiO $_3$ -based piezoelectrics: Fundamentals, current status, and perspectives,” *Appl. Phys. Rev.*, vol. 4, no. 4, p. 041305, Dec. 2017.

[15] Y. Tian, X. Chao, L. Jin, L. Wei, P. Liang, and Z. Yang, “Polymorphic structure evolution and large piezoelectric response of lead-free (Ba,Ca)(Zr,Ti)O $_3$ ceramics,” *Appl. Phys. Lett.*, vol. 104, no. 11, p. 112901, Mar. 2014.

[16] Bruchhaus, “US PATENT 6109191.”

[17] R. D. Shannon, C. T. Prewitt, and IUCr, “Revised values of effective ionic radii,” *Acta Crystallogr. Sect. B Struct. Crystallogr. Cryst. Chem.*, vol. 26, no. 7, pp. 1046–1048, Jul. 1970.

[18] Grimes Robin, “Database of Ionic Radii (Shannon Radii).” [Online]. Available: http://abulafia.mt.ic.ac.uk/shannon/ptable.php.

[19] “Bismuth Oxide | AMERICAN ELEMENTS ®.” [Online]. Available: https://www.americanelements.com/bismuth-oxide-1304-76-3.

Chapter 5

Experimental Studies on the Reproducibility and Processing Conditions of $Ba_{0.85}Ca_{0.15}(Zr_{0.10}Ti_{0.90})O_3$ Modified with 1% $Bi(Zn_{1/2}Ti_{1/2})O_3$

Jason Nikkel, Greg Guymon, Kyle Martin, and David Cann

Manuscript developed for publication in Journal of Applied Physics,
Submission Pending

5.1 ABSTRACT

Processing conditions giving rise to the unexpected temperature stable high permittivity response in observed 99% $Ba_{0.85}Ca_{0.15}(Zr_{0.10}Ti_{0.90})O_3$ – 1% $Bi(Zn_{1/2}Ti_{1/2})O_3$ were considered and investigated. Reproducibility studies successfully recreated the observed relaxor ferroelectric characteristics observed in the original sample, with similar secondary phases, though realizing only ~50% of the maximum permittivity magnitude given the maximum temperature at 1kHz. Stoichiometric deficiencies through bismuth volatilization were determined to be the driving force for secondary phase formation as secondary phases were mitigated through increasing the cooling rate from 2°C/min to 10°C/min and further diminished through the incorporation of 3 mol% Bi_2O_3 excess to the sacrificial powder. Single phase samples no longer exhibited the characteristics of the desired relaxor ferroelectric phase. Instead, they exhibited low permittivity responses (~2000), low dielectric losses (~0.015), with limited dielectric dispersion prior to the phase transition temperature.

5.2 Introduction

With the ever-increasing demand in telecommunications for faster data transfer rates and expanded device functionalities, there exists a constant push for developing new materials and devices to achieve these demands [1]. This has been realized in the current day through the development, and rollout, of 5G technologies, full surface phone displays, flexible and bendable displays, etc. These advancements, while innovative, continually diminish the circuit board space available within these devices for the necessary fundamental components that drive the device. Namely, as all smartphone devices contain thousands of multilayer ceramic capacitors (MLCCs) for full functionality, MLCCs are a necessary component for miniaturization. Not only are MLCC components of higher capacitance needed to sustain more elaborate functionalities in a smartphone device, but the space to integrate them has become more and more limited [2]. As the determinant variables for the capacitance of an MLCC are the thickness of the dielectric layer, the number of layers in the MLCC, and the permittivity of the dielectric layer, there are very few avenues available for improving the capacitance of an MLCC. With the number of layers in an MLCC being dependent on the physical form factor of the capacitor, the mechanical integrity of the ceramic/electrode interface, and the thickness of the dielectric layer, and the fact that the theoretical limit for dielectric layer thickness is currently being approached, normal device engineering approaches to increasing the MLCC capacitance while minimizing its form factor are no longer sufficient. Improving upon the inherent permittivity of the dielectric layer remains the only main avenue available to achieving these goals.

One other large complication exists further convoluting the problem. Capacitors in these devices must exhibit a stable capacitance value over a wide temperature range. As a materials permittivity is temperature dependent and exhibits maximum values at, and around, solid state phase transitions, developing a dielectric material of high permittivity that is stable over necessary temperature ranges remains a challenging prospect in both academia and industry.

Since their conception, MLCCs have utilized barium titanate [3], and composite forms thereof, for the dielectric layer. As a class II/III dielectric material of relatively high permittivity with phase transitions within most necessary temperature ranges, barium titanate has remained the material of choice in MLCC devices for decades. This is especially true due to its accessibility for manipulation into composites [4], [5], as it has been readily shown that the phase transition temperature can be shifted through small incorporations of either doping or oxygen vacancies. However, even with microstructure engineering to maintain the most desirable grain sizes and structures of these composites, their permittivity is not high enough to meet the current demands for miniaturization. Therefore, a necessity exists to research and develop high permittivity, temperature stable materials for MLCC applications.

As barium titanate-based solid solutions have garnered lots of attention over the past decade for lead-free piezoelectric alternatives to lead zirconate titanate [6], coincidentally these solid solutions were seen to exhibit very large permittivity responses , with advantageous Curie temperatures. One important example of such a solid solution is the semi-quaternary $BaTiO_3$ – $BaZrO_3$ – $CaTiO_3$ – ($CaZrO_3$) [7], hereby to be referred to as BCZT. This solid solution was shown to exhibit large relative permittivities, $\varepsilon_r > 10{,}000$ [8], [9], with a compositionally dependent Curie temperature $T_c < 100°C$. However, as already noted, these compositions were developed due to their desirable piezoelectric properties with piezoelectric coefficients, d_{33}^*, on the order of 500 pC/N. Any form of piezoelectricity is incompatible for MLCC applications as it could lead to delamination of the dielectric layer from electrodes and eventually to complete device failure. Therefore, forming composites of these compositions to take advantage of their compositionally driven Curie temperatures is more, or less, out of the question for MLCC applications. However, another possible avenue to develop temperature stability in these compositions as well as hopefully prevent inherent piezoelectricity would be to break up the ferroelectric domain structures through introduction of a relaxor ferroelectric phase [10]. In fact, in Chapter 4, a chosen composition of BCZT ($Ba_{0.85}Ca_{0.15}(Zr_{0.10}Ti_{0.90})O_3$) was modified with 1 mol% of $Bi(Zn_{1/2}/Ti_{1/2})O_3$ successfully inducing relaxor ferroelectric characteristics. While the resultant solid solution was not single phase, a relaxor ferroelectric phase was induced, and the material exhibited an excellent permittivity response over a wide temperature range. Note that, as the material was not single phase, the possibility exists that the observed relaxor characteristics could be due to defect-dipoles, not ferroelectric polar nanoregions. It was further reported that some portion of the permittivity response was observed to be due to inherent space charge mechanisms, however it was suggested that this space charge contribution was limited due to the high loss ($tan\ \delta \sim 0.3$) and was due to the limited existence of impurity phases observed via X-ray diffraction (XRD).

The goal of the present study is to better understand the very desirable permittivity response observed over a wide temperature range through the minimization, or elimination, of the observed impurity phase observed in the preliminary work. This would be accomplished through an experimental processing study to refine the processing parameters for this composition. Initially, a reproducibility study is preformed to ensure that the original published work was reliable and reproduceable, followed by subsequent processing studies looking at the effects of sintering temperature, post-sintering cooling rate, and incorporation of Bi_2O_3 excess. The motivation for this study was based on the hypothesis that the driving force for impurity phase formation was Bi volatilization during the sintering temp as Bi_2O_3 has a relatively high vapor pressure [11] combined with a low melting temperature of 817°C [12]. Finally, to develop a better overall understanding of the permittivity response of this system, microstructural studies were undertaken using scanning electron microscopy (SEM).

5.3 Experimental Procedure

Samples of $Ba_{0.8495}Ca_{0.1495}Bi_{0.01}(Zn_{0.005}Zr_{0.099}Ti_{0.896})O_3$ (BCZT-BZT) were fabricated using the normal mixed oxides route. Reagent powders of $BaCO_3$ (Alfa Aesar, 99.8%), $CaCO_3$ (Fisher, 99+%), Bi_2O_3 (STREM, 99.999%), ZnO (Alfa Aesar, 99.9%), ZrO_2 (STREM, 99+%), and TiO_2 (CERAC, 99.9%) were analytically massed and combined into a slurry with 80 vol% ethanol (EtOH) and yttria stabilized zirconia (YTZ) milling media at a ratio of 1.2 media/gram powder. Note that $BaCO_3$ and $CaCO_3$ reagents were kept dry in a 120°C oven to prevent massing error due to hydration. Prepared slurries were milled for 6 hours on a random orbital vibratory mill (SWECO), dried, and added as loose powder to a magnesia (MgO) crucible for calcination. Batched powders were then calcined at 1100°C/4h with a 5°C/min heating and cooling rate, collected, and again prepared into a wet ceramic slurry with EtOH and YTZ milling media. The slurry of calcined BCZT-BZT was milled again for 6 hours to minimize particle agglomerates and minimize grain size, dried, and collected for sample preparation. Milled, calcined powder was then massed to ~0.5 grams per sample and mixed with 4 wt% polyvinyl butyral binder (PVB, Butvar B-98, Aldrich). Samples were then pressed uniaxially in a 13mm die press at 170MPa for 3 mins and placed in an MgO crucible on a bed of sacrificial, calcined, powder. Samples were further covered with sacrificial powder and finally the covered crucible was placed in a high temperature furnace for sintering. For samples with incorporated Bi-excess, 3 mol% Bi was added to 0.5000 grams of sacrificial calcined powder which was then used to surround the pressed stoichiometric pellets. Prepared green body samples were then sintered according to desired parameters per experiment. All sintering profiles include a 450°C/2h step to allow for binder burnout. Samples of the reproduced study were sintered at 1400°C/4h with 2°C/min heating and cooling rates with 5 samples per crucible. Samples for the sintering temperature study were sintered one sample per crucible from 1350°C to 1400°C, with a 10°C interval, with a 4-hour dwell and 2°C/min heating and cooling rates. Another batch of 5 samples were sintered at 1350°C/4h with identical parameters in comparison to the 5-sample batch in the reproducibility study. Samples for the cooling rate and Bi-excess studies were sintered at 1400°C/4h with a 2°C/min heating rate and 10°C/min cooling rate. To prepare selected samples for SEM studies, samples were cleaved to expose a fresh fracture surface followed by a thermal etch at 1300°C/2h to highlight the grain boundaries.

Density of the fabricated ceramics was determined using the Archimedes principle and compared to the theoretical crystallographic density to determine a % theoretical density. Bragg-Brentano X-ray diffraction (Bruker D-8 Discover) on polished surfaces of dense sintered ceramics was utilized for phase analysis. Low temperature dielectric spectroscopy was accomplished using an LCR meter (Agilent 4284A) in tandem with a liquid N_2 fed low temperature box furnace (Delta Designs 9023) with temperature passively recorded via a temperature controller (Omega Platinum Series). Labview software was utilized to facilitate communication between experimental hardware and allow for continuous data collection. Scanning electron microscopy studies were done at the Oregon State University Electron Microscopy Facility with an FEI Quanta 600FEG environmental SEM.

5.4 Results and Discussion

Due to the extreme sensitivity to processing conditions found in the initial fabrication of the 1% $Bi(Zn_{1/2}Ti_{1/2})O_3$ modified $Ba_{0.85}Ca_{0.15}(Zr_{0.90}Ti_{0.10})O_3$ samples, this work presents three main research objectives to elucidate the effect processing parameters on the formation of this material. First, it will present the reproducibility of the initially reported sample in chapter 4 and show sample-to-sample variations between batches of five-samples prepared coincidentally with varied processing parameters. Second, it will present the effects of subtle changes in processing conditions for samples prepared individually. Together, this work demonstrates the extreme sensitivity to processing conditions for this material and aims to elucidate pathways for its development as a desirable material for multilayer ceramic capacitor applications.

5.4.1 Reproducibility Study of BCZT-BZT

To evaluate the accuracy of the originally reported data in chapter 4, a reproducibility study was performed. Five samples of the same composition BCZT-BZT were fabricated, in a single crucible, under the exact same sintering conditions as reported in chapter 4. All samples were determined to be ~94% dense, and XRD patterns of three representative reproduced samples can be observed in **Figure 5.1**. Upon inspection, it is clearly observable that the recreated samples also contain small amounts of impurity phases. However, it is quite clear that the observed impurity peaks in the reproduced sample differ significantly from that in the initially reported samples. In the initial samples, sharp impurity peaks are observable at various degrees 2θ (29.48°, 35.52°, 43.38°, 46.58°, and 54.51°). Phase identification through peak matching did not provide substantial evidence to conclusively identify these impurity phases, though they were determined to possibly be $Ca_2Ba_2O_5$, ZrO_2, $TiZn_2O_4$, $(Zr,Ti)O_2$, and/or $Ba_2Bi_4Ti_5O_{18}$. Main impurity peaks observed in the reproduced samples are compiled as a percentage of the maximum perovskite peak in **Table 5.1**. In comparison to the initial samples from chapter 4, they exhibit a lesser extent of impurity peaks, and do not exhibit the more intense impurity peak at 29.48° 2θ. However, they do still exhibit various impurity peaks at or around 29.5° 2θ with a maximum percentage of 2.8% as compared to 5.9% in the initial samples from chapter 4.

As the only difference between the reproduced samples and the initial samples was the number of samples in the crucible, this suggests that chemical gradients in the crucible environment during sintering are responsible for this discrepancy. It is possible that they may play an important role in determining which impurities are present. This was further

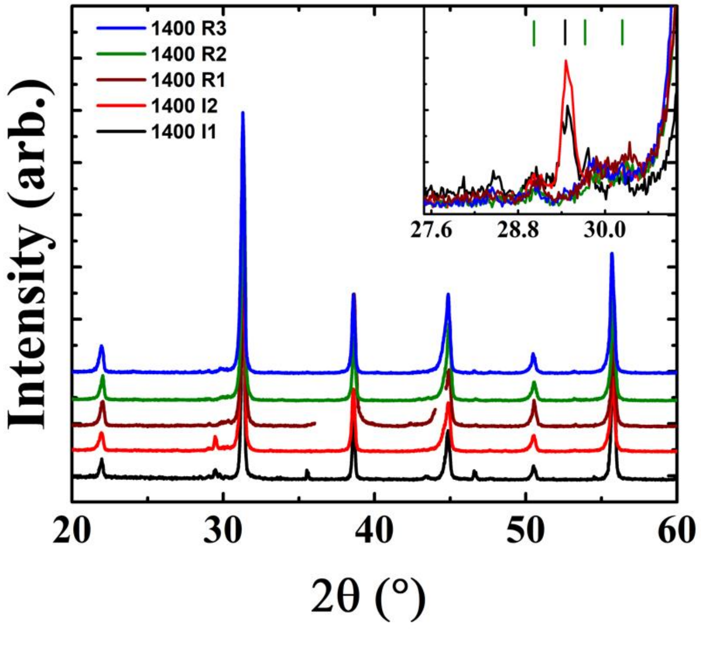

Figure 5.1: X-ray diffraction patterns of reproduced (R) BCZT – 1% BZT samples sintered at 1400°C/4h with patterns of initially fabricated (I) samples for comparison. Data missing in 1400 R1 is due to incident scattering off metal sample holder and was removed for clarity. Index drop lines on insert show peaks common to reproduced samples (green) and only initial samples (black).

Table 5.1

Summary of impurity peaks in 1% BZT modified BCZT solid solutions of reproduced (R) and initial (I) samples sintered at 1400°C/4h as a percentage of the maximum intensity of the main perovskite peak

Sintering Temp (°C)	**2θ of Impurity Peak (°)**								
	24.2	26.9	28.5	29.1	29.5	29.8	30.0	30.2	30.3
1400I1			1.7%	1.8%	4.2%	2.5%		1.5%	
1400I2		0.9%		1.8%	5.9%	2.1%	2.1%	2.2%	
1400R1	1.0%	0.8%	1.0%	1.3%		1.9%		2.0%	2.0%
1400R2	1.1%		1.0%	1.5%		2.2%			2.8%
1400R3	1.0%		1.0%	1.0%		1.8%		2.0%	2.0%

supported in high consistency between observed impurity peaks and their percentage in XRD patterns of the reproduced samples as seen in **Table 5.1**. To account for this, in further studies, only one sample will be sintered per crucible. For the sintering temperature study, a five-sample batch of the lowest sintering temperature will be done for comparison to the reproducibility study.

Low temperature permittivity data for the reproduced samples can be found in **Figure 5.2** with comparison to the initially reported data in chapter 4. In comparing the dielectric response of the reproduced samples to the initially reported data, the same high permittivity over a large temperature range with induced relaxor behavior phenomenon has been successfully reproduced. However, the permittivity magnitude of the reproduced samples is seen to be 47% lower than that of the initially reported sample (ε_r = 19300 @ T_{max} = -25°C, ε_r ~36600 @ T_{max} = -19°C for 1 kHz respectively,) which also corresponds to a 55% reduction in the observed loss ($tan\ \delta$ = 0.127 @ T_{max}, $tan\ \delta$ = 0.28 @ T_{max} respectively.) Also note that the observed frequency dependence of the dielectric response

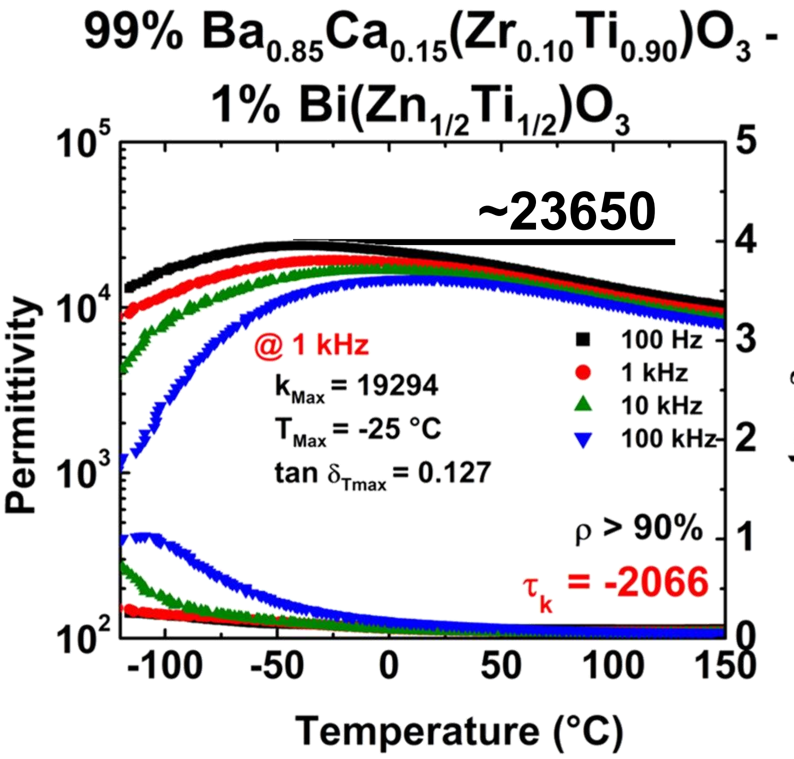

Figure 5.2: Low temperature dielectric spectroscopy for a representative reproduced BCZT – 1% BZT sample

in the high temperature regime ($T > T_{max}$) in the initial sample was still observed in the reproduced samples, though to a lesser degree. These results suggest that the observed impurity phase with a sharp peak at 29.48° 2θ was responsible for a large fraction of the loss, and therefore, the resultant inherent space charge mechanisms. In fact, upon closer inspection of the room temperature frequency dependence of the dielectric response, reported in **Figure 5.3**, the reproduced samples loss and permittivity values seem to be independent of frequency, whereas the initial sample was largely frequency dependent.

These results suggest that the initially reported data was not anomalous, that the addition of 1 mol% $Bi(Zn_{1/2}Ti_{1/2})O_3$ to BCZT induces a relaxor ferroelectric phase that exhibits a very desirable high permittivity over a wide temperature range. It also suggests that the magnitude of the observed permittivity response and its corresponding loss are

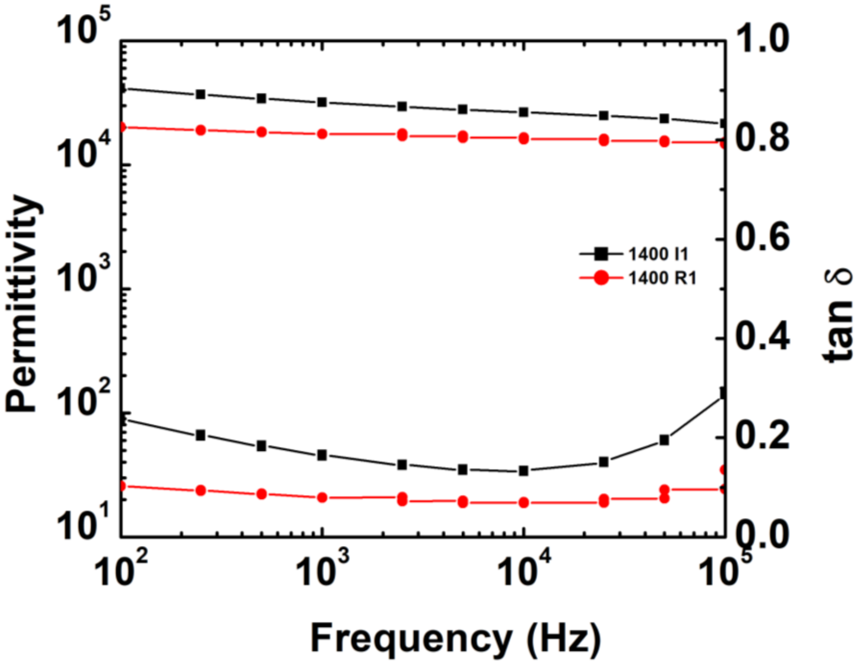

Figure 5.3: Room temperature dielectric properties as a function of temperature for a representative reproduced BCZT – 1% BZT (R1) sample with comparison to that of the initial (I1) sample as reported in chapter 4.

very sensitive to the existence of secondary, or impurity, phases, and that these impurity phases are very sensitive to processing parameters and the chemical environment within the sintering crucible.

5.4.2 Sintering Temperature Study of BCZT-BZT

To further refine the processing parameters for this system, and better understand the formation of secondary phases during sintering, a systematic study of the effects of the sintering temperature was performed. For the samples in this study, following the findings from the previous section, the samples were sintered individually in their own crucible at temperatures from 1350°C to 1390°C at 10°C intervals. Furthermore, for comparison to the five-sample batch done in the reproducibility study, five samples were sintered simultaneously in the same crucible at 1350°C. All other sintering parameters remained

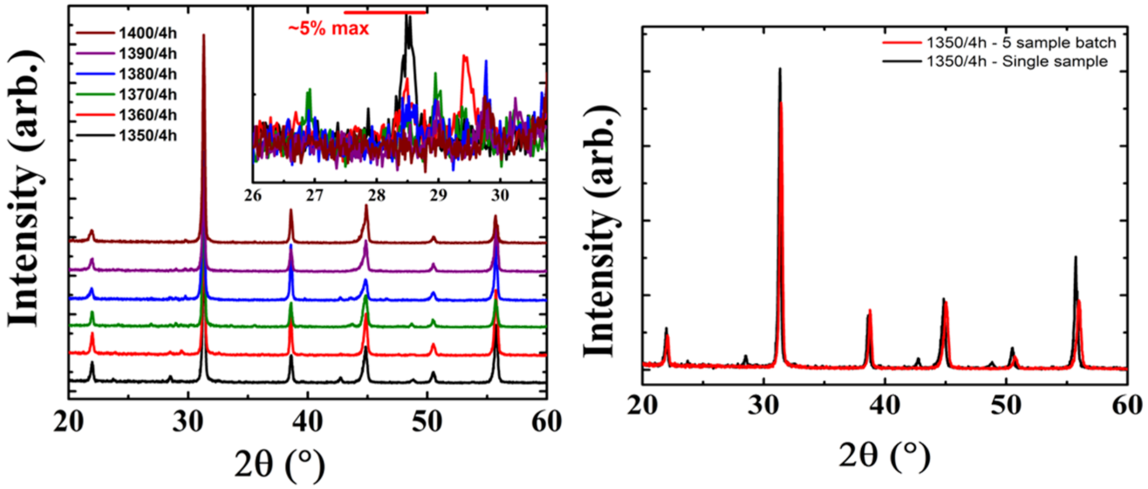

Figure 5.4: (a) XRD patterns of as-sintered BCZT – 1% BZT samples sintered individually between 1350°C and 1400°C and (b) XRD comparison of BCZT – 1% BZT sample sintered individually at 1350°C and a representative samples sintered in a five-sample batch at 1350°C.

fixed as defined in the experimental section. All samples were determined to be >90% theoretical density with an average density of 93% the theoretical. X-ray diffraction patterns of the dense ceramic samples are reported in **Figure 5.4a** with reference patterns included of the reproduced 1400°C samples.

From first inspection, no clear trend is observable in tracking the impurity peaks throughout the samples, though every sample does exhibit the desired perovskite phase and a variable amount of impurity peaks. Again, identification of the impurity peaks through 2θ matching was inconclusive though possible matches were again made for $Ca_2Ba_2O_5$, ZrO_2, $TiZn_2O_4$, and $(Zr,Ti)O_2$ in all samples. These reflections were tabulated for comparison in **Table 5.2**. It could be possible that some preferred orientation effects of the pellet further convolute the observed XRD patterns, and therefore powder scans of the crushed pellets would be necessary to develop more substantial conclusions. Furthermore, it is expected that the nature of XRD measurements on pellets has the potential to further convolute the data as it appears that there is some interchange in the morphology of the

Table 5.2

Summary of impurity peaks in 1% BZT modified BCZT solid solutions in sintering temperature study as a normalized percentage of the maximum intensity of the main perovskite peak, with reproduced (R) and initial (I) 1400°C samples for comparison. Shaded cells represent peaks common to samples of comparable permittivity, red – low, blue – medium, yellow – high

Sintering Temp (°C)	**2θ of Impurity Peak (°)**														
	23.7	24.2	26.9	27.9	28.5	28.9	29.4	29.8	30.2	32.6	33.6	35.5	42.7	46.6	47.6
1350	3.1%			2.1%	🟥 4.7%		🟥 1.8%						3.9%		
1360	🟦 2.9%				🟦 3.2%		4.0%			🟦 2.6%			1.7%		🟦 1.5%
1370		2.2%	2.5%		🟥 1.9%	2.9%	🟥 1.9%		1.9%	1.7%	1.7%	1.7%			1.1%
1380			2.1%		🟨 2.5%	2.4%		🟨 3.6%				🟨 1.2%	2.5%	🟨 1.7%	
1390	🟦 3.0%	2.8%			🟦 2.4%	3.4%		3.6%	3.6%	🟦 2.1%	1.9%	1.5%			🟦 1.0%
1400R								🟨 1.8%				🟨 1.0%			
1400I					🟨 1.7%		4.2%					🟨 4.0%		🟨 3.7%	0.9%

perovskite peaks, e.g. an onset of asymmetry to the peaks at 1380°C. This observed asymmetry in the peak shape could plausibly be due to inherent stress states in the pellet and/or preferred orientation. While it was not possible to do powder scans on these samples as they were needed for further low temperature dielectric spectroscopy, it is suggested that powder XRD of these samples would be needed to develop a better understanding of which impurity phases are present, as well as any structural differences in the perovskite phase due to a varied sintering temperature.

In comparison of the five-sample batch processed at 1350°C to the batch reproduced at 1400°C, in **Figure 5.4b** it is apparent that the representative sample from the 1350°C five-sample batch exhibited little to no impurities. The apparent purity of the 1350°C five-sample batch relative to the 1400°C was further accompanied by an

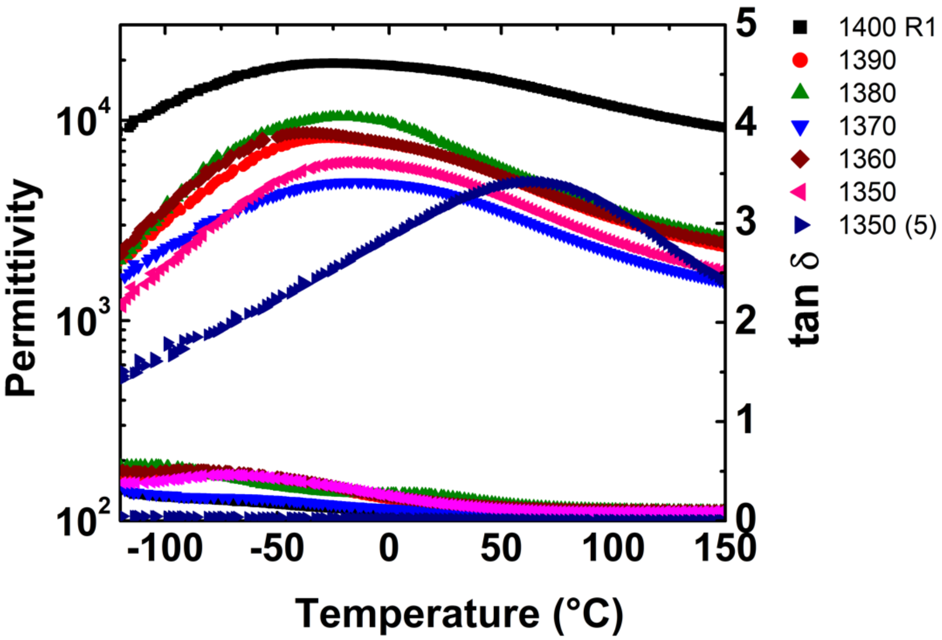

Figure 5.5: Low temperature dielectric spectroscopy for BCZT – 1% BZT samples sintered between 1350°C and 1400°C at 1kHz with comparison of a representative 1350°C five-sample batch (1350 (5))

observation of a color difference within the samples. All samples, insofar, exhibiting the high permittivity, temperature stable dielectric response were observed to be a dark-light metallic grey, whereas the samples from the 1350°C five-sample batch were observed to be a light-tan/ivory. As it is clearly observable in **Figure 5.4a** and **Table 5.2** that the 1350°C sample sintered individually had the largest extent of impurities (4.7% of max peak) this discrepancy further suggests that the composition is very sensitive to chemical environments in the crucible during sintering. However, it is acknowledged that this large discrepancy could plausibly be due to unknown experimental error, as uncontrollable environmental irregularities (short power outages, etc.) can interrupt and impact the temperature profile of a high temperature furnace or inhibit a programmed temperature controller from running the program to completion.

Low temperature dielectric spectroscopy a 1kHz for relevant samples to this study are compiled in **Figure 5.5**, and characteristic properties are listed in **Table 5.3** for ease of

Table 5.3
Summary of impurity peaks in 1% BZT modified BCZT solid solutions of reproduced (R) and initial (I) samples sintered at 1400°C/4h as a percentage of the maximum intensity of the main perovskite peak

Sintering Temp (°C)	**τ_k (ppm/ε_r)**	**$\varepsilon_{r,max}$**	**T_{max}**	**tan $\delta_{\varepsilon r,max}$**
1400°C/4h	-2066	19294	-25°C	0.127
1390°C/4h	-3430	8200	-27.5°C	0.335
1380°C/4h	-4464	10800	-25°C	0.285
1370°C/4h	-2680	4926	-17°C	0.15
1360°C/4h	-4503	8680	-34.6°C	0.39
1350°C/4h	-2276	6180	-18.1°C	0.321

comparison. Analysis of the results in **Figure 5.5** show that the desired relaxor phase is present in all samples with exception of the representative sample of the 1350°C five-sample batch. For samples with the observed desired relaxor phase, all previously noted characteristics are present, however the magnitude of the permittivity response greatly varies with no apparent trend. Plotting the maximum permittivities from **Table 5.3** as a function of sintering temperature as seen in **Figure 5.6** communicates this sporadic nature most effectively. These results further enforce the hypothesis that the high permittivity observed in this composition is very sensitive to stoichiometry and the presence of certain impurity phases. In fact, looking at the low temperature permittivity response of the representative 1350°C five-sample batch, we see the exemplified relaxor behavior diminished as well as the magnitude of the permittivity (ε_r = 4941, $\tan\delta$ = 0.012 @ T_{max} = 63°C), and a more normal insulative dielectric response for a ferroelectric material.

With the observed change in the visual nature of these samples which correlated to a more typical ferroelectric insulator, it was thought possible that the color variation between the high and low permittivity samples could be due to an existence of presence of Ti^{3+} due to reduction. To test this hypothesis, a quick annealing study of two ‘grey’ high

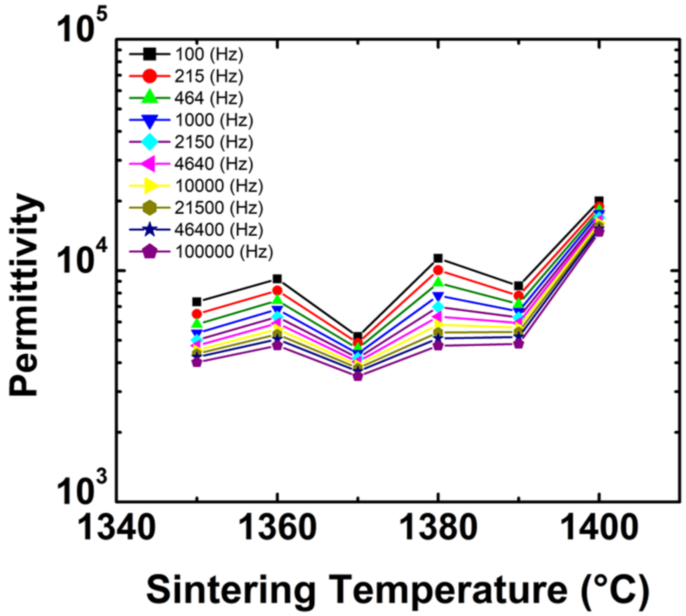

Figure 5.6: Maximum permittivity as a function of sintering temperature and frequency for BCZT – 1% BZT sintered between 1350°C and 1400°C

permittivity samples was executed. Two samples were annealed at 800°C/8 hours in air to ensure the samples could fully oxidize to Ti^{4+}. However, post annealing the samples had no physically visible change and only exhibited a decrease in their dielectric response of both permittivity and loss.

The results of this study further show that this composition is very sensitive to both processing parameters and physical conditions. While inconclusive on the underpinning mechanism of impurity formation, the systematic variation in sintering temperature showed that impurities do still exist at each sintering temperature and, in these samples, the relaxor phase is still present with observable space charge contributions visible (loss values > 0.1, frequency dependence in high temp regime. This further supports the initial suggestion that this composition is very sensitive to stoichiometry and possible volatilization of low melting point constituents. It also further supports the possibility that the observed high magnitude of the permittivity response is driven by existing secondary, or impurity, phases. As further support for these conclusions, the 1350°C five-sample batch vastly differed from the single sample prepared at 1350°C in the varied sintering temperature study as well as the 1400°C five-sample batch reproducibility study. These samples contained no visible secondary phase which could be identified by XRD and the dielectric response did not exhibit the desirable relaxor ferroelectric phase seen in every other sample thus far. Therefore, the most probable cause of impurity formation during sintering in these samples is off-stoichiometries due to volatilization of unreacted reagents or re-oxidation of Ti^{3+} during the cooling process. As Bi_2O_3 is the reagent with the lowest melting point (817°C,) it is therefore the most likely to volatilize during sintering. To combat volatilization, experiments to minimize chemical gradients for volatilization (incorporation of Bi_2O_3 excess) were developed, and to control the re-oxidation process of high temperature stable Ti^{3+} to low temperature stable Ti^{4+} faster cooling rates were suggested, as the slow cooling rate of 2°C/min could help to stabilize $Ti^{3+} - V_O^{\bullet\bullet}$ defect structures. If both factors contribute to the formation of secondary phases in this material, then it would follow that samples synthesized with only the rapid cooling rate would still have a small extent of secondary phase due to Bi volatilization during heating.

5.4.3 Considerations for Cooling Rate and Volatile Cation Excess

To further elucidate and refine the role of processing parameters on impurity formation in the desired composition, two samples were made with a cooling rate of 10°C/min for a sintering temperature of 1400°C/4h. Note that this maintains the 2°C/min heating rate and only varies the cooling rate. Both samples were isolated in their own crucible, one surrounded with stoichiometric sacrificial powder, and the other surrounded with 3 mol% Bi_2O_3 excess modified sacrificial powder. Post processing, both samples were

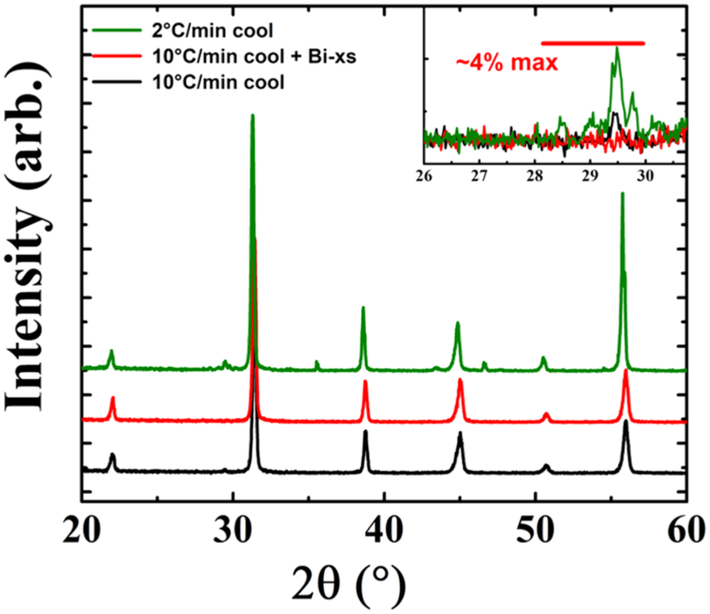

Figure 5.7: XRD patterns of BCZT – 1% BZT samples sintered at 1400°C/4h with 10°C/min cooling rate. Samples were sintered in individual crucibles, one stoichiometric and one with 3 mol% Bi_2O_3 excess incorporated into the sacrificial powder. XRD pattern of initial 1400°C sample from chapter 4 (2°C/min cool) included for reference. Insert zooms on region of main impurity peaks showing small impurity peak in the stoichiometric sample with 10°C/min cooling and no impurities in the sample with 10°C/min cooling and incorporated Bi excess

determined to be 93% theoretical density, and of visual appearance like that of the 1350°C five-batch samples. X-ray diffraction patterns of the two samples, with the initial 1400°C sample reported in chapter 4 for comparison, are reported in **Figure 5.7** and clearly show peaks of the desired perovskite phase with little to no intensity due to impurities. Upon closer inspection, a very low intensity impurity peak can be observed in the sample without Bi_2O_3 excess at 29.4° 2θ whereas the sample with included Bi_2O_3 excess exhibits no observable impurity peaks. This is consistent with hypothesis that both mechanisms of re-oxidation of Ti^{3+} and volatilization of Bi are at play in the synthesis of this material. It is also consistent with the observed phase purity in the 1350°C five-sample batch, further supporting the importance of the chemical environment within the crucible on the driving force for impurity formation.

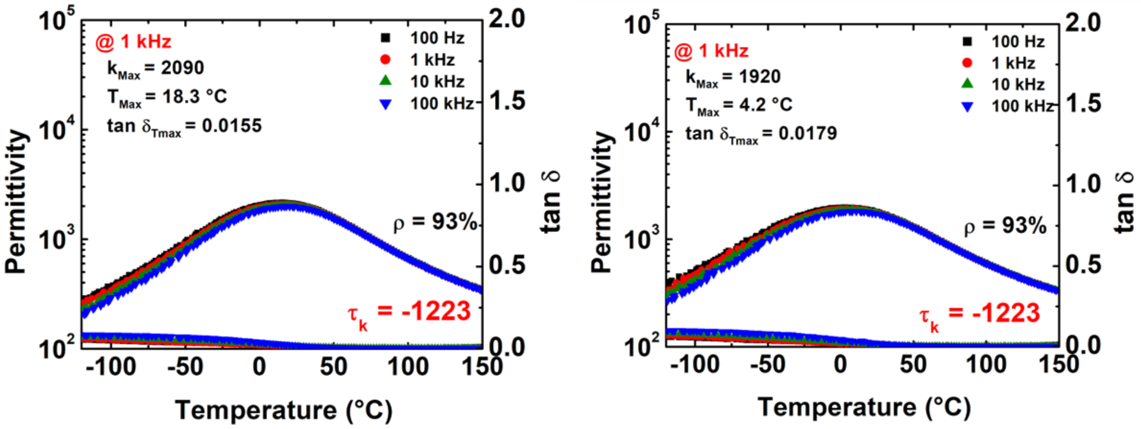

Figure 5.8: Low temperature dielectric spectroscopy of BCZT – 1% BZT samples cooled at 10°C/min stoichiometrically (left) and with 3mol% Bi_2O_3 excess incorporated into the sacrificial powder (right)

Low temperature dielectric spectroscopy for these two samples is reported in **Figure 5.8**. Both samples exhibit the normal ferroelectric insulator-like response, with a small extent of frequency dispersion, as observed in the single phase 1350°C five-sample batch. Both samples have relatively low permittivity (ε_r ~ 2000 @ T_{max}), low loss (*tan* δ ~ 0.015), with significant variation in T_{max} (18.3°C no excess, 4.2°C with excess). While these values are not in close agreement with the 1350°C five-sample batch, these results strongly suggest that the single-phase stoichiometric composition does not exhibit the observed desirable relaxor ferroelectric phase at very high permittivity. They further suggest that the high permittivity relaxor phase, reported in the original work, is driven by secondary phases due to A-site deficiencies, due to loss of Bi during sintering, and that this relaxor phase is very sensitive to the extent of secondary phases, or existence of specific secondary phases, play an intricate role in determining the key parameters ε_r, *tan* δ, and T_{max}.

5.4.4 Microcopy Studies of Selected Samples

To ensure that the observed phenomena are not further convoluted by, or attributable to, microstructure effects, SEM studies were carried out on selected samples representing three observed regimes, impure – high permittivity; impure – medium permittivity; and single phase – low permittivity. The samples chosen for this study were the second 1400°C sample from the original report in Chapter 4, the 1380°C sample from the sintering temperature study, and the 10°C with excess sample from the final study, respectively. Micrographs of these samples are reported in **Appendix B**. Notably, both the grain size and homogeneity vary widely between all samples with the most typical homogenous grain structure appearing in the impure – high permittivity sample. While this sample exhibits the most typical grain structure, it still has a wide range of grain sizes, from 1 μm to 10 μm, much smaller than expected as it was the highest permittivity sample, and a larger extent of porosity than expected given density measurements. The single phase – low permittivity sample exhibits much larger grains, from 30 μm to >60 μm, again with a larger extent of observable pores than expected. Finally, the impure – medium permittivity sample exhibits the least typical grain structure with large grain size disparity, with very large grains (~50 μm) in a matrix of smaller grains of inhomogeneous morphology and size distribution.

5.5 Conclusions

The processing conditions leading to the unexpected temperature stable high permittivity relaxor ferroelectric composition based on BCZT were considered and investigated. Reproducibility studies of five samples in the same crucible prepared under the exact same conditions showed the relaxor ferroelectric phase could be repeated, however only half of the initial reported magnitude in the permittivity was realized. Reproducibility studies also showed that the impurity phases inherent in this composition were very sensitive to crucible environment. In attempt to inhibit secondary phase formation a sintering temperature study was employed varying the sintering temperature at 10°C intervals. This study showed impurities to exist at each sintering temperature, with little correlation between the magnitude of the observed permittivity and the sintering temperature. All samples in the sintering study with impurities exhibited the same characteristics of the relaxor ferroelectric phase observed in the initial report though with varying magnitudes in the permittivity response. As it was hypothesized that the chemical environment in the crucible during sintering could play a large role in crystallization, a side by side study of the five-sample reproducibility study was done with five-samples at the lowest sintering temperature, 1350°C. A representative sample of this five-sample batch deviated greatly from the single sample sintered at 1350°C in the varied sintering temperature study, in that it no longer exhibited the relaxor ferroelectric characteristics, it exhibited a very low permittivity response correlated to much lower dielectric losses generally attributed to true dielectric insulators, it physically differed in color, and it exhibited little to no secondary phases. This further confirms the hypothesis that the composition was very sensitive to stoichiometry and processing conditions.

With the most probable mechanism for the observed non-stoichiometry being volatilization of Bi_2O_3 during sintering and oxidation of Ti during cooling, the cooling rate was increased for the initial processing conditions (1400°C/4h with 2°C/min heating) from 2°C/min to 10°C/. Simultaneously, bismuth excess was incorporated in a parallel study to further diminish impurity formation due to off-stoichiometries. Both samples with the increased cooling rate exhibited minimal secondary phases, with the bismuth excess sample exhibiting little to no impurities via XRD. Furthermore, both samples were of similar color to the representative sample from the five-sample batch experiment at 1350°C and did not show the relaxor ferroelectric characteristics observed in the samples of desirable dielectric response. Therefore, the temperature stable, high permittivity relaxor ferroelectric composition was determined to be driven by the presence of secondary phases. While generally these secondary phases contribute to space charge mechanisms in the permittivity response which therefore make them unsuitable for capacitor applications, it was noted that the reproduced samples at 1400°C exhibited relatively low dielectric losses with little to no frequency dependence in the loss at room temperature. This suggest that only a small fraction of the permittivity response at higher temperatures would be due to space charge mechanisms. It could be plausible that one of the observed secondary phases stabilizes the observed relaxor ferroelectric phase, and that, with further understanding of the secondary phases present, the loss issues and space charge contributions could be mitigated while the desirable permittivity response for capacitor applications could be maintained.

5.6 References

[1] W. S. H. M. W. Ahmad *et al.*, “5G Technology: Towards Dynamic Spectrum Sharing Using Cognitive Radio Networks,” *IEEE Access*, vol. 8, pp. 14460–14488, 2020.

[2] Y. Honda, “No Title,” *AEI*, p. 48, Oct-2004.

[3] G. H. Haertling, “Ferroelectric ceramics: History and technology,” *J. Am. Ceram. Soc.*, vol. 82, no. 4, pp. 797–818, Apr. 1999.

[4] X. Wang, J. Yue, and J. Liu, “Enhanced temperature stability and electrical properties of Bi/Mn co-doped (Ba,Ca) (Zr,Ti)O3 lead-free ceramics,” *Ceram. Int.*, vol. 47, no. 2, pp. 2525–2530, Jan. 2021.

[5] Bruchhaus, “US PATENT 6109191.”

[6] M. Acosta *et al.*, “BaTiO $_3$ -based piezoelectrics: Fundamentals, current status, and perspectives,” *Appl. Phys. Rev.*, vol. 4, no. 4, p. 041305, Dec. 2017.

[7] M. McQUARRIE and F. W. BEHNKE, “Structural and Dielectric Studies in the System (Ba, Ca) (Ti, Zr)O3,” *J. Am. Ceram. Soc.*, vol. 37, no. 11, pp. 539–543, Nov. 1954.

[8] P. Hansen, D. Hennings, and H. Schreinemacher, “Dielectric Properties of Acceptor-Doped (Ba,Ca)(Ti,Zr)O 3 Ceramics,” *J. Electroceramics*, vol. 2, no. 2, pp. 85–94, 1998.

[9] N. Chaiyo, D. P. Cann, and N. Vittayakorn, “Lead-free (Ba,Ca)(Ti,Zr)O3 ceramics within the polymorphic phase region exhibiting large, fatigue-free piezoelectric strains,” *Mater. Des.*, vol. 133, pp. 109–121, Nov. 2017.

[10] L. E. Cross, “Relaxorferroelectrics: An overview,” *Ferroelectrics*, vol. 151, no. 1, pp. 305–320, Jan. 1994.

[11] M. A. Zurbuchen *et al.*, “Bismuth volatility effects on the perfection of SrBi2Nb2O9 and SrBi2Ta2O9 films,” *Appl. Phys. Lett.*, vol. 82, no. 26, pp. 4711–4713, Jun. 2003.

[12] “Bismuth Oxide | AMERICAN ELEMENTS ®.” [Online]. Available:

https://www.americanelements.com/bismuth-oxide-1304-76-3.

Chapter 6

6.1 Introduction

With the state of high permittivity literature being complex, there are various other materials systems in need of further investigation. This chapter will explore preliminary experimental studies into some of these systems with reported high, or 'colossal,' permittivities. These material systems are non-ferroelectric in nature and consist of co-doped titanium oxide [1] and barium iron niobate ($Ba(Fe,Nb)O_3$, BFN) [2]–[5] as discussed in Chapter 1 sections 1.7.2.2.1 and 1.7.2.3. The dielectric properties of these materials, as reported by the literature in Chapter 1, are summarized in **Table 6.1**. These materials systems are of note as the literature shows their permittivity to be nearly temperature independent over the region of interest for MLCCs [1], [2]. Concerns have been raised that this type of permittivity response, as seen in various very high permittivity systems ($CaCuTiO_4$, etc.), is indicative of Maxwell – Wagner type mechanisms [6], and therefore would not be viable for MLCC applications. However, the observed desirable permittivity

Table 6.1
Summary of dielectric properties for non-ferroelectric high permittivity materials systems as found in literature

1 kHz	**T_{max} (°C)**	**$\varepsilon_{r,max}$**	**tan δ_{max}**	**ε_r (r.t.)**	**tan δ (r.t.)**	**ref**
TiO_2 10% (Nb + In)	--	70000	0.4	60000	0.015	[1]
$Ba(Fe_{1/2}Nb_{1/2})O_3$	275	145000	0.75	45000	0.4	[4]
$Ba(Fe_{1/2}Nb_{1/2})O_3$	275	200000	1	65000	0.8	[5]
$Ba(Fe_{1/2}Nb_{1/2})O_3$	227	90000	--	25000	--	[3]
$Ba(Fe_{1/2}Nb_{1/2})O_3$	200	50000	0.6	32000	0.13	[2]

responses necessitate further study into these systems to determine the underlying polarization mechanisms that contribute to the permittivity response.

6.2 Co-doping in Titanium Oxide

Ceramics of co-doped TiO_2 was fabricated through replication of processing parameters to the best extent from *W. Hu et al*. Samples of 10% (Nb + In)-doped TiO_2 were developed via mixed oxide solid solution processing, with starting reagents of TiO_2 (CERAC, 99.9%), Nb_2O_5 (Sigma, 99.9%), and In_2O_3 (Alfa Aesar, 99.9%) massed stoichiometrically to $Ti_{0.90}(Nb_{0.05}In_{0.05})O_2$. These batched powders were then milled for 10 hours in an EtOH and YTZ media slurry and dried. No calcination step was utilized in this system. The dried batched powder was then formed into cylindrical green bodies through

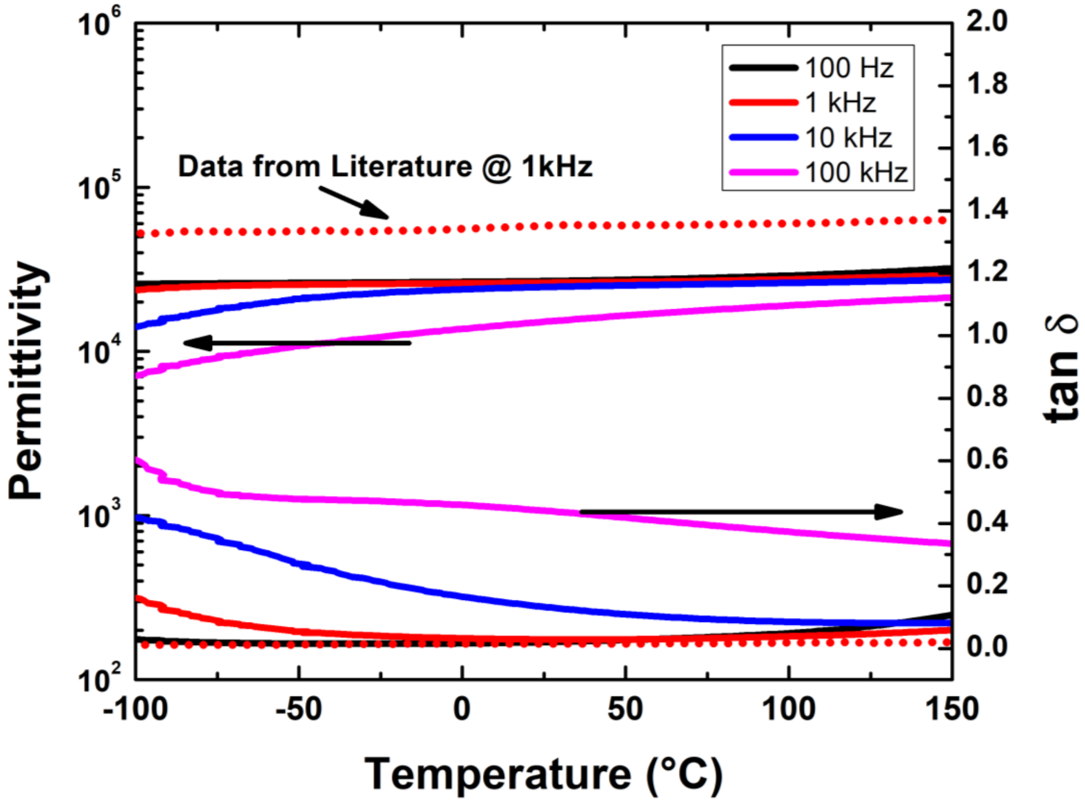

Figure 6.1: Low temperature dielectric spectroscopy of laboratory synthesized 10% (Nb + In) co-doped TiO_2 as recreated from the literature Hu et al. [1] dotted lines represent data recreated from that reported by Hu et al. and are included for comparison.

use of a uniaxial die press at 170 MPa for 3 mins, and stable green bodies were then sintered at 1400°C/10h. The as-sintered In-Nb-doped TiO_2 samples were then confirmed to be within 90% of the theoretical density (based off the density of the parent TiO_2 structure) and appeared visually similar as per their description in literature.

Low temperature dielectric studies of the synthesized TiO_2 – 10% (Nb + In) ceramics show that the reproduced sample exhibited a similar permittivity response, however only realized ~47% of the permittivity magnitude reported in the literature while exhibiting similar dielectric losses. Absolute values of these parameters are tabulated and reported in **Table 6.2** and the dielectric response as a function of frequency and temperature can be visualized in **Figure 6.1**. This discrepancy was partially attributed to the observed low density. Observable from **Figure 6.1** is some frequency dependence to the dielectric properties, namely the decrease in permittivity and increase in loss with increasing frequency. This behavior was, notably, not observed in the original work, and can also be attributed to the low apparent density or experimental anomalies at high frequency.

Table 6.2
Summary of dielectric properties for 10% (Nb+In) co-doped TiO2 at 1kHz as reported in literature by Hu et al. and recreated in this work

1kHz	**$\varepsilon_{r,AVG}$**	**τ_k (ppm/ε_r)**	**tan δ**
Hu et al.	56400	543	0.015
Recreated	26600	606	0.012

To help elucidate any underlying mechanisms to the permittivity response observed in **Figure 6.1**, the voltage dependence of the dielectric properties was measured and reported in **Figure 6.2**. These voltage dependent measurements were completed using an impedance spectrometer at room temperature with an applied DC bias of 0V to 35V with

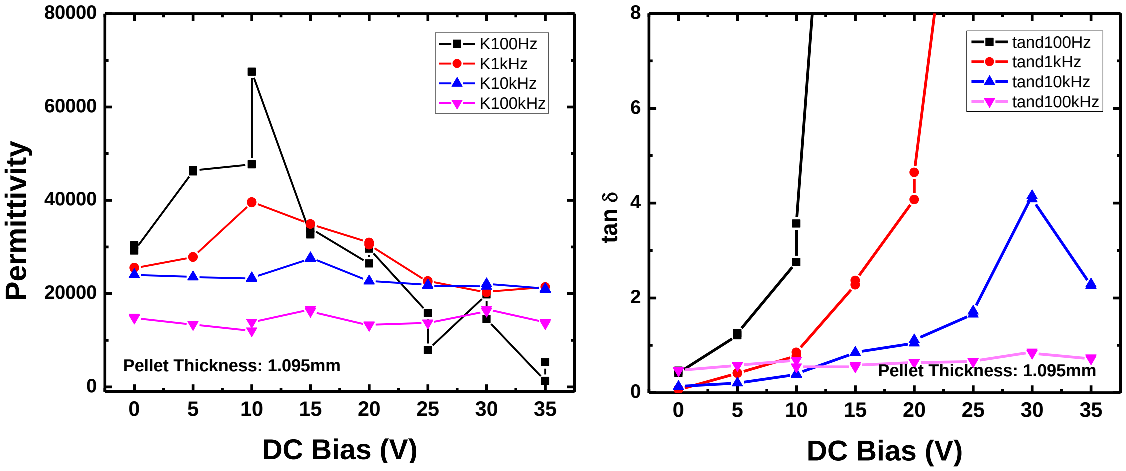

Figure 6.2: Dielectric properties at room temperature as a function of applied voltage for recreated 10% (Nb+In) co-doped TiO_2 as measured on an impedance analyzer with a 1V oscillating voltage. Applied fields approach 0.35 kV/cm when taking account for sample thickness

a 1V (ac) oscillating voltage. In the measurement of the permittivity and loss as a function of voltage for the CD TiO_2 sample there does not appear to be a strong correlative variation in the permittivity response, however a large, near instantaneous, increase in the dielectric loss occurs at low frequencies. As the dielectric loss, *tan δ*, is unphysical for values >1 (representing conduction within the sample,) at very low applied fields the sample becomes conductive. With the sample thickness at ~ 1mm, we can see that at 1kHz frequency the sample becomes conductive at ~ 0.1 kV/cm (10V/mm) which increases to ~0.2 kV/cm at 10kHz frequency. This suggests that the proposed mechanism for the observed high permittivity in literature reports, specifically, defect structures stabilized by the co-doping scheme which pin mobile electrons, may be viable but it limited to low voltages. It follows that the application of sufficient voltage to overcome the energy barrier of the defect electron pinning site would result in increasing the materials conductivity, agreeing with the observed data. However, it should be noted that, as the frequency dependence in the replicated sample is much greater than that observed in the literature and the replicated sample was on the boundary of sufficient density (~90% the theoretical), that the sample could have inherent secondary phases or microscopic defects (pores, inhomogeneities, etc.) which could also account for the observed high losses and early onset of conduction under applied voltage. More studies into refinement of processing parameters would be necessary to deconvolute these issues and develop higher quality ceramics to decouple microstructure contributions to the permittivity from the inherent materials properties.

6.3 Barium Iron Niobate

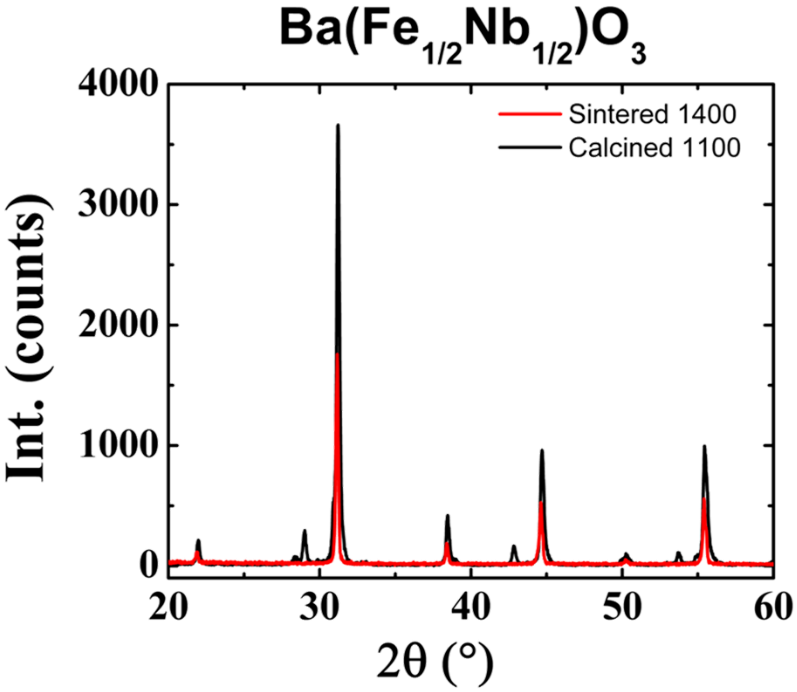

Figure 6.3: X-ray diffraction of BFN-1 samples post calcination at 1100°C/4h and post sintering at 1400°C/4h. Variations in maximum peak intensity between the two patterns is attributed to differences between XRD on a randomly ordered powder and dense ceramics with possible preferred orientations.

Barium Iron Niobate was fabricated through the replication of processing parameters from *Raevski et al.* to the desired stoichiometry of $Ba(Fe_{1/2}Nb_{1/2})O_3$ (BFN-1). As both iron and niobium are multi-valent cations, a secondary batch was fabricated in parallel utilizing the same parameters to the stoichiometry of $Ba(Fe_{1/3}Nb_{2/3})O_3$ (BFN-2) in

Figure 6.4: Images of (a) synthesized and polished dense BFN-1 ceramic showing dark metallic appearance, and (b) resistivity measurement of as-polished surface with a laboratory voltammeter of the dense BFN-1 ceramic

order to drive Fe(II) into the substitutional solid solution. With charge variance playing a large role in dipole magnitude, forcing iron into a reduced state through stoichiometry variation on the B-site could possibly increase the permittivity of the system. As determined from the literature, batched powders were milled for 6 hours, dried, then calcined at 1100°C/4h. Post calcination, powders were again milled for 6 hours, mixed with 2 wt% poly-vinyl butyral (PVB) polymer binder, pressed uniaxially in a 13mm cylindrical die press at 170MPa/3mins, and sintered at 1400°C/4h with 2°C/min ramps and a binder burnout step at 450°C/3h in alumina crucibles. Under these conditions, BFN-1 samples were successfully sintered to ~92% theoretical density by the Archimedes principle, however BFN-2 samples melted during processing. X-ray diffraction studies confirming single phase formation of BFN-1 with sintering can be found in **Figure 6.3**. Further study into the processing parameters for the BFN-2 system are suggested, namely adjusting the sintering temperature to avoid the melting point. It is also suggested that further studies with both compositions be processed in magnesia crucibles as barium oxide forms a stable solid solution with Al_2O_3 at high temperature [7] which could drive melting of the sample as well as reaction with the crucible.

As the sample of dense BFN-1 appeared very dark, with some metallic luster, as observed in **Figure 6.4a**, speculation was made to its insulative nature. Therefore, before electrodes were applied, to prepare the sample for low temperature permittivity studies a room temperature conductivity test was done with a laboratory voltammeter to crudely test whether the sample was insulating or conducting. As seen in **Figure 6.4b** the sample registered 4MΩ (0.25 μS) across the sample and 40MΩ (0.025 μS) through the sample thickness. These values suggest that BFN-1 is not insulating. As insulation resistance is necessary for capacitor applications, this system was no longer considered as a promising high permittivity material for capacitor applications. However, future studies with this system to develop an insulating high permittivity material could be feasible. Those suggested are solid solutions between BFN and $BaTiO_3$ (BT), with high phase fractions of BT, as well as doping of small phase fractions $LiNbO_3$ (LN) to induce a relaxor-like phase as well as potentially increase the permittivity due to the ionic size, and valence, difference between Ba(II) and Li(I).

6.4 Conclusions

Various materials systems were considered and investigated for possible high permittivity capacitor applications. Co-doped titanium oxide using niobium and indium studies showed that the reported ‘colossal’ permittivity is only accessible under low fields, as the application of direct DC bias induces conduction in the sample at low fields, ~0.1kV/cm at 1kHz and ~0.2kV/cm at 10kHz. Studies into barium iron niobate at Fe/Nb ratios of 1:1 and 1:2 (BFN-1 and BFN-2) showed BFN-2 to melt under the processing parameters, and a successfully densified BFN-1 to be conductive at room temperatures with 40MΩ•mm measured through the sample thickness via voltammeter. Samples of Ba(Ce_xTi_{1-x})O_3 were unsuccessfully processed given the parameters discovered in literature, and melted upon sintering to various degrees. It was determined that further studies into BFN systems could be beneficial, namely solid solutions of BT, BFN, and LN with large phase fractions of BT, and small additions of both BFN and LN.

6.6 References

[1] W. Hu *et al.*, "Electron-pinned defect-dipoles for high-performance colossal permittivity materials," *Nat. Mater.*, vol. 12, no. 9, pp. 821–826, Sep. 2013.

[2] I. P. Raevski, S. A. Prosandeev, A. S. Bogatin, M. A. Malitskaya, and L. Jastrabik, "High dielectric permittivity in AFe1/2B1/2O3 nonferroelectric perovskite ceramics (A=Ba, Sr, Ca; B=Nb, Ta, Sb)," *J. Appl. Phys.*, vol. 93, no. 7, pp. 4130–4136, Apr. 2003.

[3] Z. Wang, X. M. Chen, L. Ni, and X. Q. Liu, "Dielectric abnormities of complex perovskite Ba(Fe1⁄2Nb1⁄2)O3 ceramics over broad temperature and frequency range," *Appl. Phys. Lett.*, vol. 90, no. 2, p. 022904, Jan. 2007.

[4] D. Bochenek, P. Niemiec, I. Szafraniak-Wiza, M. Adamczyk, and R. Skulski, "Preparation and dielectric properties of the lead-free BaFe1/2Nb1/2O3 ceramics obtained from mechanically triggered powder," *Eur. Phys. J. B*, vol. 88, no. 10, p. 277, Oct. 2015.

[5] D. Bochenek, P. Niemiec, M. Adamczyk, and I. Szafraniak-Wiza, "Physical properties of lead-free BaFe1/2Nb1/2O3 ceramics obtained from mechanochemically synthesized powders," *J. Mater. Sci.*, vol. 53, no. 19, pp.

13501–13512, Oct. 2018.

[6] P. Lunkenheimer, V. Bobnar, A. V Pronin, A. I. Ritus, A. A. Volkov, and A. Loidl, “Origin of apparent colossal dielectric constants.”

[7] R. Zhang and P. Taskinen, “A phase equilibria study and thermodynamic assessment of the BaO–Al2O3 system,” *Calphad*, vol. 51, pp. 42–50, Dec. 2015.

Chapter 7

7.1 Conclusions and Future Work

In this dissertation, complex dielectric materials for advanced applications were developed through the application of fundamental concepts. Solid state chemistry was utilized to develop solid solutions, in which a material could be manipulated through the incorporation of chemical variation. These variations would directly influence the materials overall (bulk) structure, directly impacting the resultant materials properties due to inherent structure-property relationships, as a materials properties are dependent on interactions of atoms (or ions in the case of oxide materials) within the material and a materials structure determines allowable atomic/ionic interactions. These techniques were applied to a specific category of materials, perovskite metal oxides, as the structure of these materials easily allow for desirable materials properties, piezoelectricity, ferroelectricity, etc. As these properties are all dependent on the displacement of charge under the application of an electric field, also known as the dielectric effect, a fundamental understanding of displacement mechanisms in ionically bonded materials was developed and utilized to manipulate the structure of established solid solutions to enhance desired materials properties.

In doing so, the experimental synthesis and dielectric properties of various complex perovskite solid solutions. These included a modification of the piezoelectric material $Pb(Zr,Ti)O_3$ (PZT 52/48) to incorporate $BiInO_3$ in the solid solution $xBiInO_3$ – (1-x) $Pb(Zr_{0.52}Ti_{0.48})O_3$ (BI-PZT) and the lead-free dielectric material 99% $Ba_{0.85}Ca_{0.15}(Zr_{0.10}Ti_{0.90})O_3$ – 1% $Bi(Zn_{1/2}Ti_{1/2})O_3$ (BCZT-BZT). Bismuth indate modified

PZT was considered for potential high temperature dielectric applications and found the solubility limit for BI into PZT 52/48 to be ~15%. The addition of BI to PZT 52/48 induced a compositionally dependent phase transition at room temperature from tetragonal to rhombohedral with increasing %BI. A region of mixed phase stability was observed at 2.5% BI where both rhombohedral and tetragonal phases were present in X-ray diffraction studies. High temperature dielectric spectroscopy showed all BI modified compositions to contain a visible extent of frequency dispersion in the permittivity and a decrease in the apparent Curie temperature as a function of increasing % BI. Furthermore, the permittivity response at, and around, the Curie temperature showed decreasing tetragonal character from 0% - 5% BI, with the 7.5% BI composition showing characteristics typical of a rhombohedral phase transition. Divergently, the 10% BI composition showed characteristics again of a tetragonal phase transition with relatively high permittivities. This suggested the existence of a critical Zr/In B-site ratio at which the tetragonal phase becomes again more stable than the rhombohedral. This was supported by the room temperature tetragonal structure of $PbTiO_3$ – $BiInO_3$ binary solid solutions. Ferroelectric studies of the BI-PZT system showed all compositions to be nominal ferroelectrics that saturate around ~ 50kV/cm with coercive fields averaging ~20 kV/cm. These findings were consistent with observed trends in Bi based endmember modifications of PZT 52/48, where increasing additions of the Bi endmember lowered the Curie temperature of the solid solution.

In the second project, bismuth zinc titanate (BZT) modification of the dielectric material BCZT was considered for the development of a high permittivity, temperature-stable, material for multi-layer capacitor applications. The addition of the bismuth endmember was considered to induce relaxor like behavior through chemical inhomogeneity on the A and B site. Initial studies showed that modifications >5% greatly suppresses the permittivity response while inducing relaxor like behavior. However, it was found that very small additions (1%) of the endmember induced an unexpectantly high permittivity response, ε_r = 36640 @ T_{max}, as well as the desired relaxor ferroelectric phase. The temperature response of the 1% BZT modified $Ba_{0.85}Ca_{0.15}(Zr_{0.10}Ti_{0.90})O_3$ was observed to be very desirable with a τ_κ = -2469 from -55°C – 85°C, however signs of impurity induced space charge contributions were observed in the high temperature frequency dependence of the permittivity as well as relatively high losses of $tan\ \delta \sim 0.2$. This was further supported by the observation of secondary phases via X-ray diffraction of the dense pellet with a relative intensity of 4% the maximum. Voltage dependence of the dielectric properties further supported the contribution of space charge mechanisms to the observed permittivity with dielectric loss values increasing with the application of low-fields (up to 1kV/cm) through application of DC bias with a oscillating voltage of 1V. Reproducibility studies were successfully preformed confirming the existence of this high permittivity relaxor ferroelectric phase, however only realized ~50% of the permittivity magnitude correlating to a decrease in the dielectric loss. Secondary phases were also observed in the reproduced samples; however, they were observed to a lesser extent, ~ 2% the maximum intensity, and, more notably, various secondary phase peaks were not present in the reproduced samples.

Processing studies into the formation and stability of these secondary phases were further carried out to mitigate any space charge contributions to the permittivity, as these contributions are deleterious to the materials utility for capacitor applications. Studies into decreasing the sintering temperature from 1400°C to 1350°C with 10°C intervals did not result in any clear correlations between the sintering temperature and secondary phase formation. All samples showed signs of relaxor character seen in the original and recreated samples as well as a variety of impurity peaks, however the permittivity magnitude varied widely between all samples, with no apparent correlation. A secondary study of five samples sintered in the same crucible at 1350°C showed a large variation between the 1350°C sample sintered in the varied sintering temperature study and those of the five-sample batch. Those of the five-sample batch no longer showed the desired relaxor characteristics or high permittivity (ε_r ~ 5000 at T_{max}) however, were single phase by XRD. This suggested that the secondary phase formation could be sensitive to chemical gradients within the crucible during sintering.

To confirm this, studies of increased cooling rate (from 2°C/min to 10°C/min) as well as incorporated excess of volatile elements (3 mol% Bi_2O_3) into the sacrificial powder were completed. These studies returned single phase samples like those observed in the five-sample batch at 1350°C by XRD, again without the desired high permittivity phase of relaxor ferroelectric character. Notably, the maximum permittivities of these studies were much lower than that of the five-sample batch (ε_r ~ 2000 at T_{max}). It was concluded that this composition was very sensitive to both processing conditions as well as stoichiometry, and that the very desirable high permittivity relaxor ferroelectric character phase was driven by off-stoichiometry impurities.

In general, two different complex dielectric systems were considered for advanced electronic applications. Approaches for both systems were similar, where a well-known parent composition was modified with a tertiary, or quaternary, endmember to vary or improve upon desired materials properties. Systems were developed mainly on an experimental synthesis basis and led to diverse outcomes. The overall results pointed to two main takeaways, the first being that secondary processing effects, such as componential volatilization, play an exceedingly large role in crystallization and densification of complex ceramic oxides. This could be especially important as research around compositional volatilization during processing was found to be very sparse and determining best practices to account for this phenomena tends to be done experimentally on a case to case basis. As many metal oxide precursors common to advanced dielectric processing volatilize readily (PbO, Bi_2O_3, Na_2CO_3, K_2CO_3, etc.) developing a more fundamental knowledge base on the underpinning mechanisms in this phenomena could benefit the ceramics community on a whole. The second main takeaway from this work was that very small additions of chemically diverse species to a complex ferroelectric solid solution can induce relaxor ferroelectric phases. These very small additions can also result in properties very disparate from the parent solution and lead to compositions exceedingly sensitive to chemical variation through processing effects. Furthermore, for considerations to high permittivity research, additions to complex solid solutions > 5%, end up greatly suppressing the permittivity of the parent solution.

Moving forward with the work presented in this dissertation, there are three main suggested avenues for pursued research. The first suggested avenue would be for the re-consideration of the BI-PZT system for high temperature ferroelectrics. It was asserted in chapter 3 of this work that the large phase fraction of lead zirconate, which stabilizes the rhombohedral phase in the parent PZT solid solution, was responsible for the observed decrease in the Curie temperature with increasing %BI, as it appears in literature that the addition of Bi-based endmembers to PZT stabilizes the rhombohedral phase at high phase fractions of PZ. Studies to elucidate the mixed phase boundary in the BI-PT-PZ ternary for low fractions of PZ could plausibly beneficial to finding the critical PZ/PT ratio at which the tetragonal character of PT-BI binaries would be sufficient to overcome the observed stabilization of the rhombohedral phase, and lead to development of high Curie temperature ferroelectrics.

The final avenue of research would be to further pursue studies into the BCZT-BZT solid solution discussed in chapters 4 and 5. While the initial sample definitely contained large contributions to the permittivity from secondary phase stabilized space charge, reproduced samples contained a varying secondary phase phenomenology and resulted in less frequency dependence in the dielectric loss, as well as >50% lower values in dielectric loss while maintaining desirable relaxor characteristics and high permittivity of ~ 20,000. Further studies into identifying the secondary phases present and responsible for these phenomena, as well as *in situ* crystallization XRD studies to elucidate reaction pathways could be very beneficial to determining the underlying mechanisms responsible for the observed results and could prove crucial in developing a high permittivity, temperature stable material for multi-layer ceramic capacitor applications.

Bibliography

[1] J. Ho, T. R. Jow, and S. Boggs, “Historical introduction to capacitor technology,” *IEEE Electr. Insul. Mag.*, vol. 26, no. 1, pp. 20–25, Jan. 2010.

[2] B. Park, *A History of Electricity: (The Intellectual Rise in Electricity) from Antiquity to the Days of Benjamin Franklin*. J. Wiley & Sons, 1895.

[3] Z. D. Boren, “There are officially more mobile devices than people in the world | The Independent | The Independent,” *Independent*, 2014. [Online]. Available: https://www.independent.co.uk/life-style/gadgets-and-tech/news/there-are-officially-more-mobile-devices-people-world-9780518.html. [Accessed: 08-Dec-2020].

[4] Y. Honda, *AEI*, p. 48, Oct-2004.

[5] C. Hendricks, Y. Min, and V. Magadala, “What is happening to the long term life of MLCCs,” in *CARTS*, 2010, pp. 3–11.

[6] A. J. Moulson and J. M. Herbert, *Electroceramics*. Chichester: John Wiley & Sons, Ltd, 2003.

[7] M. Fortunato, “Temperature and Voltage Variation Ceramic Capacitor | Maxim Integrated,” *Maxim Integrated*, 2012. [Online]. Available: https://www.maximintegrated.com/en/design/technical-documents/tutorials/5/5527.html. [Accessed: 08-Dec-2020].

[8] J. C. Maxwell, “A Treatise on Electricity and Magnetism,” *Nature*, vol. 7, no. 182, pp. 478–480, Apr. 1873.

[9] K. W. Wagner, “Zur Theorie der unvollkommenen Dielektrika,” *Ann. Phys.*, vol. 345, no. 5, pp. 817–855, Jan. 1913.

[10] Q. Tan, P. Irwin, Non-Member, and Y. Cao, “Advanced Dielectrics for Capacitors Non-member.”

[11] J. C. Manley, “Encapsulated electrical capacitor,” US3496435A, 09-Dec-1968.

[12] R. G. Capek and J. P. Mazintas, “Method of making multilayer ceramic capacitors,” US3549415A, 15-Jul-1968.

[13] T. I. Prokopowicz, “High voltage ceramic capacitor,” US3496434A, 22-Nov-1968.

[14] F. Kossar, “Method of making multilayer circuit system,” US3545079A, 02-May-1968.

[15] A. R. Rodriguez and C. John, “Process for manufacturing multilayer ceramic capacitors,” UA3235939, 06-Sep-1962.

[16] X. Zhao, B. M. Sánchez, P. J. Dobson, and P. S. Grant, “The role of nanomaterials in redox-based supercapacitors for next generation energy storage devices,” *Nanoscale,* vol. 3, no. 3, p. 839, Mar. 2011.

[17] T. Hans and D. James, “Insulating material,” US2429588A, 02-Oct-1941.

[18] C. A. Randall, R. E. Newnham, and L. E. Cross, “History of the First Ferroelectric Oxide, $BaTiO_3$.”

[19] O. Saburi, “Properties of Semiconductive Barium Titanates,” *J. Phys. Soc. Japan*, vol. 14, no. 9, pp. 1159–1174, Sep. 1959.

[20] P. W. Forsbergh, “Domain Structures and Phase Transitions in Barium Titanate,” *Phys. Rev.*, vol. 76, no. 8, pp. 1187–1201, Oct. 1949.

[21] J. P. Remeika, “A Method for Growing Barium Titanate Single Crystals,” vol. 76, pp. 940–941, 1953.

[22] A. F. Devonshire, “XCVI. Theory of barium titanate,” *London, Edinburgh, Dublin*

Philos. Mag. J. Sci., vol. 40, no. 309, pp. 1040–1063, Oct. 1949.

[23] A. F. Devonshire, “CIX. Theory of barium titanate— *Part II*,” *London, Edinburgh, Dublin Philos. Mag. J. Sci.*, vol. 42, no. 333, pp. 1065–1079, Oct. 1951.

[24] J. T. Last, “Infrared-Absorption Studies on Barium Titanate and Related Materials,” *Phys. Rev.*, vol. 105, no. 6, pp. 1740–1750, Mar. 1957.

[25] E. C. Subbarao, M. C. McQuarrie, and W. R. Buessem, “Domain Effects in Polycrystalline Barium Titanate,” *J. Appl. Phys.*, vol. 28, no. 10, pp. 1194–1200, Oct. 1957.

[26] R. D. Burbank, H. T. Evans, and IUCr, “The crystal structure of hexagonal barium titanate,” *Acta Crystallogr.*, vol. 1, no. 6, pp. 330–336, Dec. 1948.

[27] A. G. Chynoweth, “Surface Space-Charge Layers in Barium Titanate,” *Phys. Rev.*, vol. 102, no. 3, pp. 705–714, May 1956.

[28] N. Blattau, D. Barker, and C. Hillman, “Lead Free Solder and Flex Cracking Failures in Ceramic Capactiors,” in *CARTS*, 2004.

[29] Bruchhaus, “US PATENT 6109191.”

[30] P. Lunkenheimer, V. Bobnar, A. V Pronin, A. I. Ritus, A. A. Volkov, and A. Loidl, “Origin of apparent colossal dielectric constants.”

[31] J. F. Scott, A. Schilling, S. E. Rowley, and J. M. Gregg, “Some current problems in perovskite nano-ferroelectrics and multiferroics: kinetically-limited systems of finite lateral size,” *Sci. Technol. Adv. Mater.*, vol. 16, no. 3, p. 036001, Jun. 2015.

[32] P. Curie, “Sur la symétrie dans les phénomènes physiques, symétrie d’un champ électrique et d’un champ magnétique,” *J. Phys. Théorique Appliquée*, vol. 3, no. 1, pp. 393–415, 1894.

[33] A. A. Bokov and Z.-G. Ye, “Recent progress in relaxor ferroelectrics with perovskite structure,” *J. Mater. Sci.*, vol. 41, no. 1, pp. 31–52, Jan. 2006.

[34] G. Burns, F. H. Dacol, G. Burns, and F. H. Dacol, “Glassy polarization behavior in ferroelectric compounds and,” *Solid State Commun.*, vol. 48, no. 10, pp. 853–856, Dec. 1983.

[35] A. Naberezhnov, S. Vakhrushev, B. Dorner, D. Strauch, and H. Moudden, “Inelastic neutron scattering study of the relaxor ferroelectric PbMg Nb O at high temperatures,” *Eur. Phys. J. B,* vol. 11, no. 1, pp. 13–20, Sep. 1999.

[36] V. V. Shvartsman, W. Kleemann, T. Łukasiewicz, and J. Dec, “Nanopolar structure in Sr x Ba 1 − x Nb 2 O 6 single crystals tuned by Sr∕Ba ratio and investigated by piezoelectric force microscopy,” *Phys. Rev. B*, vol. 77, no. 5, p. 054105, Feb. 2008.

[37] S. Vakhrushev, A. Nabereznov, S. K. Sinha, Y. P. Feng, and T. Egami, “Synchrotron X-ray scattering study of lead magnoniobate relaxor ferroelectric crystals,” *J. Phys. Chem. Solids,* vol. 57, no. 10, pp. 1517–1523, Oct. 1996.

[38] W. Ge *et al.*, “Direct evidence of correlations between relaxor behavior and polar nano-regions in relaxor ferroelectrics: A case study of lead-free piezoelectrics $Na_{0.5}Bi_{0.5}TiO_3$ - x %$BaTiO_3$,” *Appl. Phys. Lett.*, vol. 103, no. 24, p. 241914, Dec. 2013.

[39] A. J. Bell, Private Communication.

[40] G. Rose, “Perowskit,” *Ann. Phys.,* vol. 48, p. 558, 1839.

[41] V. M. Goldschmidt, “Die Gesetze der Krystallochemie,” *Naturwissenschaften,* vol. 14, no. 21, pp. 477–485, May 1926.

[42] R. E. Eitel, C. A. Randall, T. R. Shrout, P. W. Rehrig, W. Hackenberger, and S.-E. Park, “New High Temperature Morphotropic Phase Boundary Piezoelectrics Based on Bi(Me)O_3 – PbTiO_3 Ceramics,” *Jpn. J. Appl. Phys.*, vol. 40, no. 10, pp. 5999–6002, 2001.

[43] H. D. Megaw, “Crystal Structure of Barium Titanate,” *Nature*, vol. 155, p. 484, 1945.

[44] J. Daintith, *A Dictionary of Physics*, 6th ed. Oxford University Press, 2009.

[45] D. Bérardan, S. Franger, D. Dragoe, A. K. Meena, and N. Dragoe, “Colossal dielectric constant in high entropy oxides,” *Phys. status solidi - Rapid Res. Lett.*, vol. 10, no. 4, pp. 328–333, Apr. 2016.

[46] J. W. Yeh, Y. L. Chen, S. J. Lin, and S. K. Chen, “High-Entropy Alloys – A New Era of Exploitation,” *Mater. Sci. Forum*, vol. 560, pp. 1–9, 2007.

[47] M.-H. Tsai and J.-W. Yeh, “High-Entropy Alloys: A Critical Review,” *Mater. Res. Lett.*, vol. 2, no. 3, pp. 107–123, Jul. 2014.

[48] C. M. Rost *et al.*, “Entropy-stabilized oxides,” *Nat. Commun.*, vol. 6, no. 1, p. 8485, Dec. 2015.

[49] H. A. Jahn and E. Teller, “Stability of polyatomic molecules in degenerate electronic states - I—Orbital degeneracy,” *Proc. R. Soc. London. Ser. A - Math. Phys. Sci.*, vol. 161, no. 905, pp. 220–235, Jul. 1937.

[50] P. S. H. and and K. R. Poeppelmeier*, “Noncentrosymmetric Oxides,” 1998.

[51] K. Sakayori *et al.*, “Curie Temperature of BaTiO_3,” *Jpn. J. Appl. Phys.*, vol. 34, pp. 5443–5445, 1995.

[52] B. Jaffe, W. R. Cook, and H. L. Jaffe, *Piezoelectric ceramics*. Academic Press,

1971.

[53] M. Ahart *et al.*, “Origin of morphotropic phase boundaries in ferroelectrics,” *Nature*, vol. 451, no. 7178, pp. 545–548, Jan. 2008.

[54] Y. Huan, X. Wang, J. Fang, and L. Li, “Grain Size Effects on Piezoelectric Properties and Domain Structure of $BaTiO_3$ Ceramics Prepared by Two-Step Sintering,” *J. Am. Ceram. Soc.*, vol. 96, no. 11, pp. 3369–3371, Nov. 2013.

[55] M. H. Frey, Z. Xu, P. Han, and D. A. Payne, “The Role of Interfaces on an Apparent Grain Size Effect on the Dielectric Properties for Ferroelectric Barium Titanate Ceramics,” *Ferroelectrics*, vol. 206–207, pp. 337–353, 1998.

[56] M. A. Reed, “Quantum Dots,” *Sci. Am.*, vol. 268, no. 1, pp. 118–123, 1993.

[57] S. L. Sass, *The Substance of Civilization*. New York: Arcade Publishing, 1998.

[58] G. Shirane, S. Hoshino, and K. Suzuki, “X-Ray Study of the Phase Transition in Lead Titanate,” *Phys. Rev.*, vol. 80, no. 6, pp. 1105–1106, Dec. 1950.

[59] D. Kajewski, P. Zajdel, A. Soszyński, J. Koperski, I. Lazar, and K. Roleder, “Bismuth doped $Pb(Zr_{0.70}Ti_{0.30})O_3$ ceramics and their properties driven by high temperature local polarity,” *Ceram. Int.*, vol. 45, no. 8, pp. 9871–9877, Jun. 2019.

[60] B. Noheda, “Structure and high-piezoelectricity in lead oxide solid solutions,” *Curr. Opin. Solid State Mater. Sci.*, vol. 6, no. 1, pp. 27–34, Feb. 2002.

[61] J.-R. Gomah-Pettry, S. Said, P. Marchet, and J.-P. Mercurio, “Sodium-bismuth titanate based lead-free ferroelectric materials,” *J. Eur. Ceram. Soc.*, vol. 24, no. 6, pp. 1165–1169, Jan. 2004.

[62] L. Egerton and D. M. Dillon, “Piezoelectric and Dielectric Properties of Ceramics in the System Potassium-Sodium Niobate,” *J. Am. Ceram. Soc.*, vol. 42, no. 9, pp.

438–442, Sep. 1959.

[63] X. Wang *et al.*, “Giant Piezoelectricity in Potassium–Sodium Niobate Lead-Free Ceramics,” *J. Am. Chem. Soc.*, vol. 136, no. 7, pp. 2905–2910, Feb. 2014.

[64] Y. Bai *et al.*, “(Ba,Ca)(Zr,Ti)O3 lead-free piezoelectric ceramics—The critical role of processing on properties,” *J. Eur. Ceram. Soc.*, vol. 35, no. 13, pp. 3445–3456, Nov. 2015.

[65] J. Rödel, K. G. Webber, R. Dittmer, W. Jo, M. Kimura, and D. Damjanovic, “Transferring lead-free piezoelectric ceramics into application,” *J. Eur. Ceram. Soc.*, vol. 35, no. 6, pp. 1659–1681, Jun. 2015.

[66] M. McQuarrie and F. W. Behnke, “Structural and Dielectric Studies in the System (Ba, Ca) (Ti, Zr)O_3,” *J. Am. Ceram. Soc.*, vol. 37, no. 11, pp. 539–543, Nov. 1954.

[67] N. Chaiyo, D. P. Cann, and N. Vittayakorn, “Phase transitions, ferroelectric, and piezoelectric properties of lead-free piezoelectric x$BaZrO_3$–(0.25−x)$CaTiO_3$–0.75$BaTiO_3$ ceramics,” *J. Mater. Sci.*, vol. 50, no. 18, pp. 6171–6179, Sep. 2015.

[68] W. Liu and X. Ren, “Large Piezoelectric Effect in Pb-Free Ceramics,” *Phys. Rev. Lett.*, vol. 103, no. 25, p. 257602, Dec. 2009.

[69] X. G. Tang, K.-H. Chew, J. Wang, and H. L. W. Chan, “Dielectric tunability of (Ba0.90Ca0.10)(Ti0.75Zr0.25)O3 ceramics,” *Appl. Phys. Lett.*, vol. 85, no. 6, pp. 991–993, Aug. 2004.

[70] N. Chaiyo, D. P. Cann, and N. Vittayakorn, “Lead-free (Ba,Ca)(Ti,Zr)O_3 ceramics within the polymorphic phase region exhibiting large, fatigue-free piezoelectric strains,” *Mater. Des.*, vol. 133, pp. 109–121, Nov. 2017.

[71] M. Acosta *et al.*, “$BaTiO_3$ -based piezoelectrics: Fundamentals, current status, and

perspectives," *Appl. Phys. Rev.*, vol. 4, no. 4, p. 041305, Dec. 2017.

[72] Z. Yao *et al.*, "Titanium deficiency in tetragonal-structured (Ba,Ca)(Zr,Ti)O_3 piezoelectric ceramics," *J. Alloys Compd.*, vol. 712, pp. 406–411, Jul. 2017.

[73] W. Cai *et al.*, "Effects of oxygen parial pressure on the electrical properties and phase transitions in (Ba,Ca)(Ti,Zr)O_3 ceramics," *J. Mater. Sci.*, vol. 55, pp. 9972–9992, 2020.

[74] D. Ghosh *et al.*, "Ferroelectric Materials: Domain Wall Displacement is the Origin of Superior Permittivity and Piezoelectricity in $BaTiO_3$ at Intermediate Grain Sizes (Adv. Funct. Mater. 7/2014)," *Adv. Funct. Mater.*, vol. 24, no. 7, pp. 884–884, Feb. 2014.

[75] A. Chen, Y. Zhi, J. Zhi, P. M. Vilarinho, and J. L. Baptista, "Synthesis and characterization of $Ba(Ti_{1-x}Ce_x)O_3$ ceramics," *J. Eur. Ceram. Soc.*, vol. 17, no. 10, pp. 1217–1221, Jan. 1997.

[76] G. Canu *et al.*, "Structure-property correlations and origin of relaxor behaviour in $BaCe_xTi_{1-x}O_3$," *Acta Mater.*, vol. 152, pp. 258–268, Jun. 2018.

[77] J. H. Hwang and Y. H. Han, "Dielectric Properties of $(Ba_{1-x}Ce_x)TiO_3$," *Jpn. J. Appl. Phys.*, vol. 39, no. Part 1, No. 5A, pp. 2701–2704, May 2000.

[78] G. Confalonieri, V. Buscaglia, G. Canu, M. T. Buscaglia, M. Dapiaggi, and IUCr, "The local and average structure of Ba(Ti,Ce)O_3 perovskite solid solution: effect of cerium concentration and particle size," *J. Synchrotron Radiat.*, vol. 26, no. 4, pp. 1280–1287, Jul. 2019.

[79] X. Wang, J. Yue, and J. Liu, "Enhanced temperature stability and electrical properties of Bi/Mn co-doped (Ba,Ca) (Zr,Ti)O_3 lead-free ceramics," *Ceram. Int.*,

vol. 47, no. 2, pp. 2525–2530, Jan. 2021.

[80] X. Liu *et al.*, “Enhancing piezoelectric properties of BCZT ceramics by Sr and Sn co-doping,” *J. Alloys Compd.*, vol. 640, pp. 128–133, Aug. 2015.

[81] G. M. Osoro, D. Bregiroux, M. P. Thi, and F. Levassort, “Structural and piezoelectric properties evolution induced by cobalt doping and cobalt/niobium co-doping in $BaTiO_3$,” *Mater. Lett.*, vol. 166, pp. 259–262, Mar. 2016.

[82] W. Hu *et al.*, “Electron-pinned defect-dipoles for high-performance colossal permittivity materials,” *Nat. Mater.*, vol. 12, no. 9, pp. 821–826, Sep. 2013.

[83] M. A. Subramanian, D. Li, N. Duan, B. A. Reisner, and A. W. Sleight, “High Dielectric Constant in $ACu_3Ti_4O_{12}$ and $ACu_3Ti_3FeO_{12}$ Phases,” *J. Solid State Chem.*, vol. 151, no. 2, pp. 323–325, May 2000.

[84] I. P. Raevski, S. A. Prosandeev, A. S. Bogatin, M. A. Malitskaya, and L. Jastrabik, “High dielectric permittivity in $AFe_{1/2}B_{1/2}O_3$ nonferroelectric perovskite ceramics (A=Ba, Sr, Ca; B=Nb, Ta, Sb),” *J. Appl. Phys.*, vol. 93, no. 7, pp. 4130–4136, Apr. 2003.

[85] Z. Wang, X. M. Chen, L. Ni, and X. Q. Liu, “Dielectric abnormities of complex perovskite $Ba(Fe_{1/2}Nb_{1/2})O_3$ ceramics over broad temperature and frequency range,” *Appl. Phys. Lett.*, vol. 90, no. 2, p. 022904, Jan. 2007.

[86] S. Saha and T. P. Sinha, “Low-temperature scaling behavior of $BaFe_{0.5}Nb_{0.5}O_3$,” *Phys. Rev. B*, vol. 65, no. 13, p. 134103, Mar. 2002.

[87] C.-Y. Chung, Y.-H. Chang, and G.-J. Chen, “Effects of lanthanum doping on the dielectric properties of $Ba(Fe_{0.5}Nb_{0.5})O_3$ ceramic,” *J. Appl. Phys.*, vol. 96, no. 11, pp. 6624–6628, Dec. 2004.

[88] X. Sun *et al.*, "Grain boundary defect compensation in Ti-doped $BaFe_{0.5}Nb_{0.5}O_3$ ceramics," *Appl. Phys. A*, vol. 122, no. 9, p. 864, Sep. 2016.

[89] U. Intatha, S. Eitssayeam, and T. Tunkasiri, "Giant Dielectric Behavior of $BaFe_{0.5}Nb_{0.5}O_3$ Perovskite Ceramic," in *Condensed Matter Theories*, 2008, pp. 429–435.

[90] D. Bochenek, P. Niemiec, M. Adamczyk, and I. Szafraniak-Wiza, "Physical properties of lead-free $BaFe_{1/2}Nb_{1/2}O_3$ ceramics obtained from mechanochemically synthesized powders," *J. Mater. Sci.*, vol. 53, no. 19, pp. 13501–13512, Oct. 2018.

[91] D. Bochenek, P. Niemiec, I. Szafraniak-Wiza, M. Adamczyk, and R. Skulski, "Preparation and dielectric properties of the lead-free $BaFe_{1/2}Nb_{1/2}O_3$ ceramics obtained from mechanically triggered powder," *Eur. Phys. J. B*, vol. 88, no. 10, p. 277, Oct. 2015.

[92] R. Zhang and P. Taskinen, "A phase equilibria study and thermodynamic assessment of the BaO–Al2O3 system," *Calphad*, vol. 51, pp. 42–50, Dec. 2015.

[93] W. C. Röntgen, "On a new kind of rays," *Science (80-.).*, vol. 3, no. 59, pp. 227–231, 1896.

[94] T. Young, "II. The Bakerian Lecture. On the theory of light and colours," *Philos. Trans. R. Soc. London*, vol. 92, pp. 12–48, Dec. 1802.

[95] W. H. Bragg and W. L. Bragg, "The Reflection of X-rays by Crystals," *Proc. R. Soc. London. Ser. A, Contain. Pap. a Math. Phys. Character*, vol. 88, no. 605, pp. 428–438, Jul. 1913.

[96] H. M. Rietveld, "The Rietveld method," *Phys. Scr.*, vol. 89, no. 9, p. 098002, Sep. 2014.

[97] A. A. Coelho, “Whole-profile structure solution from powder diffraction data using simulated annealing,” *J. Appl. Crystallogr.*, vol. 33, no. 3, pp. 899–908, Jun. 2000.

[98] D. C. Joy, “The theory and practice of high-resolution scanning electron microscopy,” *Ultramicroscopy*, vol. 37, no. 1–4, pp. 216–233, Aug. 1991.

[99] “ProboStat^{TM} Manual.”

[100] “A-Tech Systems.” [Online]. Available: https://www.atech-systems.com/probostat.html.

[101] “ProboStat Versatile High Temperature Test Fixture - Maranata-Madrid SL - NIF B-85746204.” [Online]. Available: https://www.alphaomega-electronics.com/en/norecs/2256-probostat-accesorio-de-prueba-versatil-de-alta-temperatura.html.

[102] N. Izyumskaya, Y.-I. Alivov, S.-J. Cho, H. Morkoç, H. Lee, and Y.-S. Kang, “Processing, Structure, Properties, and Applications of PZT Thin Films,” *Crit. Rev. Solid State Mater. Sci.*, vol. 32, no. 3–4, pp. 111–202, Dec. 2007.

[103] D. Damjanovic, “A morphotropic phase boundary system based on polarization rotation and polarization extension,” *Appl. Phys. Lett.*, vol. 97, no. 6, p. 062906, Aug. 2010.

[104] W. Jo *et al.*, “Evolving morphotropic phase boundary in lead-free (Bi1/2Na1/2)TiO3–BaTiO3 piezoceramics,” *J. Appl. Phys.*, vol. 109, no. 1, p. 014110, Jan. 2011.

[105] D. Damjanovic, “Ferroelectric, dielectric and piezoelectric properties of ferroelectric thin films and ceramics,” *Reports Prog. Phys.*, vol. 61, no. 9, pp.

1267–1324, 1998.

[106] M. Marsilius, K. G. Webber, E. Aulbach, and T. Granzow, "Comparison of the Temperature-Dependent Ferroelastic Behavior of Hard and Soft Lead Zirconate Titanate Ceramics," *J. Am. Ceram. Soc.*, vol. 93, no. 9, pp. 2850–2856, Jun. 2010.

[107] R. E. Eitel, C. A. Randall, T. R. Shrout, P. W. Rehrig, W. Hackenberger, and S.-E. Park, "New High Temperature Morphotropic Phase Boundary Piezoelectrics Based on Bi (Me) O 3 – PbTiO 3 Ceramics," *Jpn. J. Appl. Phys.*, vol. 40, no. 10, pp. 5999–6002, 2001.

[108] R. Duan, R. F. Speyer, E. Alberta, and T. R. Shrout, "High Curie temperature perovskite BiInO3–PbTiO3 ceramics," *J. Mater. Res.*, vol. 19, no. 07, pp. 2185–2193, Jul. 2004.

[109] S. Zhang, R. Xia, C. A. Randall, T. R. Shrout, R. Duan, and R. F. Speyer, "Dielectric and Piezoelectric Properties of Niobium-modified BiInO3–PbTiO3 Perovskite Ceramics with High Curie Temperatures," *J. Mater. Res.*, vol. 20, no. 08, pp. 2067–2071, Aug. 2005.

[110] J. Fu and R. Zuo, "Giant electrostrains accompanying the evolution of a relaxor behavior in Bi(Mg,Ti)O 3-PbZrO 3-PbTiO 3 ferroelectric ceramics," 2013.

[111] W. Hu, X. Tan, and K. Rajan, "BiFeO3–PbZrO3–PbTiO3 ternary system for high Curie temperature piezoceramics," *J. Eur. Ceram. Soc.*, vol. 31, no. 5, pp. 801–807, May 2011.

[112] A. Molak *et al.*, "Electric features of PZT 70/30–BiMnO3 solid solution ceramics," *J. Eur. Ceram. Soc.*, vol. 35, no. 9, pp. 2513–2522, Sep. 2015.

[113] S. C. Lee *et al.*, "Bi(Zn 0.5 Ti 0.5)O 3 substitution effects in Pb(Zr,Ti)O 3

piezoelectric ceramics around morphotropic phase boundary region," *Ferroelectrics*, vol. 401, no. 1, pp. 181–185, Oct. 2010.

[114] A. a Belik, S. Y. Stefanovich, and B. I. Lazoryak, "BiInO 3 : A Polar Oxide with GdFeO 3 -Type Perovskite Structure," *Chem. Mater*, vol. 18, no. 8, pp. 1964–1968, 2006.

[115] B. Noheda, J. Gonzalo, L. Cross, R. Guo, and S.-E. Park, "Tetragonal-to-monoclinic phase transition in a ferroelectric perovskite: The structure," *Phys. Rev. B - Condens. Matter Mater. Phys.*, vol. 61, no. 13, pp. 8687–8695, Apr. 2000.

[116] M. Morozov, "Softening and Hardening Transitions in Ferroelectric Pb(Zr,Ti)O 3 Ceramics," 2005.

[117] L. E. Cross, "Relaxor ferroelectrics," *Ferroelectrics*, vol. 76, no. 1, pp. 241–267, Dec. 1987.

[118] A. Sehirlioglu, A. Sayir, and F. Dynys, "High temperature properties of BiScO3–PbTiO3 piezoelectric ceramics," *J. Appl. Phys.*, vol. 106, no. 1, p. 014102, Jul. 2009.

[119] M. McQUARRIE and F. W. BEHNKE, "Structural and Dielectric Studies in the System (Ba, Ca) (Ti, Zr)O3," *J. Am. Ceram. Soc.*, vol. 37, no. 11, pp. 539–543, Nov. 1954.

[120] P. Hansen, D. Hennings, and H. Schreinemacher, "Dielectric Properties of Acceptor-Doped (Ba,Ca)(Ti,Zr)O 3 Ceramics," *J. Electroceramics*, vol. 2, no. 2, pp. 85–94, 1998.

[121] D. Xue, Y. Zhou, H. Bao, J. Gao, C. Zhou, and X. Ren, "Large piezoelectric effect in Pb-free Ba(Ti,Sn)O$_3$ -x(Ba,Ca)TiO$_3$ ceramics," *Appl. Phys. Lett.*, vol. 99, no.

12, p. 122901, Sep. 2011.

[122] J. Wu, A. Habibul, X. Cheng, X. Wang, and B. Zhang, “Orthorhombic–tetragonal phase coexistence and piezoelectric behavior in (1−x)(Ba,Ca)(Ti,Sn)O3–x(Ba,Ca)(Ti,Zr)O3 lead-free ceramics,” *Mater. Res. Bull.*, vol. 48, no. 10, pp. 4411–4414, Oct. 2013.

[123] S.-W. Zhang, H. Zhang, B.-P. Zhang, and G. Zhao, “Dielectric and piezoelectric properties of (Ba0.95Ca0.05)(Ti0.88Zr0.12)O3 ceramics sintered in a protective atmosphere,” *J. Eur. Ceram. Soc.*, vol. 29, no. 15, pp. 3235–3242, Dec. 2009.

[124] R. Hayati, M. A. Bahrevar, Y. Ganjkhanlou, V. Rojas, and J. Koruza, “Electromechanical properties of Ce-doped (Ba0.85Ca0.15)(Zr0.1Ti0.9)O3 lead-free piezoceramics,” *J. Adv. Ceram.*, vol. 8, no. 2, pp. 186–195, Jun. 2019.

[125] P. Hansen, D. Hennings, and H. Schreinemacher, “High-K Dielectric Ceramics from Donor/Acceptor-Codoped (Ba1−xCax)(Ti1-yZry)O3 (BCTZ),” *J. Am. Ceram. Soc.*, vol. 81, no. 5, pp. 1369–1373, Jan. 2005.

[126] M. Acosta *et al.*, “BaTiO$_3$ -based piezoelectrics: Fundamentals, current status, and perspectives,” *Appl. Phys. Rev.*, vol. 4, no. 4, p. 041305, Dec. 2017.

[127] Y. Tian, X. Chao, L. Jin, L. Wei, P. Liang, and Z. Yang, “Polymorphic structure evolution and large piezoelectric response of lead-free (Ba,Ca)(Zr,Ti)O$_3$ ceramics,” *Appl. Phys. Lett.*, vol. 104, no. 11, p. 112901, Mar. 2014.

[128] R. D. Shannon, C. T. Prewitt, and IUCr, “Revised values of effective ionic radii,” *Acta Crystallogr. Sect. B Struct. Crystallogr. Cryst. Chem.*, vol. 26, no. 7, pp. 1046–1048, Jul. 1970.

[129] Grimes Robin, “Database of Ionic Radii (Shannon Radii).” [Online]. Available:

http://abulafia.mt.ic.ac.uk/shannon/ptable.php.

[130] “Bismuth Oxide | AMERICAN ELEMENTS ®.” [Online]. Available: https://www.americanelements.com/bismuth-oxide-1304-76-3.

[131] W. S. H. M. W. Ahmad *et al.*, “5G Technology: Towards Dynamic Spectrum Sharing Using Cognitive Radio Networks,” *IEEE Access*, vol. 8, pp. 14460–14488, 2020.

[132] Y. Honda, “No Title,” *AEI*, p. 48, Oct-2004.

[133] G. H. Haertling, “Ferroelectric ceramics: History and technology,” *J. Am. Ceram. Soc.*, vol. 82, no. 4, pp. 797–818, Apr. 1999.

[134] L. E. Cross, “Relaxorferroelectrics: An overview,” *Ferroelectrics*, vol. 151, no. 1, pp. 305–320, Jan. 1994.

[135] M. A. Zurbuchen *et al.*, “Bismuth volatility effects on the perfection of SrBi2Nb2O9 and SrBi2Ta2O9 films,” *Appl. Phys. Lett.*, vol. 82, no. 26, pp. 4711–4713, Jun. 2003.

APPENDICES

Appendix A – Supplemental Information for Chapter 3

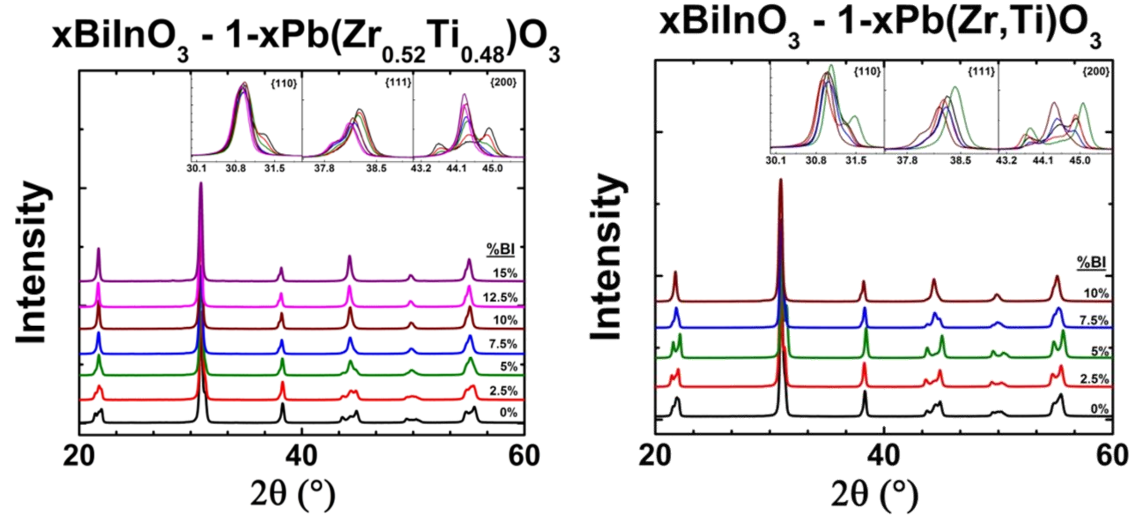

Figure A1: XRD plots of single phase, calcined (x) $BiInO_3$ – (1-x) $Pb(Zr_yTi_{1-y})O_3$ for (left) y = 0.52 and (right) y = 0.50 for increasing composition of $BiInO_3$. Samples were calcined as loose powders between 900°C – 1000°C for 2h with a 5°C/min ramp. Samples were calcined various times to achieve single phase. Inserts are included to help identify room temperature phase transitions.

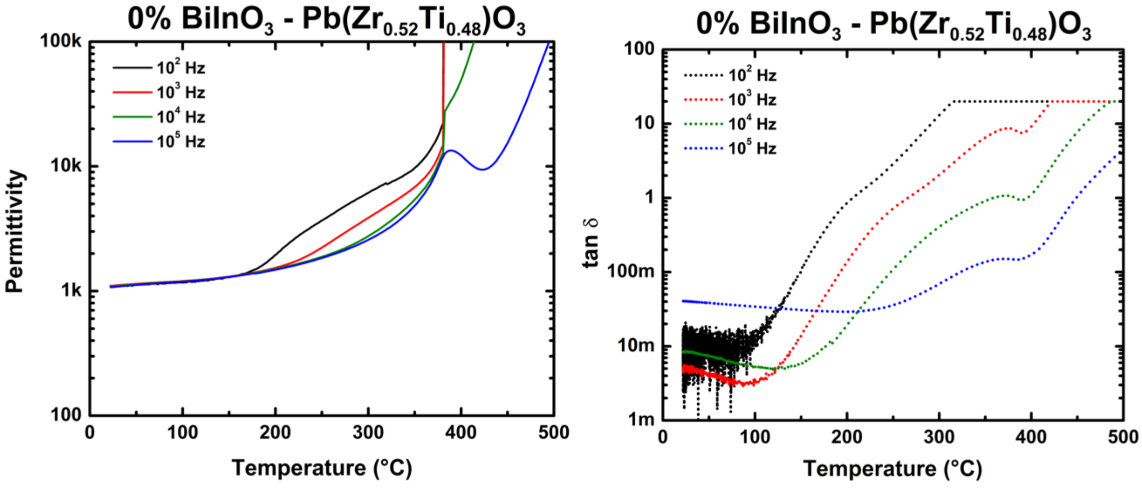

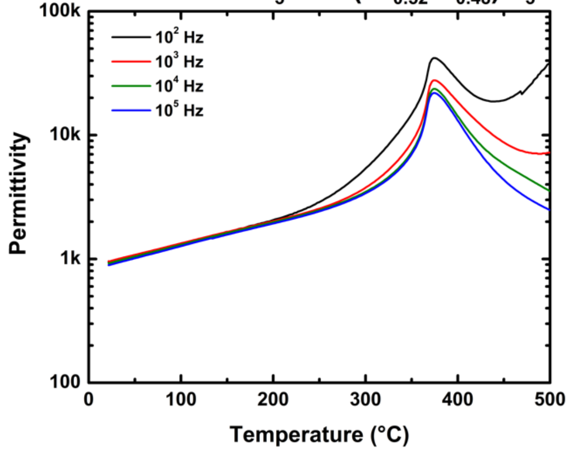

2.5% $BiInO_3$ - $Pb(Zr_{0.52}Ti_{0.48})O_3$

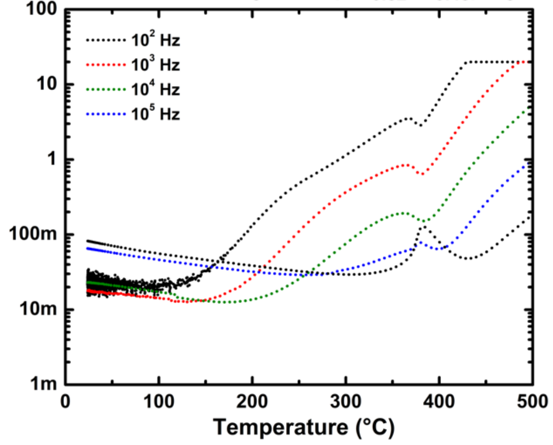

2.5% $BiInO_3$ - $Pb(Zr_{0.52}Ti_{0.48})O_3$

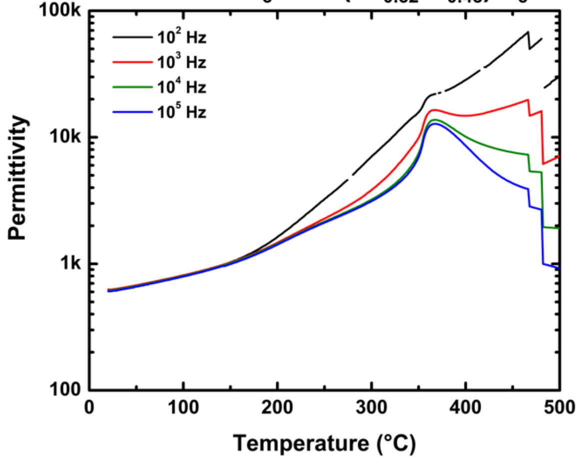

5% $BiInO_3$ - $Pb(Zr_{0.52}Ti_{0.48})O_3$

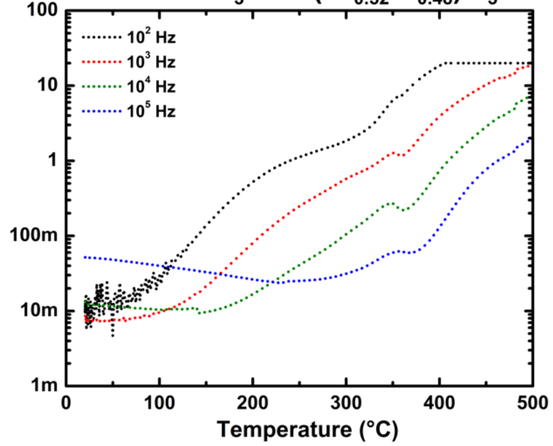

5% $BiInO_3$ - $Pb(Zr_{0.52}Ti_{0.48})O_3$

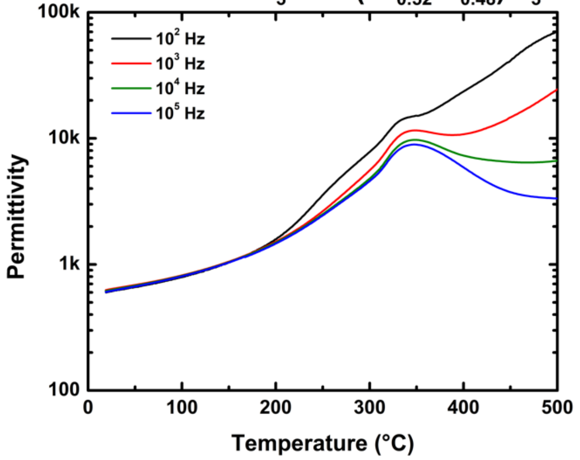

7.5% $BiInO_3$ - $Pb(Zr_{0.52}Ti_{0.48})O_3$

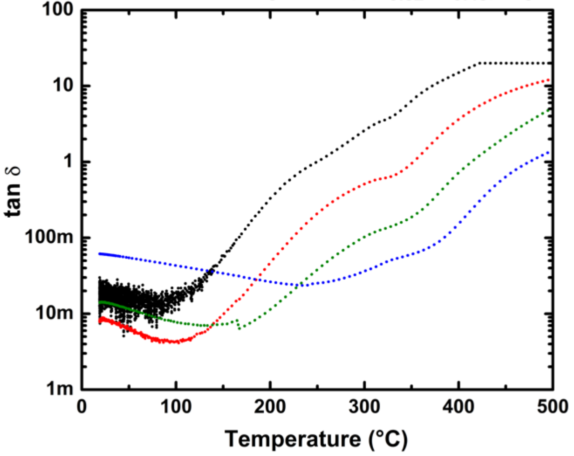

7.5% $BiInO_3$ - $Pb(Zr_{0.52}Ti_{0.48})O_3$

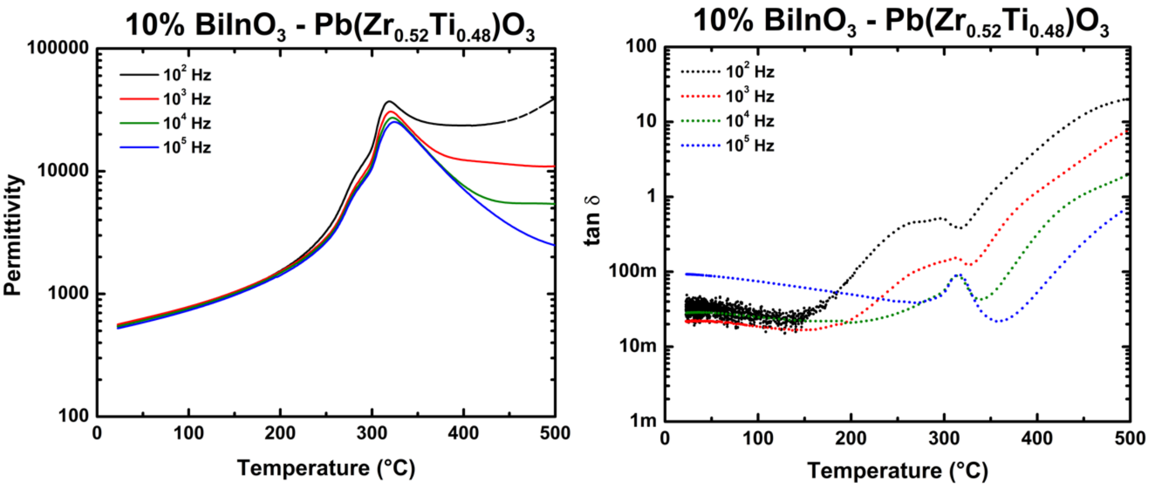

Figure A2: Permittivity (left) and dissipation factor (right) as a function of temperature at selected frequencies for increasing composition of BiInO$_3$ in x BiInO$_3$ – (1-x) Pb(Zr$_{0.52}$Ti$_{0.48}$)O$_3$. Discontinuities in 5% BI permittivity are due to physical breakdown of sample during testing.

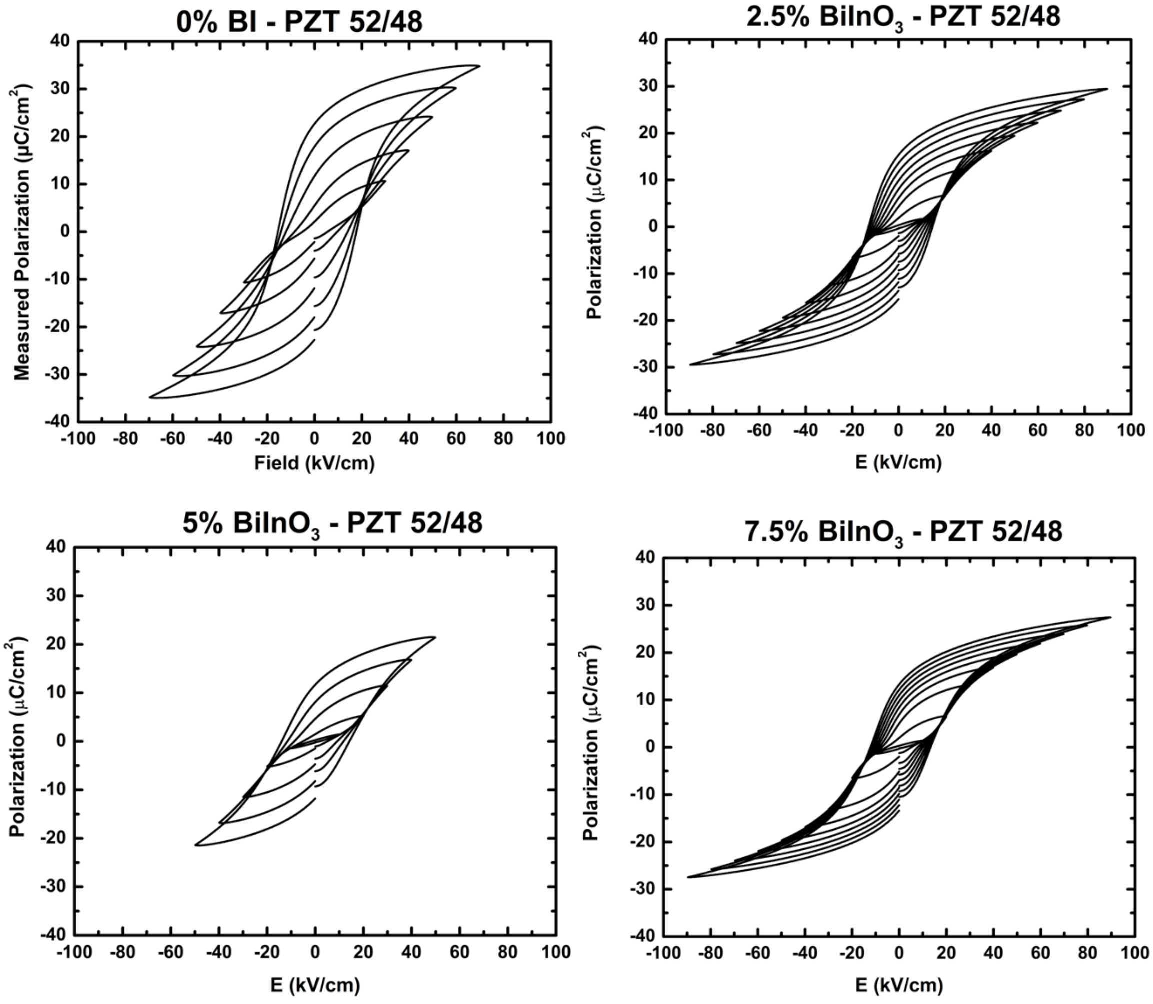

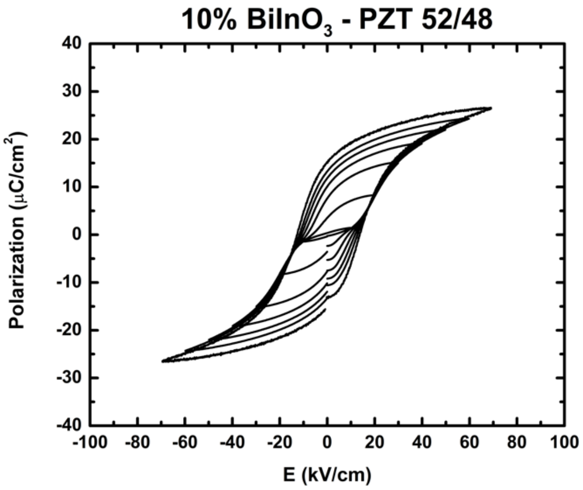

Figure A3: Polarization versus electric field for unpoled BiInO$_3$ containing samples executed at 1Hz. Fields were increased at 10kV/cm intervals from 10kV/cm until breakdown, accounting for discrepancies in max fields between samples. Each loop represents a three-loop scanning average. Full saturation was observed between 40 kV/cm and 50 kV/cm for all samples, which exhibit a prototypical ferroelectric response from saturation until breakdown, ranging from 60 kV/cm to 100kV/cm. At 50 kV/cm all samples exhibit a maximum polarization of 20 ± 2 μC/cm^2, a remnant polarization of 10 ± 2 μC/cm^2, and a coercive field of 11.5 ± 3 kV/cm.

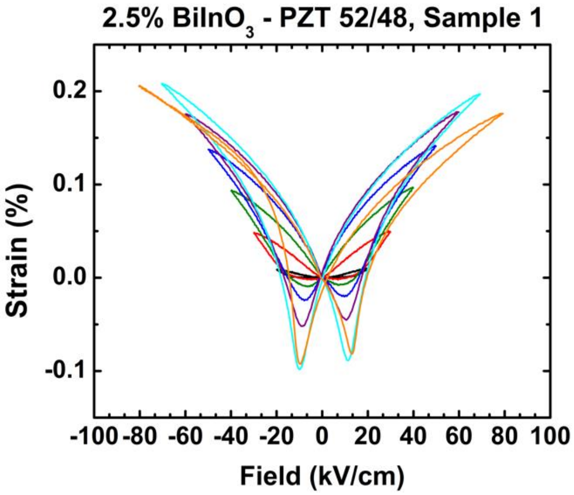

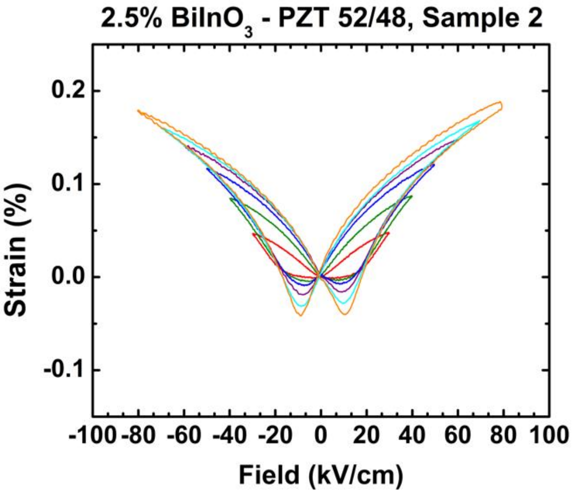

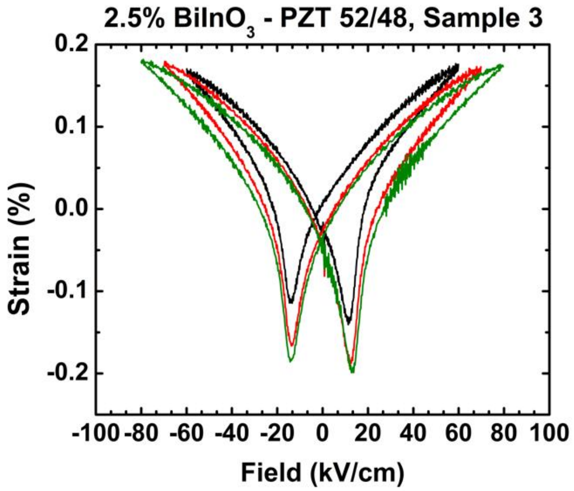

Figure A4: Strain data for only the 2.5% BI – PZT 52/48 composition due to time constraints. Non-zero, zero-field strain on sample 3 can be attributed to experimental error, as initial data was un-useable. The observed secondary scans undoubtedly contain strain contributions due to an induced poled state from initial measurements, as no thermal anneal was done post measurement. Scans show the appearance of negative strain around 50kV/cm, suggesting the onset of full saturation, in agreement with the observed trend in the polarization data. Strain maximums at 70kV/cm range from 0.175% (sample 2), to 0.215% (sample 1). This is proportional to a d_{33}^* of 248 pC/N.

Appendix B – Supplemental Information for Chapter 5

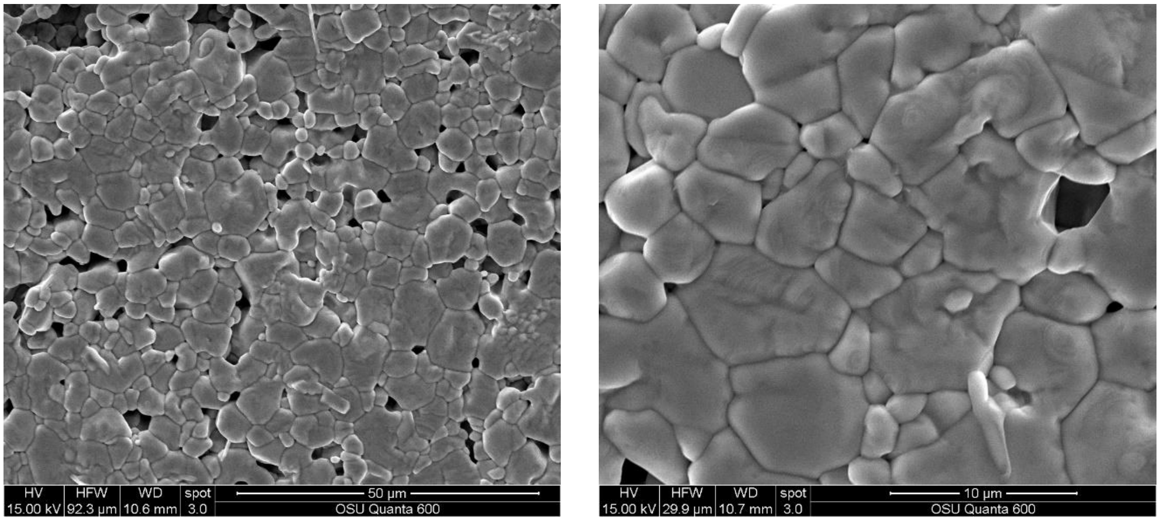

Figure B1: Micrographs at varying magnification of 1% $Bi(Zn_{1/2}Ti_{1/2})O_3$ – 99% $Ba_{0.85}Ca_{0.15}(Zr_{0.10}Ti_{0.90})O_3$ sintered at 1400°C/4h dense ceramic thermally etched at 1300°C/1h as imaged on Oregon State University Electron Microscopy Facility with an FEI Quanta 600FEG environmental SEM

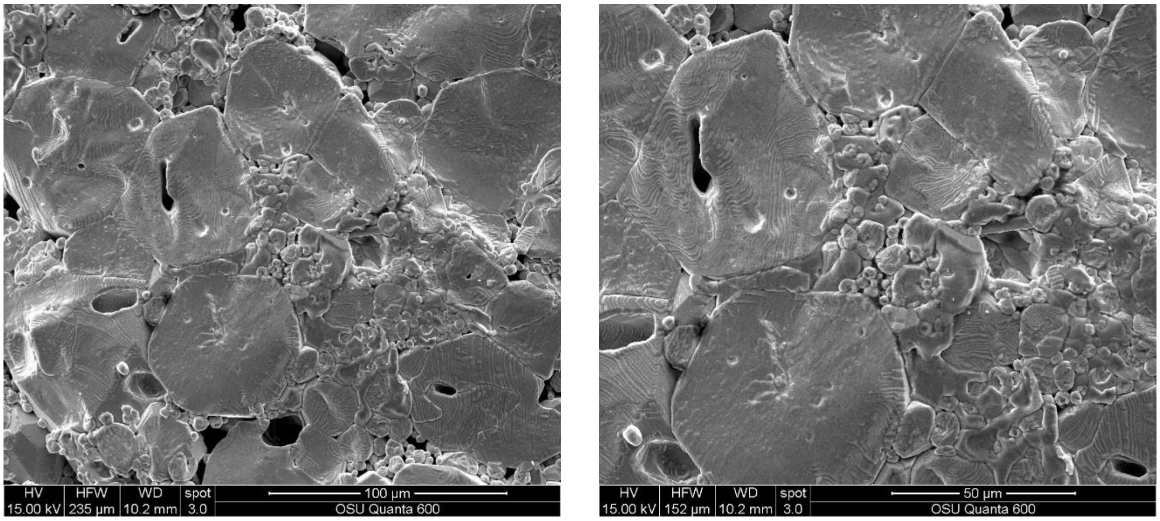

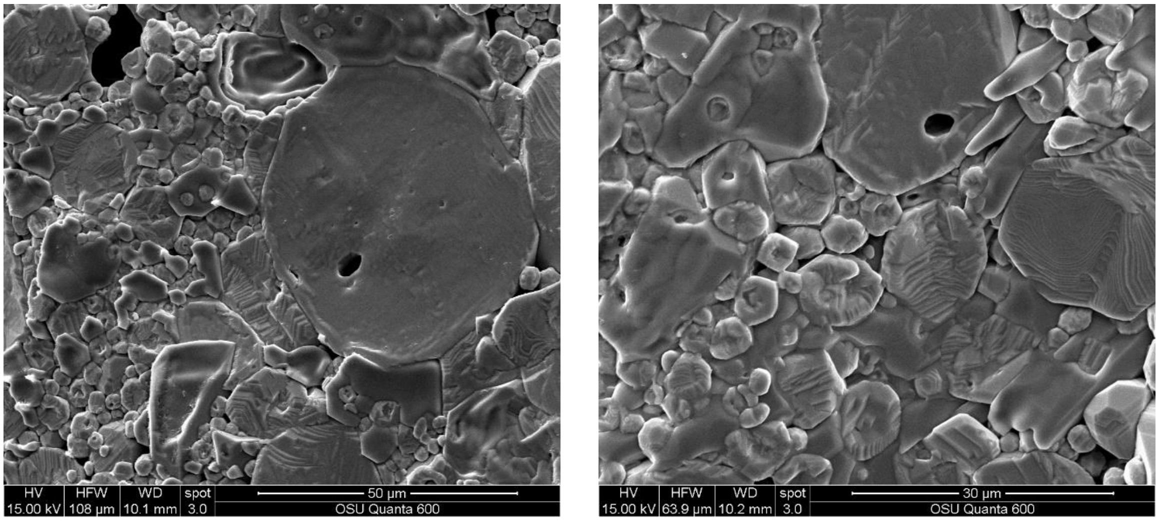

Figure B2: Micrographs at varying magnification of 1% $Bi(Zn_{1/2}Ti_{1/2})O_3$ – 99% $Ba_{0.85}Ca_{0.15}(Zr_{0.10}Ti_{0.90})O_3$ sintered at 1380°C/4h dense ceramic thermally etched at 1300°C/1h as imaged on Oregon State University Electron Microscopy Facility with an FEI Quanta 600FEG environmental SEM

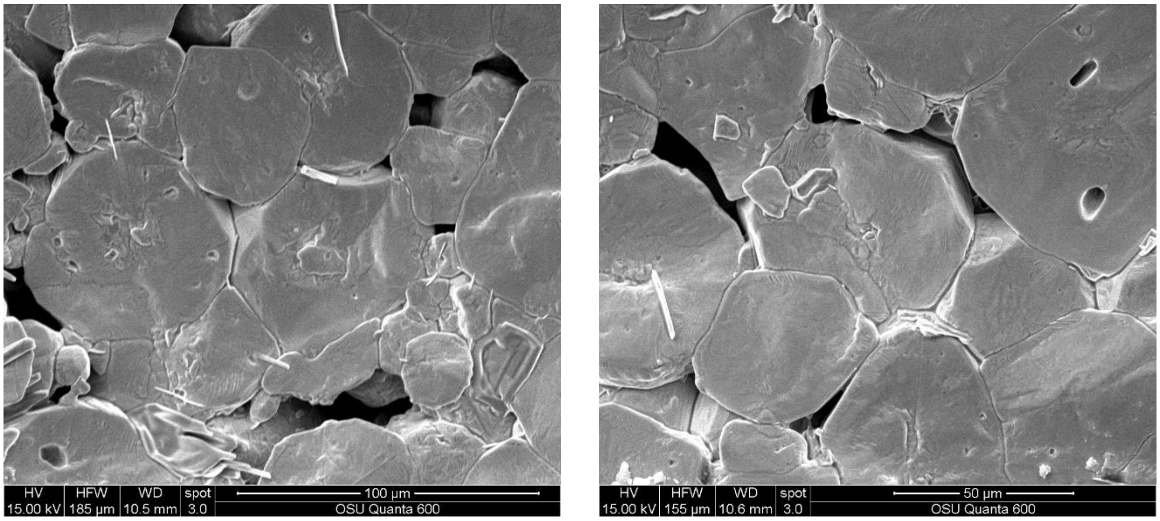

Figure B3: Micrographs at varying magnification of 1% $Bi(Zn_{1/2}Ti_{1/2})O_3$ – 99% $Ba_{0.85}Ca_{0.15}(Zr_{0.10}Ti_{0.90})O_3$ sintered at 1400°C/4h with 10°C/min cooling rate and 3 mol% Bi excess dense ceramic thermally etched at 1300°C/1h as imaged on Oregon State University Electron Microscopy Facility with an FEI Quanta 600FEG environmental SEM